

Monte-Carlo Background Studies for Space-Based Detectors in X-ray Astronomy

Dissertation
zur Erlangung des Grades eines Doktors
der Naturwissenschaften
der Fakultät für Mathematik und Physik
der Eberhard-Karls-Universität zu Tübingen

vorgelegt von

Jan-Christoph Tenzer

aus Tübingen
2008

Selbstverlegt von: J.C. Tenzer, Mohlstr. 23, 72074 Tübingen
Tag der mündlichen Prüfung: 24. Juli 2008
Dekan: Prof. Dr. N. Schopohl
1. Berichterstatter: Prof. Dr. A. Santangelo
2. Berichterstatter: Prof. Dr. K. Werner

Abstract

The observation of most astrophysical X-ray sources is characterized by the fact that these usually rather weak cosmic sources have to be detected in the presence of a very strong background. This background, which has its origin in the interactions of high-energy cosmic particles with the materials that constitute the camera and also in the characteristic properties of the respective detector, has a strong impact on the ultimately achievable sensitivity of the instrument. Sources that have a flux below the limiting minimum detectable flux of a certain instrument will therefore not be detected or cannot be observed within a given experiment. To gain a higher sensitivity, which always converts to new scientific results, an intense effort to minimize the internal detector background is undertaken.

This thesis has been devoted to simulation studies of the instrumental background of X-ray detectors in astronomy. In this context, it is first shown on the basis of the pn-CCD camera on board the XMM-Newton satellite, that Monte-Carlo simulations of the physics processes and interactions caused by the radiation environment in the respective orbit can reproduce the measurements of the actual detector background. With the thus validated simulation environment, the detector geometry of the future X-ray mission *Simbol-X* has been optimized in collaboration with the designers. Special attention has been paid to the task of background minimization and experiment deadtime. Furthermore, the composition and spectral shape of the remaining background is predicted. For another future X-ray telescope called *eROSITA*, estimations of the detector background, depending on different orbit inclinations and thus different radiation environments, are presented.

Part of the work has also been concerned with hardware development. In a collaboration with the electronics lab at the Institute for Astronomy and Astrophysics in Tübingen (IAAT), a fast digital detector-event preprocessor based on experiences gained with XMM-Newton has been developed. The processor, which has been designed for utilization on board, filters the detector output with different criteria and therefore noticeably reduces the detector background as well as the necessary telemetry rate.

Erweiterte deutsche Zusammenfassung

Die Beobachtung einer Vielzahl astrophysikalischer Quellen im Röntgenbereich ist dadurch charakterisiert, dass die Detektion der Quellphotonen in Gegenwart eines hohen Detektorhintergrundes stattfindet. Dieser Hintergrund entsteht durch die Wechselwirkung von hochenergetischen Teilchen mit den Detektormaterialien und die dadurch hervorgerufene Sekundärstrahlung. Neben den jeweiligen Charakteristika des verwendeten Detektortyps, hat er entscheidenden Einfluss auf die letztendlich erreichbare Empfindlichkeit des Instrumentes. Quellen, die Photonenflüsse unterhalb eines aus dieser wichtigen Größe ableitbaren, für das Experiment limitierenden, minimalen noch detektierbaren Flusses aufweisen, können nicht entdeckt bzw. beobachtet werden. Um die Sensitivität weiter zu steigern, werden bei der Konzeption zukünftiger Instrumente große Anstrengungen unternommen, den Detektorhintergrund möglichst gering zu halten.

In diesem Zusammenhang zeigt die vorliegende Arbeit anhand der pn-CCD Kamera an Bord des Satelliten XMM-Newton, dass Monte-Carlo Simulationen der physikalischen Wechselwirkungen zwischen der Strahlungsumgebung im entsprechenden Orbit und Materialien der Detektoren den tatsächlich gemessenen Detektorhintergrund reproduzieren können. Aufbauend auf diesen Ergebnissen konnte die Geometrie der Fokalebene, die momentan für den Röntgensatelliten Simbol-X entwickelt wird, in Zusammenarbeit mit den Ingenieuren hinsichtlich des Hintergrundes und der Totzeit des Detektors optimiert werden. Die Zusammensetzung und die spektrale Verteilung des noch verbleibenden Hintergrundes wurden errechnet. Anhand weiterer Simulationen wurde der zu erwartende Kamerahintergrund des geplanten Röntgenteleskopes eROSITA abgeschätzt.

In Zusammenarbeit mit der Elektronikabteilung am Tübinger Institut für Astronomie und Astrophysik (IAAT) wurde eine schnelle digitale Elektronik zur ersten Verarbeitung von Detektorereignissen an Bord entworfen, die auf den ebenfalls bei XMM-Newton erworbenen Erfahrungen aufbaut. Diese verringert den Detektorhintergrund sowie die notwendige Telemetrierate zur Datenübertragung nochmals deutlich.

Contents

1	Observational Astronomy in the X-ray Range	1
1.1	The Beginning of X-ray Astronomy	1
1.2	Observational Techniques in X-ray Astronomy	3
1.2.1	Non-Focusing Imaging Techniques	3
1.2.2	Focusing Techniques	4
1.2.3	Current Detector Types	6
1.3	An Overview of Modern X-ray Observatories	8
1.4	On the Importance of a Low Detector Background	10
2	The GEANT4 Toolkit	15
2.1	On Monte-Carlo Simulations	15
2.2	Introduction to GEANT4	16
2.2.1	Historic Evolution of GEANT4	17
2.2.2	Scientific Community	17
2.2.3	Pseudo-Random Number Generation in GEANT4	18
2.3	Structure and Design of GEANT4 Simulations	19
2.4	The Physics Behind GEANT4	21
2.4.1	Implementation of Physics Processes	22
2.4.2	Physics Validation	25
2.5	Comprehensiveness and Possibilities of GEANT4	25
2.5.1	Recent Developments	25
2.5.2	GEANT4 Applications in Space Science	26
3	Simulation of the XMM-Newton EPIC pn-Camera Detector Background	27
3.1	An Introduction to the XMM-Newton Observatory	27
3.1.1	The MOS Cameras	28
3.1.2	The EPIC pn-Camera	28
3.2	The Geometric Model of XMM-Newton Used in the Simulations	29
3.2.1	The XMM-Newton Spacecraft	29
3.2.2	Implementation of the EPIC pn-Camera	30
3.2.3	The CCDs and the Backplane PCB	30
3.3	The Measured Detector Background	31
3.3.1	Composition of the Background	31
3.3.2	Data Selection and Reduction	32

3.4	Details of the Simulations	34
3.4.1	The Simulation Environment	35
3.4.2	Incoming Particle Spectrum and Flux	35
3.4.3	Data Generation and Storage	36
3.5	Results of the Simulations and Comparison to Measured Data	37
3.5.1	Quantum Efficiency of the pn-CCDs	37
3.5.2	Simulated vs. Measured Background Spectra	38
3.5.3	Simulated vs. Measured Fluorescence Images	40
3.6	Discussion of the Results	40
4	The Simbol-X Mission	43
4.1	Mission Concept and Characteristics	44
4.1.1	Scientific Objectives	44
4.1.2	Optics	47
4.1.3	Low Energy Detector	48
4.1.4	High Energy Detector	50
4.1.5	Active Anticoincidence Detector	51
4.2	Summary	51
5	Simulations for Simbol-X	53
5.1	Challenges and Goals of the Simulation Activities	53
5.1.1	Composition of the Detector Background and Optimizations Measures	53
5.2	Parameters and Characteristics of the Simulation Environment	56
5.2.1	The Geometric Model	56
5.2.2	Incoming Particle Fluxes and Spectra	59
5.2.3	Considered Physics Processes	61
5.2.4	Event Data Evaluation	62
5.3	Details of the Performed Simulations and their Results	62
5.3.1	Particle Production Cuts, Accuracy and Computation Time	63
5.3.2	Simulation of the Quantum Efficiency of Both Detectors	64
5.3.3	Expected Simbol-X Detector Background	65
5.3.4	Simulated Remaining Background Spectra	67
5.3.5	Performance of the Graded Shield	67
5.3.6	Effects of Thickness Variation of the Tantalum Component in the Graded Shield	68
5.3.7	Reducing the LED Deadtime by Optimizing the Anticoincidence Detector	69
5.3.8	Further Results of the SPST Group	72
5.3.9	Improvements of the Mission Design as a Consequence of Simulations	73
5.3.10	Simulated Observation of the Diffuse Cosmic X-ray Background Spec- trum	74
5.3.11	Calculations Regarding the Sensitivity of Simbol-X	76
5.4	Discussion of the Results	77

6	Simulation and Measurement of X-ray Fluorescence Backlight from CdTe	79
6.1	The Experimental Setup	79
6.1.1	The DEPFET Active Pixel Sensor Matrix	81
6.1.2	The CdTe-Crystals	82
6.1.3	X-ray Sources	83
6.2	Simulation of the Experiment	83
6.2.1	The Geometric Model of the Experimental Setup	83
6.2.2	Simulation of the X-ray Sources	84
6.2.3	Data Generation and Storage	85
6.2.4	Simulation Results	85
6.3	Description of the Measurements	86
6.3.1	Data Selection and Processing	87
6.4	Comparison Between Simulated and Measured Data	87
6.5	Discussion	89
7	The Simbol-X Event-Preprocessor	91
7.1	LED Electronics Overview	91
7.2	Tasks of the Event-Preprocessor	92
7.3	On Board Event-Preprocessing	94
7.3.1	Pixel Correction Unit	94
7.3.2	Common Mode Correction Unit	94
7.3.3	Energy Threshold Analyzer Unit	96
7.3.4	Pattern and Trace Analyzing Unit	96
7.3.5	Programmable Pixel Filter Unit	97
7.3.6	Generation of Housekeeping Data	98
7.4	EPP Testbench Environment	98
7.5	Results of the EPP Tests	98
7.6	Discussion and Outlook	101
8	Simulations for eROSITA	103
8.1	Introduction	104
8.1.1	Scientific Goals of the eROSITA Mission	104
8.1.2	The Spectrum-RG Observatory	105
8.1.3	The eROSITA Instrument	105
8.1.4	The Frame Store pnCCD-Camera	106
8.2	Details and Results of the Simulations	108
8.2.1	Goals of the Simulations	108
8.2.2	Simulation Geometry	108
8.2.3	Incoming Particle Spectra and Fluxes	109
8.2.4	Simulation Results	110
8.3	Discussion of the Results	112

9	Summary and Conclusions	115
9.1	Summary	115
9.2	Outlook	116
A	Details of the Simulation Environment	119

Observational Astronomy in the X-ray Range

The domain of Astronomy today encompasses numerous areas of specialization that are characterized on the basis of their subject of research. In the field of *Observational Astronomy*, however, a classification based on the energy or wavelength of the observed photons has been established, with common methods and instruments applied within these major sections of the electromagnetic spectrum. As of today, we distinguish the areas of radio- and infrared-astronomy at energies below the field of classical optical astronomy and UV-, X-ray and γ -astronomy at higher energies, which extend up to 10^{12} eV. As the Earth's atmosphere is in some of these ranges mainly opaque to radiation, observations became only recently possible with the technological advancements of the space age and the ability to transport the detectors to higher altitudes, outside the bulk of the atmosphere, with balloons, rockets and satellites (see *Fig. 1.1*).

1.1 *The Beginning of X-ray Astronomy*

The fact that X-ray photons from celestial sources cannot be detected on ground due to the high level of atmospheric absorption has been most decisive for the development of experiments in X-ray astronomy (0.1 keV - 100 keV, or 10 nm - 10 pm). The first detection of X-ray emission from the solar corona in 1949 with a detector carried by a rocket (Friedman et al., 1951) was so weak, that it was assumed that no further sources would be detectable due to their large distance. In 1962 another rocket experiment by Giacconi et al. (1962, 1964) detected the first source outside the solar system, Sco X-1, which contrary to the Sun was found to be much more powerful in X-rays than in the optical. This discovery opened a new window to the universe and revolutionized our understanding of stellar evolution and physics as well as the processes responsible for the generation of radiation.

With the availability of satellites as a platform to carry the detectors, much longer observations on timescales of 10 ks to 1 Ms became possible and major progress was achieved in the collection of scientific data with respect to previous experiments. The first satellite dedicated entirely to X-ray astronomy, UHURU, was launched in 1970 (Jagoda et al., 1972) and for the first time mapped the entire X-ray sky in the energy band 2 - 20 keV.

The Einstein observatory, launched in November 1978, featured a Wolter Type-I grazing incidence telescope (0.1 keV - 4 keV) and was the first focusing X-ray telescope put into space (Giacconi, 1980). With its two arcseconds angular resolution, a field of view (FOV) of 25 arcminutes and a sensitivity several hundred times greater than any mission before (see *Fig. 1.5*), it was capable of detecting faint sources and of imaging extended objects as well as diffuse

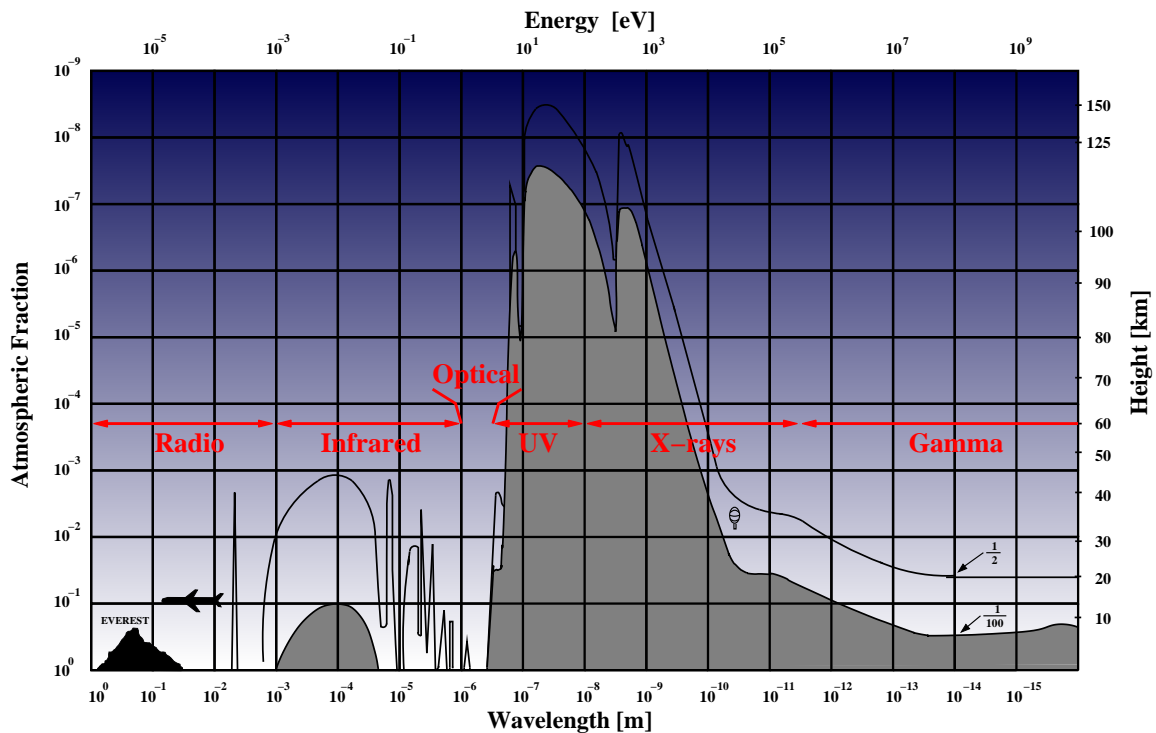


Figure 1.1: Attenuation of electromagnetic radiation at different heights in the Earth's atmosphere; reproduction of a figure from Giacconi et al. (1968). The grey area marks the region where less than 1% of the original flux can be measured, the solid line above identifies the height in which $\sim 50\%$ are still detectable.

emission. Now thousands of sources were discovered (Harris et al., 1993) and high resolution spectroscopy was available for the first time. This completely changed the view of the X-ray sky.

For the European Space Agency's X-ray Observatory Satellite, EXOSAT (see Taylor et al., 1981), a highly elliptical orbit of 90 hours was selected, so that continuous observations of X-ray sources, lasting several days without disturbing Earth occultations, were possible. This allowed to study the timing behaviour of many X-ray sources, triggering the discovery of their bursting activity and in some sources also that of Quasi Periodic Oscillations. Eventually, the German X-ray satellite ROSAT (ROentgen SATellite; see Truemper, 1982) was launched on June 1, 1990 and operated for almost 9 years. The survey obtained by ROSAT was the first X-ray all-sky survey (0.1 - 2.5 keV) using an imaging telescope with an X-ray sensitivity about a thousand times better than that of UHURU and the resulting catalogs holds more than 150.000 objects (Voges et al., 1999, 2000). In the pointing phase following the survey, ROSAT made deep observations of selected objects and discovered a wide variety in their nature - from ordinary stars, white dwarfs, neutron stars, black holes, supernova remnants, active galactic nuclei to hot gas in interstellar and intergalactic medium.

These now historic experiments (see also Fig. 1.5 and Table 1.1) have contributed much to our view of the universe, as they discovered it to be full of high energy phenomena that are

sometimes underlying rapid and/or periodic variations. Their discoveries and achievements are the motivation behind today's effort to build even more efficient telescopes, covering wider energy ranges with a higher resolution than before, as the field of X-ray astronomy is still full of surprises and many phenomena are still waiting to be detected.

1.2 Observational Techniques in X-ray Astronomy

The following sections give a short introduction to selected imaging techniques and detectors used in present X-ray and γ -ray instruments. The list is far from being complete and only introduces those concepts that are referred to in subsequent chapters.

1.2.1 Non-Focusing Imaging Techniques

The field of view (FOV) of X-ray detectors can be constrained to the desired angle by a collimating tube constructed of heavy X-ray absorbing material. In the most basic case, such a *collimator* allows to map the sky even with a non-imaging detector, consisting e.g. of a scintillating material and a photomultiplier. The FOV is then given by the angle at which the collimator reduces the incoming flux to 50%. The length of the tube, which would necessarily increase when higher resolutions (of the order of 1°) and thus smaller FOVs are desired, can be reduced to a more compact geometry by a honeycomb structure of smaller tubes (see *Fig. 1.2, left*), but not without loss of sensitive detector area due to the collimator's structure.

Although the FOV is reduced to small angles by a collimator tube and the X-ray background from other directions is effectively rejected, it is not possible to distinguish different sources within the field of view. This can be achieved, also with a non-imaging detector, for instance, by modulating the incoming flux with two grids of tungsten wires at different distances in front of the detector (*Fig. 1.2, middle*). Such a *rotation modulation collimator* was first proposed by Mertz (1967). Sources at various positions within the field of view are attenuated periodically in a unique way, corresponding to their angle to the line of sight. When the two grids are rotated against each other - seen from the restframe of the collimator - the sources appear to cross the bars with different frequency and phase on their way around the line of sight. Finally, the detector count rate is a superposition of the thus modulated lightcurves of all the sources within the FOV. The distance of a source from the line of sight can later be reconstructed from its signal's period and the azimuth can be found by analyzing the phase shift.

An imaging technique which is commonly used today in the hard X-ray band is that of the coded-mask camera. It was proposed independently by Ables (1968) and Dicke (1968). A coded-mask telescope basically consists of the mask, i.e. a plate with areas that are transparent or opaque to the observed photons and which are distributed in an optimized, non-redundant pattern - and a position-sensitive detector at a certain distance below (*Fig. 1.2, right*). Photons from the FOV then project the mask onto the detector and this projection has the same coding as the mask pattern, but is shifted relative to the central position corresponding to the direction of the incoming photons.

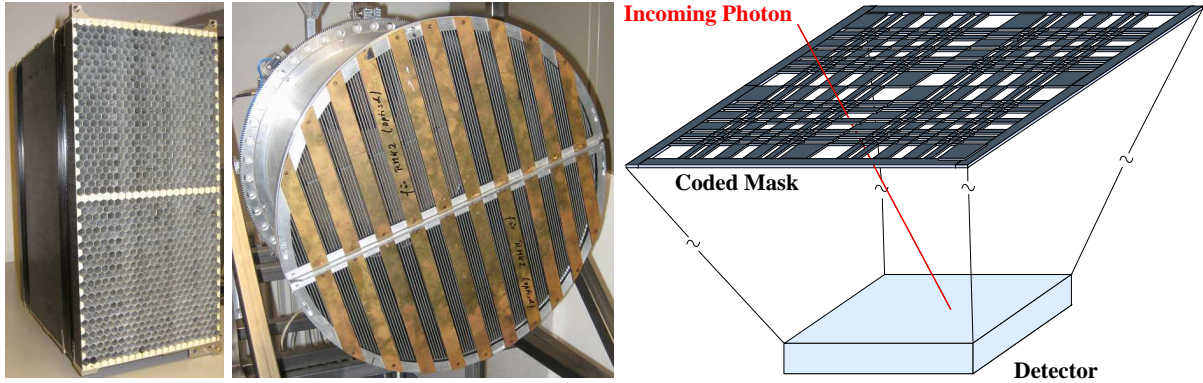


Figure 1.2: *Different imaging techniques used in high energy astrophysics (left to right): honeycomb collimator, rotation modulation collimator, principle of coded aperture imaging.*

The intensity of the projections encodes the intensity of the sources at their respective positions. After a given exposure time, the accumulated image of the detector is decoded to a sky image by inverting the coding equation 1.1, for which different methods exist (Skinner, 1995).

$$D(x, y) = M(x, y) \times S(x, y) \quad (1.1)$$

In other words, the distribution D on the detector results from folding the sky image S with the aperture modulation (i.e. the mask) M , whereas x and y are the coordinates in the respective planes. To reconstruct the original sky image, the detector distribution is usually 'unfolded' using a computer.

The imaging quality of the camera is determined by the type of mask pattern, the quality and resolution of the detector, the design of the camera (distance between mask and detector, mask and detector sizes) and the photon statistics. The resulting sky image is subject to uncertainties that arise because of the presence of background from the sky within the FOV and because of the detector background that is due to incident charged particles and secondaries generated locally in the camera. With a tungsten coded-aperture mask, located at 3.2 m above the detection plane, the IBIS instrument on board the INTEGRAL satellite reaches angular resolutions of 12' FWHM and typical source location accuracies of $< 1'$ (Winkler et al., 2003).

1.2.2 Focusing Techniques

The use of X-ray focusing mirrors in combination with position sensitive focal plane detectors significantly increases the instrument sensitivity by concentrating the flux from a large area to a tiny region. This leads to small detector sizes and therefore low background and a high signal-to-noise ratio (see also Equation 1.7).

An effective solution for focusing X-rays with mirrors was proposed by Wolter (1952) in the context of microscopes. He showed that in order to achieve a high imaging quality over

an extended field of view, the X-rays have to undergo two successive reflections from either a paraboloid/hyperboloid (see Fig. 1.3) or paraboloid/ellipsoid combination of mirrors which are mounted in a coaxial and confocal arrangement (Aschenbach, 1985). In 1961 the first astronomical X-ray collector was launched, using a combination of a polished glass paraboloid and hyperboloid with an effective area of 1 cm² (Giacconi et al., 1981).

Reflection on the mirrors occurs only for incidence angles below the critical angle for total reflection θ_c , whose relation to the index of refraction between the vacuum and the mirror material can be derived from Snell's law:

$$\frac{\sin \alpha_{1,c}}{\sin 90^\circ} = \frac{n_1}{n_2} := n \Rightarrow \sin \alpha_{1,c} = n \quad (1.2)$$

With $\theta := 90 - \alpha_1$ follows $\cos \theta_c = n$. From this it can be deduced that total reflection is only possible with $n < 1$. The refraction index between vacuum and material for a perfect mirror with no absorption is given by:

$$n = 1 - N_A \frac{Z \cdot r_e}{A \cdot 2\pi} \cdot \rho \cdot \lambda^2 := 1 - \delta \quad (1.3)$$

Where N_A is Avogadro's number, r_e is the classical electron radius, Z the atomic number, A the atomic weight, ρ the mass density and λ the wavelength.

The critical angle for X-ray reflection is therefore $\cos \theta_c = 1 - \delta$. As in this case $\delta \ll 1$, we can approximate $\cos \theta_c \approx 1 - \theta_c^2/2$ and finally get in the case of heavy elements, where Z/A is about 0.5:

$$\theta_c = \sqrt{2\delta} \approx 5.6' \cdot \sqrt{\rho[g/cm^3]} \cdot \lambda[nm] \quad (1.4)$$

The critical angle θ_c is thus directly proportional to the square root of the density ρ of the reflecting material and inversely proportional to the incoming photon energy. This means that for X-rays with a wavelength around 1 keV, θ_c is about one degree. For energies above, this angle becomes even smaller. Small reflection angles result in large focal lengths as the slope angle of the first mirror element should approximate the critical angle for rays that are parallel to the optical axis and the ratio of aperture size $2r$ to focal length f is determined by this slope angle α (Friedrich, 2008).

$$r/f = \sin 4\alpha \quad (1.5)$$

For small slope angles, the projected geometrical area of a mirror shell is only a thin annulus, much smaller than the polished surface. The technique of nesting several mirror shells with the same focal length and the same optical axis is therefore applied to enlarge the collecting area while keeping the mirror module as compact as possible.

As shown, for example, in Malaguti et al. (2005), the effective area for a Wolter-I multi-shell telescope system that totally fills the open volume inside the outermost shell is then

$$A_{eff} \propto f^2 \cdot \theta_c^2 \cdot R^2 \quad (1.6)$$

Thus the effective area for a given focal length can be optimized mostly by increasing the mirror reflectivity or the critical angle by choosing the appropriate materials. Very dense and reflective material coatings like gold (XMM-Newton) or iridium (Chandra) are usually applied to increase θ_c and enlarge the effective area. With four iridium mirror shell pairs and an aperture diameter of 1.2 m, the Chandra observatory reaches an effective area of 1100 cm² and an on-axis resolution of 0.5" (see Table 1.1). However, an immense advantage can be attained when the focal length is enlarged. This allows *geometrical* access to reflection at small angles, resulting in a much larger effective area.

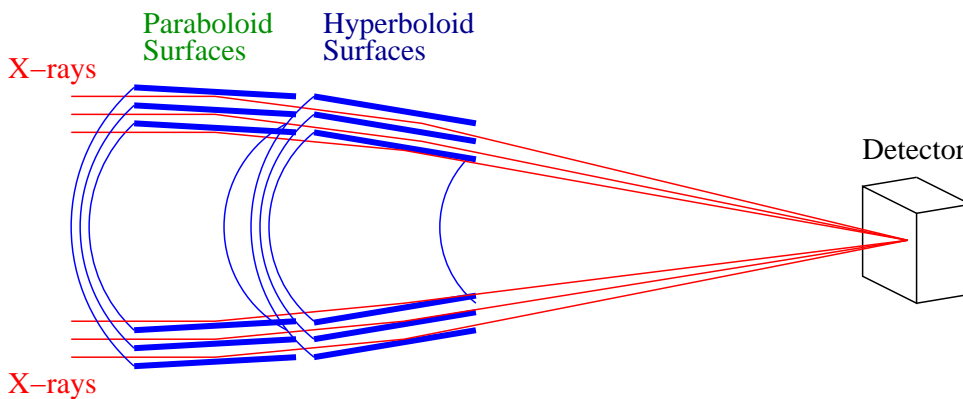


Figure 1.3: Reflection of X-rays on a Wolter Type-I telescope

1.2.3 Current Detector Types

In X-ray astronomy, detectors are designed to measure individual photons with the aim to reconstruct their incoming direction (images), energy (spectra) and the time of arrival of the photon. Some experiments are also able to measure the polarization angle of the incoming photons.

The illustration on the left in Fig. 1.4 explains the operation principle and the advantages of pn-CCD detectors, which have been the most successful focal plane instruments in recent years. PN-CCDs are backside-illuminated; their unstructured radiation entrance window enables an unobstructed high quantum efficiency from the near IR to the X-ray band. Incoming radiation generates electrons and holes on interaction with the fully depleted silicon substrate. The average energy required to form an electron-hole pair is 3.7 eV at -90°C (Strüder et al., 2001), which makes high resolution spectroscopy of the order $E/\Delta E \approx 50$ possible. Electric fields applied to the detector separate the charges, so the electrons drift to the potential minimum under the transfer registers, while the positively charged holes are absorbed on the backside. The electrons captured in the potential wells below the registers can later (after a certain exposure time)

be transferred by shifting the potentials towards the edge of the CCD. The readout electronics terminates each CCD line with a readout amplifier.

In contrast to MOS-CCDs, the transfer registers of a pn-CCD are formed by pn-junctions. This allows for a higher radiation hardness, faster transfer modes and more storage capacitance. In order to perform imaging X-ray spectroscopy, the CCD must be operated in such a way that only one photon hits a detector pixel per exposure and readout cycle. If that is not the case due to a high local photon flux from a bright source, the associated energy of an event corresponds to the sum of the occurred interactions and cannot be disentangled. This situation is commonly referred to as *pile-up* and fast readout cycles are required in order to avoid it and to be able to resolve phenomena happening on timescales even below 1 ms.

Photons that hit the CCD during the transfer process are misplaced in their position and thus degrade the scientific performance. A newly developed *frame-store CCD* from the Semiconductor Laboratory (HLL) of the Max-Planck-Institute for Extraterrestrial Physics in Garching (MPE) largely reduces these so-called *out-of-time events* with an additional shielded pixelized area, under which the generated charges are quickly transferred before they are read out at the usual speed.

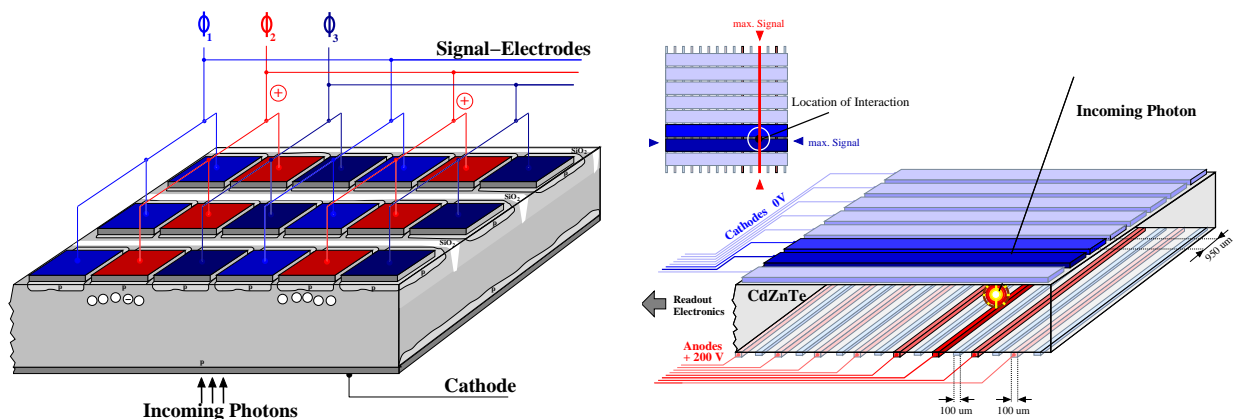


Figure 1.4: Illustration of the detection principle for a pn-CCD (left) and a crossed-strip detector. In both techniques, the incoming photons generate electrons and holes, which are then driven to opposite sides (top and bottom) by a strong electric field. In a CCD, only the electrons are gathered under a pixelized structure on the top and then transferred to a readout electronics on the side of the chip. In a crossed-strip detector, the signals of the electrons and holes are directly measured as fluctuations in the anode and cathode voltage of the respective strips (illustrations by T. Schanz).

Another way to obtain information about the location of interaction of X-rays in monolithic semiconductors is to use orthogonal anode and cathode strips on the top and bottom of the crystals to separate the charges (Fig. 1.4, right). The signals of the electrons and holes can then be measured with high timing precision as fluctuations in the anode or cathode voltage of the strips close to the interaction. Thus, with 50 μm wide electrodes and a 100 μm gap in between,

the intrinsic spatial resolution of e.g. CdZnTe or Ge semiconductor crystals can be covered sufficiently. CdZnTe is often used in such *cross-strip detectors*, because it features a very good energy resolution while maintaining good detection efficiency over a large energy range (usually 5 - 200 keV). The combination of these properties with the ease of packaging and handling and the lack of severe cryogenics requirements yields advantages over the scintillators, gas, and Ge detectors previously used in the hard X-ray range.

1.3 An Overview of Modern X-ray Observatories

The American Advanced X-ray Astrophysics Facility, now called **Chandra**, was launched on July 23, 1999 (Weisskopf et al., 2002). With a mirror module that consists of four nested Wolter shell pairs with a focal length of 10 m, it reaches an unprecedented spatial resolution of 0.5 arc-seconds (about five times better than ROSAT). Both detectors (a micro channel detector similar to the HRI on board ROSAT and an X-ray CCD camera) can be used in connection with transmission gratings for higher resolution spectroscopy.

Chandra's European counterpart is the European Space Agency's **XMM-Newton** (see also Chapter 3), which was launched on December 10 of the same year and is equipped with three Wolter mirror systems, each consisting of 58 nested mirror shells with a focal length of 7.5 m (Jansen et al., 2001). With its large collecting area of 1.500 cm² per mirror module, the European Photon Imaging Cameras (EPIC) and a spectrometer (RGS) located in the focal plane, it is dedicated to highly-resolved X-ray spectroscopy and time variability studies. An overview of the instrumental parameters of XMM-Newton and the observatories described in the following are also given in Table 1.1.

ASTRO-E2 ('**Suzaku**'; Kelley, 2004; Mitsuda et al., 2004) is the fifth in a series of Japanese X-ray astronomy satellites and was developed by an international cooperation between the United States and Japan. It is equipped with three instruments to perform broad band observations and high resolution spectroscopy over a wide energy range from soft X-rays to gamma-rays (0.4 - 600 keV). There are four X-ray Imaging Spectrometers (XIS) on board, each with a 1024 x 1024 pixel CCD. The Hard X-ray Detector (HXD) is a non-imaging instrument that uses scintillator crystals to detect radiation. The third instrument is a new type of X-ray spectrometer (XRS), which has an energy resolution that is an order of magnitude better than those of previous instruments. This device detects individual X-ray photons thermally by a phase transition in the detector material and is thus able to measure their energies with extraordinary precision and sensitivity. Unfortunately, a malfunction in the essential vacuum system in August 2005 (shortly after launch) caused the loss of the entire liquid helium required for cooling the instrument.

The **INTEGRAL** (INTErnational Gamma-Ray Astrophysics Laboratory) satellite, launched in 2002, is a gamma-ray mission under the supervision of ESA (Winkler et al., 2003). Its science payload consists of the spectrometer SPI and the imager IBIS, supplemented by the X-ray monitor JEM-X. INTEGRAL's main instruments make use of the coded mask technique to at-

tain the position information of sources in the sky. Due to the technological improvements since the launch of the Compton Gamma-Ray Observatory (**CGRO**), the measurements combine an angular resolution and sensitivity never reached before in the gamma-ray band.

The Rossi X-ray Timing Explorer (**RXTE**) satellite provides us with the unique opportunity to monitor the timing behaviour and variability of astronomical X-ray sources with unprecedented time resolution on scales from months to microseconds. It was launched in December 1995 and carries two pointed instruments - the Proportional Counter Array (PCA) and the High-Energy X-ray Timing Experiment (HEXTE) - that cover an energy range from 2 - 250 keV and an All Sky Monitor (ASM) that scans about 80% of the sky, allowing uninterrupted monitoring at time scales of 90 minutes or longer (Bradt et al., 1993).

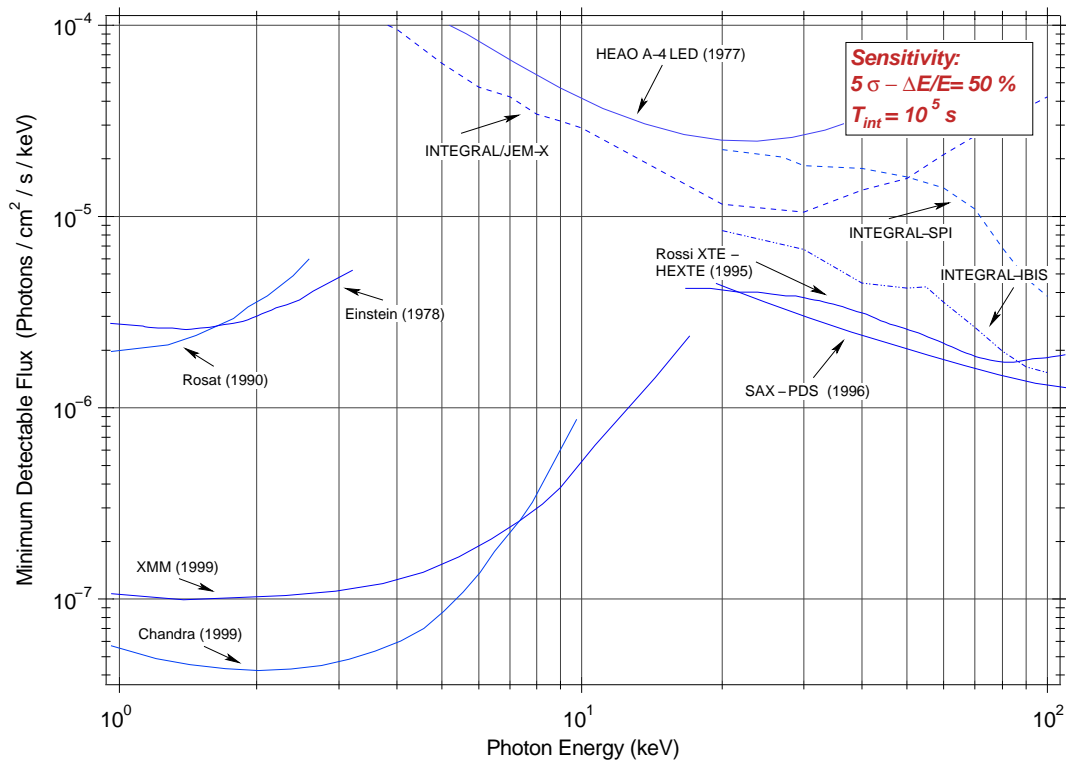


Figure 1.5: Comparison in sensitivity of the historic and present X- and gamma-ray observatories mentioned in this chapter. The remarkable leap in sensitivity in the 1-10 keV band achieved with XMM-Newton and Chandra and the lack of a comparable instrument in the 10-100 keV range are clearly visible.

As the results of the observations performed by the above missions constantly change and improve our knowledge of the universe, the perspective for X-ray astronomy is exciting indeed. A series of future space-based observatories is currently under development. These will be launched soon, in order to bridge the gaps between existing missions and to increase sensitivity and resolution capabilities to even fainter sources.

The Gamma-ray Large Area Space Telescope (**GLAST**) is an international observatory that was recently launched on June 11th and will study astrophysical sources with its two instruments, the GLAST Burst Monitor (GBM) and the Large Area Telescope (LAT). The GBM consists of 14 scintillation detectors, which will detect sudden rises in photon flux in an energy range from 8 keV to 30 MeV. The LAT is an imaging gamma-ray detector in the range from 30 MeV to 300 GeV (Ritz et al., 2007).

The extended ROentgen Survey with an Imaging Telescope Array (**eROSITA**) X-ray telescope is currently developed under the leadership of the MPE (Predehl et al., 2006). It will be launched on board of the Spectrum-RG satellite (*see also Chapter 8*) in the next years. Consisting of seven individual mirror modules and seven framestore-CCD cameras, it will perform the first imaging all-sky survey in the low energy X-ray range up to 12 keV with an unprecedented spectral and angular resolution.

Simbol-X is a French-Italian mission with German participation that will use for the first time focusing mirrors for an energy range from 0.5 to 80 keV. The necessary long focal length is obtained by having the mirrors and the detectors fly in formation on two separate spacecraft at a distance of 20 m. After its launch in 2014, Simbol-X will thus be able to extend the imaging quality and sensitivity already obtained with XMM-Newton up to the hard X-ray range. The prediction of the performance of Simbol-X with respect to the detector background is part of this thesis and the mission details are introduced in the following (*see Chapters 4 and 5*). A mission with a similar objective, the New X-ray Telescope (**NeXT**), is developed in Japan for a launch in 2010. With only one satellite, which has an extensible optical bench, a final focal length of 12 m will be achieved. The instrument also makes use of the stacked detector concept with a Soft- and a Hard X-ray Imager (Kunieda et al., 2006).

True focusing of X-rays in the energy range of 10 - 100 keV will further help us to explore extreme processes in the universe in a spectral region where non-thermal emission from cosmic X-ray sources dominates. However, common to all projects is the need for a low intrinsic detector background, so that the few counts received from a source are not lost in the background noise and a high sensitivity can be maintained preferably over the whole energy range of the instruments.

1.4 On the Importance of a Low Detector Background

In the typical radiation environment that is present in an orbit around the Earth, the usually rather weak cosmic X-ray sources have to be detected in the presence of a very strong background. Despite the increase of sensitivity in astronomical observations in the soft X-ray band, which has been achieved by the use of imaging telescopes, the background generated in the detectors is still a major issue nowadays and a lot of work is dedicated to its minimization (*the different origins and the composition of this background are introduced in subsequent chapters for the respective missions*). With today's more sophisticated instruments that feature a low background and short deadtimes, a typical observation yields a higher signal-to-noise ratio and

Table 1.1: An overview of instrument parameters of historic and modern X-ray observatories.

Satellite	Launch	Instrument	Energy Band (keV)	Spectral Resolution	Angular Resolution	Field of View
UHURU (SAS-1)	12.12.1970	proportional counters	2 - 20		30'	0.52°
Einstein (HEAO-2)	12.11.1978	IPC (Imaging Proportional Counter) HRI (High Resolution Imager) SSS (Solid State Spectrometer) FPCS (Focal Plane Crystal Spectrometer) MPC (Monitor Proportional Counter) OGS (Objective Grating Spectrometer)	0.4 - 4 0.15 - 3 0.5 - 4.5 0.42 - 2.6 1.5 - 20 0.15 - 3	E/ΔE: 3 - 25 E/ΔE: 50 - 1000	1' 2"	75' ∅ 25' ∅ 6' 1.5°
EXOSAT	26.05.1983	CMA (Channel Multiplier Array) PSI (Position Sensitive Detector) TGS (Transmission Gratings) ME (Medium Energy Proportional Counter) GSPC (Gas Scintillation Proportional Counter)	0.05 - 2.0 1 - 50 2 - 20		18"	2° ∅ 2° ∅ 2° ∅ 45'
ROSAT	01.06.1990	PSPC (Position Sensitive Proportional Counter) HRI (High Resolution Imager) WFC (Wide Field Camera)	0.1 - 2.5 0.1 - 2.5 0.062 - 0.206	E/ΔE: 1 - 4	2.5"	2° ∅ 38' 5° ∅
CGRO	05.04.1991	BATSE (Burst And Transition Source Experiment) OSSE (Oriented Scintillation Spectrometer experiment) COMPTEL (Compton Telescope) EGRET (Energetic Gamma-Ray Experiment Telescope)	20 - 1000 50 keV - 10 MeV 800 keV - 30 MeV 30 MeV - 10 GeV		< 1°	full sky
RossiXTE	30.12.1995	PCA (Proportional Counter Array) HEXTE (High Energy X-ray Timing Experiment) ASM (All Sky Monitor)	2 - 60 15 - 250 2 - 10	18% at 6 keV 15% at 60 keV	1°	1° 1°
Beppo-SAX	30.04.1996	LECS (Low Energy Concentrator Spectrometer) MECS (Medium Energy Concentrator Spectrometer) HPGSPC (High Pressure Gas Scintillator Prop. Counter) PDS (Phoswich Detector System) WFC (Wide Field Camera)	0.1 - 10 1.3 - 10 4 - 120 15 - 300 2 - 30		1.5' 75" 5'	37' ∅ 56' ∅ 1.3° 20°
Chandra (AXAF)	23.07.1999	ACIS (AXAF charge Coupled Imaging Spectrometer) HRC (High Resolution Camera) HETG (High Energy Transmission Grating) LETG (Low Energy Transmission Grating)	0.2 - 10 0.1 - 10 0.5 - 10 0.08 - 6	E/ΔE: 20 - 50 E/ΔE: 60 - 1000 E/ΔE: 30 - 2000	0.5"	16' ∅ 30' ∅
XMM-Newton	10.12.1999	EPIC-MOS 1+2 (European Photon Imaging Camera) EPIC-pn RGS (Reflection Grating Spectrometer)	0.1 - 15 0.1 - 15 0.35 - 2.5	E/ΔE: 20 - 50 E/ΔE: 20 - 50 E/ΔE: 200 - 800	6" 6"	33' ∅ 27.5' ∅ 5'
INTEGRAL	17.10.2002	IBIS (Imager on Board the INTEGRAL Satellite) SPI (SPectrometer for INTEGRAL) JEM-X (Joint European X-ray Monitor)	15 keV - 10 MeV 20 - 8000 3 - 35	E/ΔE: 500	12' 2° 3'	9° 16° 4.8°
Suzaku (Astro-E2)	10.07.2005	XRS (X-ray Spectrometer) XIS (X-ray Imaging Spectrometer)	0.3 - 12 0.2 - 12	6.5 eV at 6 keV 130 eV at 6 keV		2.9' 18'
GLAST	11.06.2008	LAT (Large Area Telescope) GBM (GLAST Burst Monitor)	20 MeV - 30 GeV 8 keV - 25 MeV	E/ΔE > 10	0.1°	2.4 sr 8.6 sr
NeXT	sched. 2010	SXT (Soft X-ray Telescope) HXT (Hard X-ray Telescope) WXI (Wide band X-ray Imager)	0.1 - 80 0.1 - 80 0.1 - 80	6 eV at 6 keV		
Spectrum-RG	sched. 2011	eROSITA (extended ROentgen Survey with an Imaging Telescope Array) ART-X (Astronomical Roentgen Telescope) LOBSTER (all sky monitor) GRB (Gamma-Ray Burst detector)	0.2 - 12 3 - 30 0.1 - 40	130 eV at 6 keV 1.2 keV at 60 keV E/ΔE ~ 5	< 15"	0.467 deg ² 10° 22.5°

thus more significant science output. Furthermore, more objects (or larger regions, respectively) can be covered in a survey, as shorter observation durations are necessary to detect the sources.

The minimum detectable flux of a weak source for an instrument that consists of a detector with a quantum efficiency of $\epsilon(E)$ counts per photon and an effective area of $A_{eff}(E)$ for collecting source photons, can be expressed in photons \cdot cm $^{-2}$ \cdot s $^{-1}$ \cdot keV $^{-1}$, and is usually calculated according to the following formula, adapted from Fraser (1989):

$$F_{min} = n_{\sigma} \cdot \frac{\sqrt{B \cdot A_{det}}}{\epsilon \cdot \eta \cdot A_{eff} \cdot \sqrt{T_{int} \cdot \Delta E}} \quad (1.7)$$

n_{σ} is the desired statistical significance of a detection, T_{int} is the measurement time, A_{det} the area of the detector (relevant for the background) that encompasses a fraction of usually $\eta = 50\%$ of the source photons and B the background flux in the detector. Equation 1.7 strongly emphasizes the importance of the background, as the minimum detectable flux for a given n_{σ} is hence the flux which produces in the measurement time a count that is n_{σ} standard deviations of the background B above the mean background. Therefore, besides the size of the effective area and the detector efficiency, it is the background that finally determines the sensitivity and performance of the instrument.

One of the key systems to reduce a large fraction of the detector background is an **active anticoincidence detector** (AC). It is usually designed to surround the experiment in order to detect events from impinging charged cosmic ray particles. In the case of coincident triggering of the AC and the X-ray detector, the event that was registered on the detector is discarded as a background event. Due to their high effectivity in reducing the instrument background, anticoincidence schemes are implemented in a large number of X-ray and γ -ray experiments.

Although the use of CCD detectors as focal plane instrumentation improved the performance (regarding energy and position resolution) of X-ray instruments by a factor of 5 to 10 compared to the previously used proportional counters (Pfeffermann et al., 2004a), the detector background in these instruments is again higher, because anticoincidence detectors cannot be applied in such a mission. As the timing accuracy of an event in a CCD detector is given by the integration and readout cycle time, discarding such a measured *frame* (~ 70 ms in XMM-Newton's FF mode) when in coincidence with a signal from the AC would result in a unacceptably large downtime. Even with the faster frame times of the Active Pixel Sensors for Simbol-X (2μ s per row), as described in Chapter 4, it still remains quite a challenge to provide a small but effective anticoincidence tagging scheme.

As events generated by minimum ionizing particles on the CCDs can be easily distinguished from valid events by means of an upper threshold and/or an **event pattern filter** (see Chapter 7), the instrument's main background component is produced by interactions of cosmic ray particles in the materials surrounding the detector. The resulting events, generated by X-rays in the correct energy range, cannot be separated from events due to X-rays collected by the mirrors.

However, a **graded-Z shield** close to the detector provides an effective tool to absorb and/or to shift the energy of those locally generated X-rays down to lower energies, i.e. usually below the detection threshold of the detector. In order to construct such a shield, materials with descending atomic numbers Z (outside to inside) are stacked together. As the radiative energy loss due to bremsstrahlung of charged particles is proportional to Z of the absorbing material and the fluorescence yield of the elements also drops to lower Z s, such a shield can be optimized to exactly fit its purpose and to leave no detectable X-ray fluorescence of the higher order materials. With innermost materials like B_4C , a large fraction of the re-emitted energy is also carried away by Auger electrons, which can be stopped in very thin layers of material, e.g. in the passivation layers of CCDs (Pfeffermann et al., 2004b).

As reported in Chapter 3, the materials which are used in a detector's front-end electronics can also be a strong source of X-ray fluorescence (in simulations and in in-orbit measurements) due to their proximity to the detector. Consequently, they have to be shielded like all other materials in the FOV of the detector.

It is in the context of this challenge - to reduce the ever-present instrument background - in which the simulations and results described in this work have been regarded by the instrument scientists as a valuable and important input to the design of the Simbol-X and eROSITA missions.

The aim of this thesis is to describe in detail how Monte-Carlo simulations of the physics processes and interactions taking place in a space-based X-ray detector as a result of its orbital environment are capable of explaining the measured detector background of already existing missions. It will be demonstrated that these simulations are therefore an excellent tool in predicting the background of future X-ray observatories.

At the heart of the simulations described in this work is the GEANT4 Monte-Carlo simulation toolkit. Its design and capabilities are introduced in the next chapter. An environment has been created implementing the toolkit in order to simulate the background present in in-orbit X-ray observatories. With the aim to prove the performance of this environment, results of such background simulations for the pn-camera of XMM-Newton are presented and compared to actual measurements in Chapter 3. For the upcoming missions Simbol-X and eROSITA, an estimate of their detector background is calculated on the basis of simulations and predictions for their scientific performances are made thereupon (Chapters 4, 5 and 8). In Chapter 6, another comparison between simulation and measurement is presented for the detection of low-energy X-ray fluorescence photons created by the high-energy detector in a stacked detector setup. Last but not least, a prototype for a digital event-preprocessing device to further reduce the background and the necessary telemetry rate is presented in Chapter 7. Conclusions and a summary of the thesis can be found in the final chapter.

All simulations presented in this thesis are done with the same environment that was developed in the progress of this thesis for Simbol-X. The sequence of chapters in this thesis was

chosen after some considerations, however, to first give an impression of the quality of the results obtainable with the code and then present the predictions for future observatories. This approach appeared more convincing, although the reader is in this way sometimes referred to Chapter 5 for a more detailed introduction to the simulation environment. Another benefit of this structuring is that work, which was done for the same project, is presented in a coherent way.

The GEANT4 Toolkit

GEANT4 is a powerful and flexible Monte-Carlo simulation toolkit that provides libraries for *GEnerating ANd Tracking* of particles through matter and electromagnetic fields. In its current version, efficient functions are included, which allow the application developer to design detector geometries, make use of physics models, visualize complex particle tracks and generate detector *hits*. The embedded physics processes cover electromagnetic interactions of hadrons, ions, leptons and photons from 250 eV up to several PeV, hadronic interactions from thermal energies to 1 PeV and also the production and propagation of optical photons. Thus, it is suitable for an increasing user group doing research in a variety of domains like medical physics, space science and astrophysics, radiation protection and, of course, in the original domain of GEANT4: high energy and accelerator physics. The toolkit is continually being extended by the worldwide GEANT4 *Collaboration* and is freely available via the Web¹ at source code level (object-oriented C++). All of the above make GEANT4 the right tool to complement a simulation environment for investigating space-instrument background.

2.1 On Monte-Carlo Simulations

Monte-Carlo methods are distinguished from other simulation methods by being stochastic, that is, nondeterministic, in that they make use of (pseudo-)random numbers as opposed to deterministic algorithms. Such statistical sampling methods have already been applied even by the earliest pioneers of probability theory (e.g. in experiments like Buffon's needle² or works by William Gosset³). Enrico Fermi also used a statistical method in 1930 in the calculation of neutron diffusion, and later designed the *Fermiac*, a Monte-Carlo mechanical device, used in the calculation of criticality in nuclear reactors (Metropolis, 1987). A formal foundation for the Monte-Carlo method was developed by John von Neumann, who established the mathematical basis for *probability density functions* (PDFs) and pseudo-random number generators in collaboration with Stanislaw Ulam. Statistical methods were applied in the simulations for the Manhattan Project but became popular in the fields of physics and mathematics only after the war in the 1950s, when electronic computers became available. The designation 'Monte-Carlo' was coined by Nicholas Metropolis, Ulam and Fermi during their work on the Manhattan Project in reference to the casino in Monaco.

¹GEANT4 Website: <http://geant4.web.cern.ch>

²A question first posed in the 18th century by Georges-Louis Leclerc, Comte de Buffon: Drop a needle onto a floor made of parallel strips of wood (wider than the length of the needle). What is the probability that the needle will lie across two strips? It can be solved to derive a Monte-Carlo method (i.e. tossing the needle) to approximate π .

³William S. Gosset - English statistician, also known as Student and for his work on Student's t-distribution

Monte-Carlo methods directly simulate a physical process - there is no need to specify the differential equations that describe the behaviour of the underlying physical or mathematical system. In contrast to conventional numerical methods, the only requirement is that the system can be described by PDFs. A large number (depending on the desired variance of the result) of simulations are then performed, each by random sampling the PDFs, and the result is taken, for instance, as the average of all outcomes. In describing physical processes as PDFs (using experimental data or a theoretical model), we can sample an outcome from one of them and thus simulate the actual physical process. In order to simulate the interactions of a 10 MeV proton within a plastic scintillator detector, for example, it will be necessary to sample from a PDF that yields the distance such a proton travels in this particular material before suffering its first collision with a molecule of the detector.

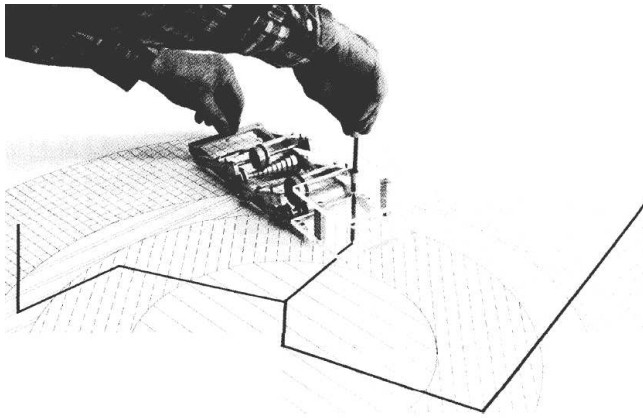


Figure 2.1: *The Monte-Carlo trolley or FERMIAC was invented by E. Fermi and was used to determine, among other things, the change in neutron population over time in numerous nuclear systems. The drums on the trolley were set according to the material being traversed, and random digits were used to choose between fast and slow neutrons, direction of motion and distance to the next collisions. The trolley was then moved across a two-dimensional drawing of the reactor assembly being studied. The trolley drew a track as it rolled, stopping for changes in settings whenever a material boundary was crossed (Metropolis, 1985).*

Monte-Carlo methods are especially useful in studying systems with a large number of coupled degrees of freedom and require, due to the involved uncountable numerical calculations, the use of a computer. They also need large amounts of random numbers, which led to the development of effective pseudo-random number generators. Today, Monte-Carlo methods have become very important in computational physics, astrophysics, physical chemistry, medicine and related applied fields (e.g. traffic flow, finance, and oil well exploration; Kok et al., 2006) and have diverse applications from complicated quantum chromodynamics calculations, designing heat and radiation shields to aerodynamic forming and computer graphics.

2.2 Introduction to GEANT4

The GEANT4 toolkit covers all aspects of a Monte-Carlo simulation process: starting with the geometry of the system, the materials involved, the fundamental particles of interest, the tracking of particles and secondaries through materials and external electromagnetic fields, the physics governing particle interactions, the response of the detector components, up to the generation of event data and the visualization of particle trajectories. The physics models that

handle the interactions of particles incorporate about all that is known thereof today and more-over continue to be refined and expanded. Different implementations of physics are possible - and some are already included in GEANT4 - facilitating alternative or altogether new modeling approaches. The toolkit is developed by a large international collaboration that is considered (in terms of size and scope of the code as well as the number of contributors) to represent one of the largest open software development projects (Agostinelli et al., 2003).

2.2.1 *Historic Evolution of GEANT4*

The first version of a 'detector description and simulating tool' with the name GEANT was written in the FORTRAN programming language in 1974 at CERN¹ as a framework for tracking particles through simple geometries (Agostinelli et al., 2003). The first step towards the complexity and scale of the current versions was taken when two independent studies, that were working on improving the original code (done at CERN and KEK²) were merged in 1993. The growing collaboration on the resulting project (named RD44) decided to adapt such (at that time) modern computing techniques as object-oriented programming and the C++ language for the development of the code. In 1998, the first production release was delivered and since then the number and variety of its applications has been increasing steadily. The GEANT4 Collaboration, which was established in January 1999, continues the development nowadays and provides documentation and support for the toolkit.

2.2.2 *Scientific Community*

With the widespread adoption of GEANT4 by scientists from different fields of physics, medicine and engineering to simulate their experiments, the formal structure of the GEANT4 Collaboration consists today of a steering board and an oversight board composed of scientists from many different laboratories and institutions. The daily technical work, however, is performed in working groups which are organized thematically according to the GEANT4 structure. These groups also provide the user support, maintain a Web-based user forum with sub-forums for the different fields of application and also a list of frequently asked questions on the GEANT4 website.

GEANT4 has a growing community of application developers. Among the flagship experiments that are well known for the adoption of GEANT4 code are, of course, the ATLAS detector and other detector simulations at the LHC³, experiments and projects at the Fermilab⁴ accelerators, the OpenGATE collaboration⁵ and the GLAST telescope.

¹Centre Européen pour la Recherche Nucléaire, Geneva, Switzerland

²National Laboratory for High Energy Physics, Tsukuba, Japan

³The Large Hadron Collider is a particle accelerator and collider located at CERN.

⁴The Fermi National Accelerator Laboratory near Chicago, USA

⁵GEANT4 Application for Emission Tomography, an application in the field of nuclear medicine

2.2.3 Pseudo-Random Number Generation in GEANT4

A vast amount of pseudo-random numbers are required at various stages all through a GEANT4 Monte-Carlo simulation. Depending on the application, they are used not only to sample from the PDFs of the applicable physics processes at each step, but also in many cases to simulate further detector behaviour, electronics response and most commonly to define the properties of the primary particles. This is effectively handled by using the *General Particle Source* module, introduced in Section 2.3 below.

Random number generation within GEANT4 simulations is done via the *HEPRandom* module, which originally has been a part of the GEANT4 kernel, but is today included in the CLHEP¹ package. It is the abstract interface to classes implementing different random *engines* and distributions. An *engine* executes the basic algorithm for pseudo-random number generation. The application designer can choose from one of several currently implemented engines:

- **HepJamesRandom**

This class implements the algorithm described in James (1990). It is the default random engine for all purposes unless the user sets a different one.

- **RandEngine**

A very simple engine using the *rand()* and *srand()* functions from the C standard library to implement a flat distribution.

- **DRand48Engine**

A random engine using *drand48()* and *srand48()* system functions from the C standard library for a flat distribution.

- **RanluxEngine**

The algorithm has been taken from the original FORTRAN77 implementation by Fred James (James, 1990), which provides five different 'luxury' levels, showing a different amount of correlation between consecutive numbers.

- **RanecuEngine**

Originally also written in FORTRAN77 as part of the MATHLIB HEP library, it uses a table of seeds that provide uncorrelated couples of seed values.

Only one random engine can be active at a time, but the user is free to change it or define and set up a new one.

¹The Class Library for High Energy Physics provides utility classes for numerical programming, vector arithmetic, geometry, pseudo-random number generation and more, targeted for high energy physics simulation and analysis software.

A set of random number distribution classes are defined in *HEPRandom* to allow sampling numbers according to specified predefined distribution algorithms. Depending on the application, the user is free to sample from the following highly configurable distributions:

- **RandFlat**
distribution class for flat random number generation
- **RandExponential**
class holds methods for shooting exponential distributed random values, given a mean
- **RandGauss**
holds methods for shooting gaussian distributed random values, given a mean and a deviation
- **RandBreitWigner**
distribution class for shooting numbers according to the relativistic Breit-Wigner distribution used to model resonances (unstable particles) in high energy physics
- **RandPoisson**
shoot numbers according to the Poisson distribution, given a mean

All engines require *seed values* as input parameters that identify an entry point into a sequence of random numbers and allow to repeat exactly the same sequence of events in a simulation for debugging purposes or to cross-check results. The current state of a random engine depends only on this seed value and the number of times its *shoot*-function was called during previous events. This number of callings is totally different for each event due to the stochastic nature of the simulation. However, the phenomenon creates a virtual interdependency among consecutive events. This effect has to be kept in mind when simulation code is parallelized to run simultaneously on different CPUs in one computer or on many computers in a network environment. In order not to lose this dependency (if desired) in such a case, one approach is to use a master random seed generator as an input to the random number generator of each sequential application (Cooperman et al., 2006).

Seen at this 'engine level', there is nothing 'random' about a Monte-Carlo simulation. All events are results of a long computation, that can be repeated at any time on any computer by using the same code and the same seed value.

2.3 Structure and Design of GEANT4 Simulations

GEANT4 is provided as a 'toolkit', which implies that the user assembles his simulation program of components taken from the toolkit and parts of his own code. Due to the size of GEANT4, the user contribution will almost in every case be the much smaller part, but GEANT4 is certainly far from being a standalone application.

As a result of the object-oriented design approach, GEANT4 has a very hierarchical and transparent structure. Many of the top-level categories and classes are also simple interfaces to the outside (e.g. for user input or the visualization of geometry and tracks) and can be considered and understood independently. Within *Geant4*, a simulation *run* is the largest unit of the simulation and consists of a sequence of *events* (i.e. generation of a primary particle) that share a common source, detector implementation and physics processes (see Fig. 2.2). An *event* represents the main unit of GEANT4 Monte-Carlo simulations. Before processing, it contains all information about the primary particle itself and the primary vertex (positional and time information). Afterwards, it holds detector *hits* generated by the simulation and the trajectories of all involved particles. As explained later, this information is only transitory and the user is responsible for collecting and storing this information.

GEANT4 provides the user with the possibility and the obligation to interface the simulation in a few essential *user classes*. Three of them are obviously mandatory: the *DetectorConstruction*, the *PhysicsList* and the *PrimaryGeneratorAction*. To construct a geometrical model of a detector and to define its sensitive elements that record information about *hits*, the user is offered special classes that assist in the construction of various geometric shapes and volumes as well as some that create and assign materials with user specified properties to them. In GEANT4, materials are made of elements, which in turn consist of isotopes. At each level of this hierarchy, the user can create his own materials/elements/isotopes or select the appropriate ones from the GEANT4 material database. Using the *G4Element* class, he can specify properties of the atoms like atomic number, number of nucleons, atomic mass, shell energy, as well as such quantities as cross section per atom. In using the *G4Material* class, the user is able to describe the macroscopic parameters of matter like density, state, temperature, pressure, radiation length, mean free path, etc. Molecules are implemented by specifying the number of each atom type or by giving the fractional mass of each component.

GEANT4 defines no default physics processes to be included in all standard simulations because it is considered impossible to provide a set of processes which apply to the demands of most situations and still allow for reasonable simulation runtimes. Instead, the user is required to specify in the *PhysicsList* all particles, processes (even the transportation process) and their respective parameters that seem relevant for the simulation (see Section 2.4 on GEANT4 physics below). The current GEANT4 distribution provides various examples to illustrate this selection.

There are different ways to implement the generation of primary particles in the *PrimaryGeneratorAction* class, but the most effective one is via the GPS module (Ferguson, 2000). The *General Particle Source* module is part of the GEANT4 toolkit and allows the user to select the kind of incident source (*primary*) particles as well as to specify their spectral, spatial and angular distribution. Multiple particle sources can also be specified. These specifications are usually assembled in macro-files but can also be accessed and changed via the command-line. The particle source can be either a beam or an emitting surface or volume (circle, annulus, ellipse, rectangle, sphere, ellipsoid, cylinder or parallelepiped). Emission can be restricted using a histogram to totally arbitrary angles. Finally, the user has to select one of the following further

customizable functions/models for particle energy: monoenergetic, linear, powerlaw, exponential, Gaussian, bremsstrahlung, Black Body, Diffuse Gamma Ray and arbitrary histogram.

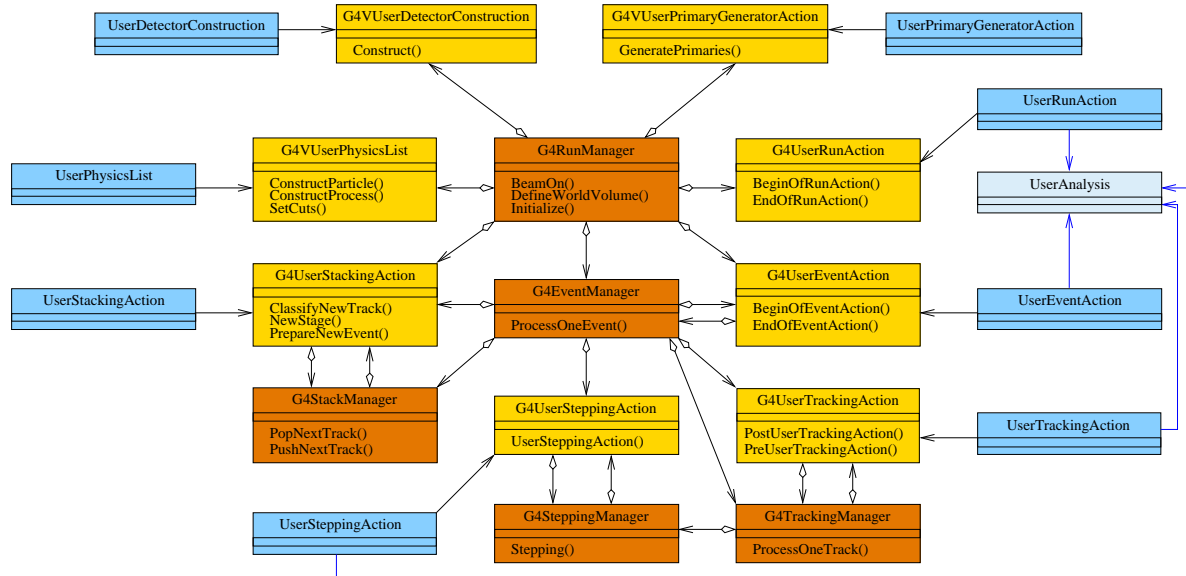


Figure 2.2: Structural scheme and class diagram of an exemplary simulation with GEANT4, displaying the user defined class implementations (blue) and their respective relations to the GEANT4 Manager- (red) and Action-Classes (orange).

Further optional user classes involve user interaction with the simulation process at various levels (see Fig. 2.2) in order to store information about interactions generated with each step, event or run that would otherwise be lost with the next respective instance.

2.4 The Physics Behind GEANT4

One of the design principles of GEANT4 is that its implementation of physics should be transparent and open to user validation. Its architecture is therefore modular, extendable and allows the user to understand and customize it by picking exactly the components he needs for a particular simulation. GEANT4 also allows multiple implementations of physics models to participate in every interaction or decay channel, and the application designer is free to select models by energy range, particle type or material of the interaction location. Data encapsulation and polymorphism¹ - there are public methods with the same name and the same parameter sets in all the objects - allow transparent access to the cross sections in interpolating either from a tabulated set or computing analytically from a formula.

¹the ability of objects belonging to different types to respond to method calls of the same name, each one according to a type-specific behavior

2.4.1 Implementation of Physics Processes

GEANT4 treats physics processes in a rather generic way: the tracking of particles neither depends on the particle type nor on the kind of physics process involved (including transportation). In GEANT4, a particle is considered transported by a special transportation process, rather than being self-moving. There is *no* grid; the length of a transportation step (for a particle at rest, this is a time step) is proposed by the physics processes and the respective material associated with the particle at that time. Each process has a *GetPhysicalInteractionLength* method that calculates the step length from the current position of a particle in space and time to its next. This calculation involves the probability of interaction based on the cross section information of the process. At the end of each step, a *DoIt* method is evoked, implementing the details of the interaction like changing the particle's energy, momentum, direction of movement and position as well as creating secondary particles if necessary. According to its nature, a physics process in GEANT4 applies changes to a particle either 1) *at rest* (e.g. decay), 2) *along step* (e.g. Cherenkov radiation), 3) *post step* (e.g. secondary particle production). In some special cases combinations of these are allowed (e.g. ionisation: energy loss and delta ray) (Geant4 Collaboration, 2006).

The following major physics process categories are provided by GEANT4:

- electromagnetic
- hadronic
- decay
- photolepton-hadron
- optical
- transportation

For the application of simulating the background of a space-borne instrument, electromagnetic and hadronic processes are the most significant of the above. Having been developed in the field of high-energy collider physics, GEANT4 distinguishes 'standard' electromagnetic processes from so-called 'low-energy' processes. At lower energies the atomic shell structure is more important for physics processes than it is at higher energies (Apostolakis et al., 1999). Therefore, the low energy processes make direct use of known shell cross section data, while the standard processes, that are optimized for high energy physics, rely on parameterizations of these data. The (in space science) therefore necessary low-energy data files and associated processes (see Fig. 2.3) have to be explicitly included into simulations in order to extend the accuracy of the photoelectric effect, Compton scattering, gamma conversion, ionization and bremsstrahlung down to 250 eV and to include valid physics (that can be used up to about 100 GeV) for such phenomena as Rayleigh scattering and X-ray production through fluorescence.

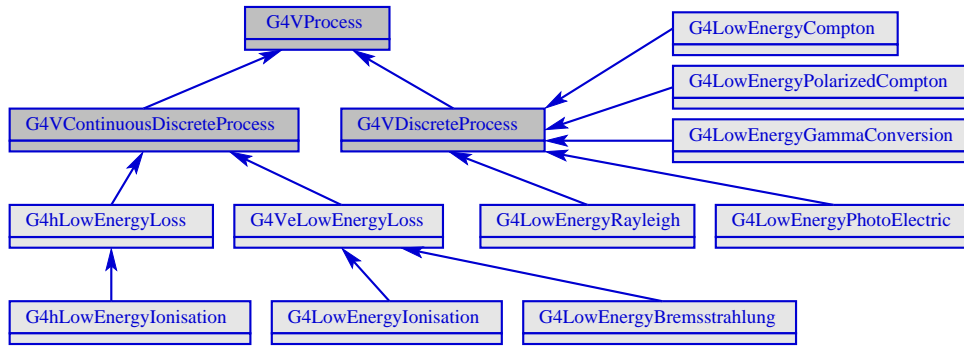


Figure 2.3: Class diagram of the low energy electromagnetic processes.

The total interaction cross section is derived from those library files by interpolating the cross sections given only for discrete incident energies according to Equation 2.1, taken from (Apostolakis et al., 1999).

$$\log(\sigma(E)) = \frac{\log(\sigma_1)\log(E_2/E) + \log(\sigma_2)\log(E/E_1)}{\log(E_2/E_1)} \quad (2.1)$$

with E_1 and E_2 being the closest lower and higher energy for which there are data available. The mean free path for interacting of a particle of energy E via a given process is given by:

$$\lambda = \frac{1}{\sum_i \sigma_i(E) \cdot n_i} \quad (2.2)$$

The sum is taken over all elements of the material composition, where n_i is the atomic density of the i -th element.

While generating the final state products after excitation by e.g. the photoelectric effect or ionization, an atom of the material in which the interaction has occurred is randomly selected and atomic relaxation is simulated.

2.4.1.1 Example: Atomic Relaxation

To give an example of how a low-energy physics process is simulated, this section will take a closer look at how atomic relaxation is handled in GEANT4 and how fluorescence photons are generated (as described in the GEANT4 Physical Reference Manual). The latter play an important role in the composition of the instrument background of existing X-ray detectors.

After being ionized by one of the above mentioned processes, an atom is assumed to have ejected exactly one electron, leaving a vacancy in a given subshell. The data describing the relaxation of atoms are taken from the Livermore Evaluation Atomic Data Library (see Perkins

et al., 1991), which contains the radiative and non-radiative transition probabilities for the subshells of the K, L, M, N shells as well as some of the O subshells for all elements from $Z=6$ through 100. For the time being, for $Z=1$ to 5 only a local energy deposit, corresponding to the binding energy of the vacant shell is simulated (with the exception of subshells of the O, P, and Q shells, where a photon is emitted at that energy in a random direction in 4π).

In all other cases, the simulation procedure is the following: An outer subshell is selected randomly by sampling from the relative transition probabilities. If the energy of the thus selected transition is larger than the user defined cut value (see *below*), a photon is created at the respective energy and randomly emitted in 4π . These steps are repeated for the newly vacant shell, and so forth.

Non-radiative relaxation can occur via the Auger effect, that has almost the same structure as the fluorescence process, with the difference that two shells need to be randomly chosen: one for the transition electron, that fills the vacancy and the other one is the shell generating the Auger electron. The Atomic Data Library's probability data are normalized to one for the sum of fluorescence and Auger.

2.4.1.2 Production / Range Cuts

Particles tracked by the GEANT4 kernel include photons, gluons, quarks, leptons, mesons, baryons and ions. However, when secondary particles are produced in an interaction and the range of these secondaries is less than a user defined *range cut* value, the process suppresses them and adds their energy to the energy deposited locally during, or at the end of the relevant step. This last point is important to guarantee the conservation of energy. A range is used rather than a threshold in energy-space to provide a more coherent concept for different materials and particles (Agostinelli *et al.*, 2003). The range cut is internally converted to an energy for the respective materials. Some electromagnetic processes, like δ -ray and bremsstrahlung production, require such a threshold to suppress the generation of large numbers of soft electrons and gammas in order to avoid 'infrared divergence', while in other cases the user may need to cut some particle types in certain volumes for optimization reasons. Therefore, cuts can always be specified for individual particle types and can be administered globally or only for selected volumes/regions. A study was performed in the context of this work on the trade-off accuracy vs. computing time and the global cuts for all simulations described here were refined from the default values to what appeared a more precise and still sustainable setting (see *Section 5.3.1*).

In some cases a process may have reasons to produce particles also below that threshold, as in the case of gamma conversion, where the positron is always produced for further annihilation, even at zero energy. Finally all particles are, once produced, tracked up to zero range; there are *no tracking cuts* in GEANT4.

2.4.1.3 *Simulation of Radioactive Decay*

Long term radioactivity produced by nuclear interactions and activation of materials represents a minor but tenacious contribution to the instrument background in space, as resulting detector events often occur outside the time-scales of the anti-coincidence measures. This contribution has been investigated in the case of Simbol-X (see *Chapter 5*) with the help of the Radioactive Decay Module of GEANT4 that is like the low-energy electromagnetic processes an optional extension of the toolkit. Further information on *Geant4* physics implementation can also be found in the appendix.

2.4.2 *Physics Validation*

A systematic validation of simulated data against corresponding reference data - both calculated and measured - is constantly pursued by the GEANT4 Collaboration. This concerns on one side the basic features of the toolkit's physics models: Quantities like cross sections, attenuation coefficients and stopping powers for electromagnetic models are compared to the National Institute of Standards and Technology (NIST) database, that is an authoritative reference in the field. For the domain of hadronic physics, simple geometries that allow to test single interactions with thin targets are used for the validation of individual models. On the other side, the collaboration and also the user group perpetually subject the toolkit's simulation results for large and complex experiments from all the different domains of physics research to thorough analysis and comparison with experimental data from test beams or ongoing experiments, before simulating new setups. This procedure has also been chosen for this work. The analyses all show GEANT4 results to be in good agreement with reference data (Amako et al., 2006; Allison et al., 2006). A list of published general GEANT4 validation results can be obtained from the GEANT4 publications website¹ and more specific results can be found on the websites of the respective GEANT4 working groups, accessible from here².

2.5 *Comprehensiveness and Possibilities of GEANT4*

Today, simulations have found their way into nearly all domains of science and engineering and are especially useful in estimating the performance and limits of projected devices. In the field of simulating physics processes, the GEANT4 toolkit is outstanding in its comprehensiveness and application range, encompassing all domains where particles need to be tracked, from astrophysics via particle physics to medical simulation tasks. This wide range, its transparent implementation of physics and the large user community make its usage in any project within these domains greatly appealing.

2.5.1 *Recent Developments*

Newly implemented physics models, corrections, user feedback as well as requests for new features lead to a constant release of GEANT4 updates and patches. A major version release is

¹<http://geant4.cern.ch/results/publications.shtml>, <http://geant4.cern.ch/results/results.shtml>

²http://geant4.cern.ch/collaboration/working_groups.shtml

issued about once per year. Though this ensures a quick reaction time for bugfixing, it is not always transparent if the implemented changes will affect particular simulation results. Within a group, that is working on the same project, it is therefore difficult to coordinate versions and patch levels of the many involved modules between coworkers in order to always attain comparable outcomes of simulations, resulting sometimes in the decision to 'freeze' an established version.

One of the latest features in the current version 9.0 is the first implementation of error propagation for tracks. In addition, the introduction of the Geometry Description Markup Language (GDML), an application-independent geometry description format based on XML, finally provides a geometry data exchange format for the existing applications. Eventually this will lead to interfaces between GEANT4 and existing CAD programs that are used to design the drawings of the experiment and in this way facilitate the exchange of geometry setups between the design and the simulation groups.

2.5.2 GEANT4 Applications in Space Science

The European Space Agency (ESA) encourages the use of GEANT4 Monte-Carlo code for studies in space related applications. GEANT4 is at present the standard Monte-Carlo code used by ESA for radiation transport analyses (Santin et al., 2003). As in recent years the space environment and astrophysics community has grown to become a substantial part of the GEANT4 users community, dedicated events and workshops are now periodically organized to gather the scientists working in this field and to support the exchange of expert knowledge. A website¹ is available, presenting the space user community and providing several useful resources as well as a list of experiments and publications. Examples mentioned there cover space electronics and space science detector systems, simulations of astronaut radiation hazards, Cosmic ray magnetospheric propagation analyses, microdosimetry, large-scale simulations requiring event biasing and GRID capabilities and general shielding optimization applications.

¹<http://geant4.esa.int>

Simulation of the XMM-Newton EPIC pn-Camera Detector Background

In this chapter the simulation of the background of one of the instruments on board of XMM-Newton, the pn-camera, is described. This was originally intended as only a first stage along the way to the Simbol-X simulation environment (see *Chapter 5*). As the background of the pn-camera has been thoroughly investigated and published since the launch of the XMM-Newton observatory, the results of the simulations presented here can be directly compared to real measurements. Thus, simulating an instrument background with well known spectrum and composition is an ideal possibility to understand and verify the GEANT4 physics processes relevant for an in-orbit X-ray detector. After early successes in reproducing the local X-ray fluorescence of the electronics components behind the CCDs and with today's experience gained during the Simbol-X simulations, the simulation environment for the pn-camera has been recently extended to encompass almost the complete XMM-Newton satellite.

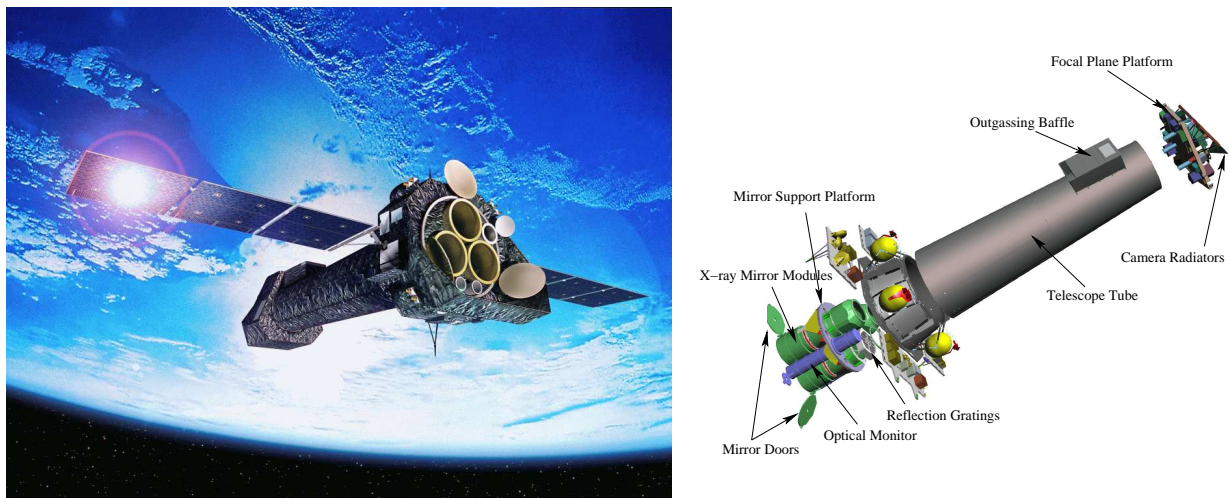


Figure 3.1: *The XMM-Newton Satellite. Left: artist's impression, courtesy of ESA; right: labeled exploded view of the XMM satellite, courtesy of Dornier Satellitensysteme GmbH*

3.1 An Introduction to the XMM-Newton Observatory

The European Space Agency's X-ray Multi-Mirror satellite was launched on December 10, 1999 in Kourou, French Guiana. Later, the name was changed to XMM-Newton in reference to Sir Isaac Newton's achievements in spectroscopy. The satellite had - at the time of launch

- a mass of 3800 kg, is 10 m long and 16 m wide with deployed solar arrays. It is situated in a highly elliptical orbit of 48 hours extending from 7.000 km to 114.000 km distance to earth, allowing long uninterrupted observations outside the earth's radiation belts. The satellite holds three X-ray telescopes, each of which contains 58 Wolter Type-I concentric mirrors. The combined collection area is 4300 cm² at 1.5 keV, decreasing down to 1800 cm² at 8 keV. The three European Photon Imaging Cameras (EPIC) (two MOS cameras and the pn-camera), located in the focal plane of the mirrors, are nominally sensitive over the energy range of 0.1 keV to 15 keV (Jansen et al., 2001). Other instruments on board are two reflection grating spectrometers (RGS), which are designed to operate below ~ 2 keV, and a 30 cm diameter optical/UV monitor (OM) telescope mounted parallel to the X-ray telescopes. Each of the X-ray telescopes has a field of view (FOV) of ~ 30 arcmin and a 6 arcsec (FWHM) spatial resolution.

XMM-Newton is especially designed to do time resolved imaging spectroscopy and thus to investigate in detail the spectra of faint cosmic X-ray sources. Due to its unprecedented sensitivity it is able to detect sources down to a few times 10^{-16} ergs/cm²/s (Jansen et al., 2001).

3.1.1 The MOS Cameras

Two of the X-ray telescopes are equipped with the X-ray gratings of the RGS instrument, which deflect part of the flux out of the EPIC beams. Therefore, only 44% of the original flux reaches the MOS cameras, located at the focal plane of these telescopes. Each MOS camera consists of seven specially designed 2.5×2.5 cm² CCDs with 600×600 pixels, arranged in a three-dimensional mosaic (as shown on the left in Fig. 3.2) to follow the focal plane curvature and to cover the focal plane diameter of 62 mm. They have a very good quantum efficiency in the energy range 0.2 to 10 keV. The standard readout cycle is 2.6 s, which is the length of the integration time. Faster (windowed) observation modes and a timing mode are also available (Turner et al., 2001).

3.1.2 The EPIC pn-Camera

The pn-camera is situated at the focus of the third X-ray telescope. It is a 6×6 cm² array of twelve individually operated pn-CCDs on a single monolithic wafer. The 3×1 cm² CCDs have a format of 200×64 pixels and are arranged in four quadrants (see Fig. 3.4). A pixel size of $150 \mu\text{m} \times 150 \mu\text{m}$ was chosen, sampling 4.1 arcsec of the field of view and resulting in a 6 arc second FWHM (15 arc second HPD) angular resolution. The sensitive material thickness amounts to $\sim 300 \mu\text{m}$ of silicon. X-rays hit the detector from the rear side, so the readout structures and charge transfer channels do not reduce the efficiency. In this way they are also automatically protected from low energy proton damage caused by protons coming from the field of view. Six different observation modes are implemented, allowing to reach a very fast time resolution spreading from 200 ms (Extended Full Frame Mode) to 5.7 ms (Small Window Mode) in the imaging modes, 0.03 ms and 0.007 ms in the Timing Mode, resp. in the Burst Mode. The energy resolution of both cameras, $E/\Delta E$, is ~ 20 -50 over the whole energy range (Strüder et al., 2001).



Figure 3.2: The focal planes of the MOS- (left) and pn-camera (right) on board of the XMM-Newton observatory. MOS: image courtesy of Leicester University, University of Birmingham, CEA Service d'Astrophysique Saclay and ESA; pn-camera: image courtesy of MPI-semiconductor laboratory, MPE, Astronomisches Institut Tübingen and ESA

3.2 The Geometric Model of XMM-Newton Used in the Simulations

In the course of this thesis, a geometric model of the EPIC pn-camera was developed with the intention to simulate the internal camera background in a Monte-Carlo simulation that makes use of the GEANT4 toolkit. Beginning with the CCDs themselves and the backplane PCB¹, which holds the electronic components necessary to operate and read out the CCDs, the model was later extended to include the whole camera with the proton shield and the collimator. At a later stage, additional minor support structures and a mirror module were added, which had been already implemented in the case of XMM in the GEANT4 'X-ray telescope' example illustrating the propagation of low energy (< 500 keV) protons through the X-ray mirrors via multiple scattering processes (Nartallo et al., 2001).

3.2.1 The XMM-Newton Spacecraft

A detailed mass model of one of the XMM telescope mirror modules has been implemented in GEANT4 in the above mentioned example application, in which only simple collecting volumes at the location of the focal plane represent the EPIC and RGS detectors. The X-ray baffle has been modelled as two 1 mm thick plates (59 mm apart) with a material composition of Ni and Fe with an element ratio of 1:2. The telescope mirrors have been modelled as 58 shells, each of which is made of four contiguous conic sections: two representing the parabolic shaped part of the mirror and two representing the hyperbolic part. The overall length of the mirrors is 600 mm, centered at a position 7.5 m from the focal plane. The surface of the mirrors is a 50 nm gold layer deposited on a nickel shell of ~ 1 mm thickness. The core of the telescope is filled by cylindrical nickel tubes. In this simulation geometry, the actual telescope tube is omitted, as it consists of a carbon fibre tube and was not considered relevant for the generation of background.

¹Printed Circuit Board

3.2.2 Implementation of the EPIC pn-Camera

As only the background of the EPIC pn-camera was analyzed in this study, no other instruments in the focal plane region were included in the simulations presented in this work. Figure 3.3 illustrates the details of the geometric model of the camera. X-ray photons focused by the mirrors will enter from below through the collimator and will reach the CCDs that are mounted to the lower side of the PCB, if the filter wheel is turned open. All simulations for the background - and also the measurements - reported in this work were performed with the filter wheel in its 'Closed' position, which is realized by a 1 mm thick aluminum plate. A thick aluminum proton shield protects the CCDs from damage that could be caused by high energy protons. Behind the PCB, a coldfinger made of copper connects the CCDs thermally to the radiator structure on top.

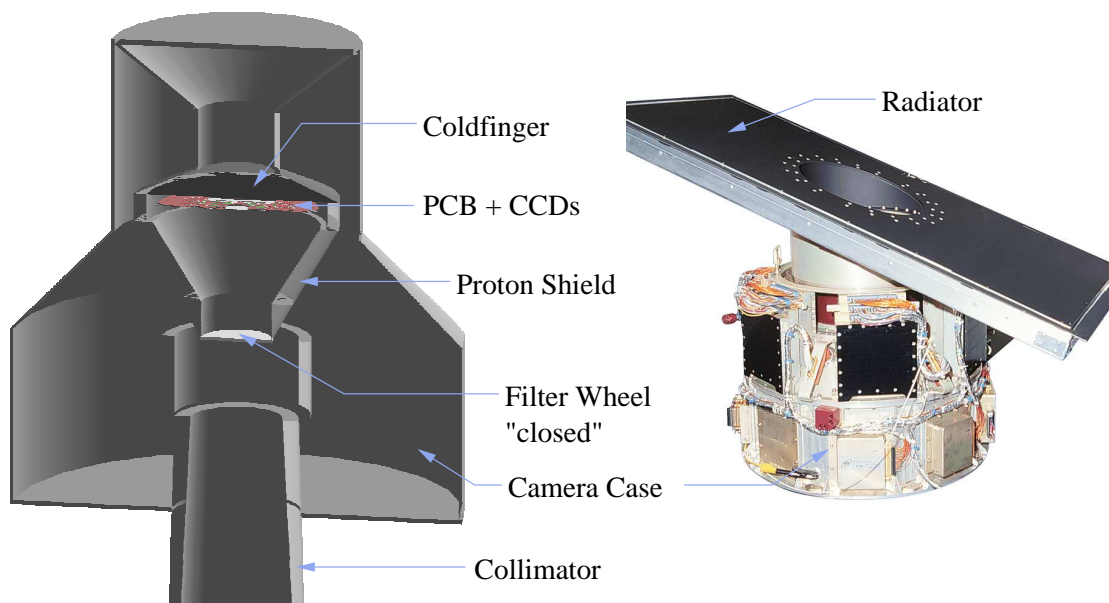


Figure 3.3: The EPIC pn-camera head - geometric model used in the simulations (left) and photograph of a spare model (right, courtesy of MPE, Garching).

3.2.3 The CCDs and the Backplane PCB

The CCDs are arranged as shown in Fig. 3.4. In the simulation, a single CCD is represented by a $300\ \mu\text{m}$ bulk layer of sensitive silicon, with a $30\ \text{nm}$ insensitive layer of SiO_2 on top. Directly behind the CCDs is the backplane PCB (Fig. 3.5), consisting of a $0.8\ \text{mm}$ molybdenum core enclosed between layers of $0.2\ \text{mm}$ copper on each side. The CAMEX and TIMEX chips for the control and readout of the CCD data as well as other smaller SMD¹ components are mounted on the opposite side of the PCB. However, a thin ($2\text{-}3\ \mu\text{m}$) Ni coating covered by the same thickness of gold is deposited at the respective positions on the CCD side to protect the devices against radiation (Pfeffermann et al., 1999). The layout of the PCB is implemented accurately,

¹Surface Mounted Device

following the original drawings obtained from E. Pfeffermann, MPE¹. A total of 432 of the board's electronics components are included in the simulations.

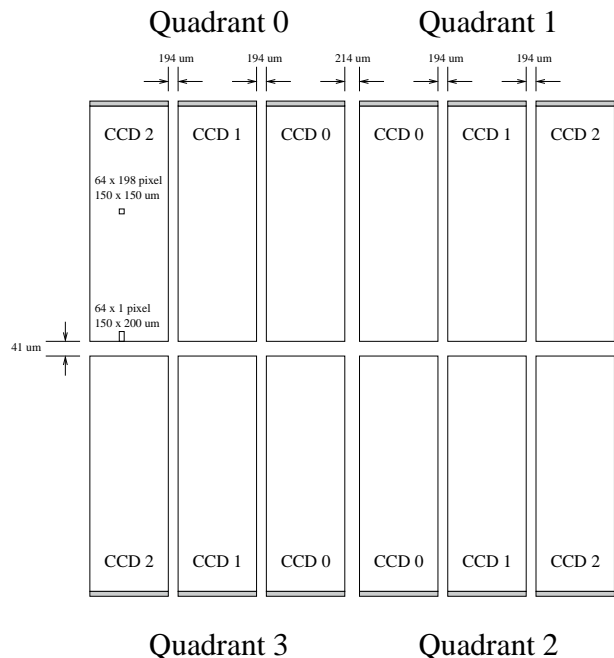


Figure 3.4: Layout of the CCDs in the focal plane of the pn-camera. The focal point is in CCD 0 in Quadrant 1 in order not to have the center of the field of view coincide with a gap between the CCDs. 97 % of the field of view are covered by the CCDs. About 6 cm^2 of the sensitive area are outside the field of view and are used for background studies. Note, that the size of the gaps between adjacent CCDs is enlarged in this figure.

3.3 The Measured Detector Background

The performance of the EPIC pn-camera is monitored regularly through observations of selected well-known astrophysical objects (among these are supernova remnants, neutron stars and AGN) and also during exposure times with the calibration wheel turned to the 'CalClosed' or 'Closed' position. In the 'CalClosed' position, the spectral response of the instrument can be checked with the help of lines from an ^{55}Fe calibration source that illuminates the CCDs. 'Closed' filter exposures are used to analyze the internal camera background as X-rays from sources or the Cosmic X-ray Background (CXB) as well as low energy particles passing through the telescope are stopped by the 1 mm thick aluminum 'Closed' filter (Freyberg et al., 2004).

3.3.1 Composition of the Background

The measured instrument background can be roughly characterized as consisting of two different components. The first one - detector and readout noise - is not further analyzed in this work as it is beyond the focus of the Monte-Carlo simulations. The second prominent component is caused by the interactions of high energy particles and radiation with the structures surrounding the detector and the detector itself. While the first contribution is reproducible also in a lab measurement on earth, the second, which is described in this chapter, strongly depends on the orbital environment present at the location of the satellite. Among the components of

¹Max-Planck-Institute for Extraterrestrial Physics

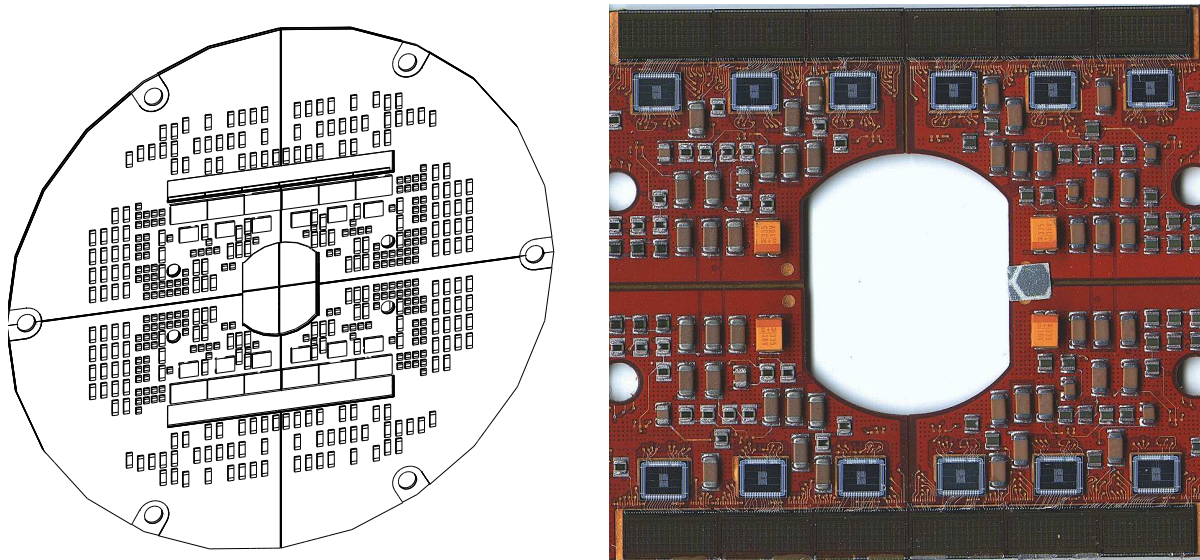


Figure 3.5: GEANT4 geometrical model (left) of the EPIC-pn focal plane printed circuit board (PCB) and a closeup photo of the area covered (on the backside) by the CCDs on a spare PCB (right). Among the components selected for the simulation are the CAMEX and TIMEX devices for each CCD as well as some smaller SMD components (resistors, capacitors).

this particle induced contribution to the background are so-called *soft proton flares* that show a strong and unpredictable variability and which are attributed to protons with energies below ~ 300 keV that are channeled onto the CCDs by the telescope mirrors. These have already been analyzed (Nartallo et al., 2001) and are not further studied within this thesis. A more detailed introduction to all of the relevant in-orbit background components is given in Chapter 5.

3.3.2 Data Selection and Reduction

For this comparison between measured and simulated background, a comprehensive dataset of 'Closed' filter observations, taken in the Full Frame (FF) and extended Full Frame (eFF) modes in the years since the launch of XMM-Newton, have been kindly provided by M. Freyberg, MPE. These observations have been carried out at different intervals and with different total exposure times between May 22nd, 2001 and January 1st, 2007 (see Fig. 3.6). The total observation time amounts to 301.55 ks in the FF mode and 304.03 ks in the eFF mode. The eFF mode is similar to the FF mode in so far that the whole CCD area is read out, though after a longer integration time. Thus, the two kinds of observations are evaluated together for this background study. From the event-lists in the compiled files, only single and double event-patterns have been selected in this analysis (FLAG=0, event patterns 0-4), as events that hit more than two pixel thereby collect more noise during readout and as a result broaden the spectral lines.

The raw data contains all kinds of 'Closed' observations performed in the above mentioned time-frame, including not only the calibration and background measurements, but also those cases, where the filter wheel was closed due to other causes, e.g. a high particle background,

as becomes clear from Figure 3.6. By selecting only the relevant 'good time' intervals, which show an average background below 10 counts per second, these extreme measurements can be excluded. After the application of this criterion, the remaining observations amount to 279.21 ks in the FF mode and 228.53 ks in the eFF mode, resulting in a total of ≈ 507.74 analyzed kiloseconds.

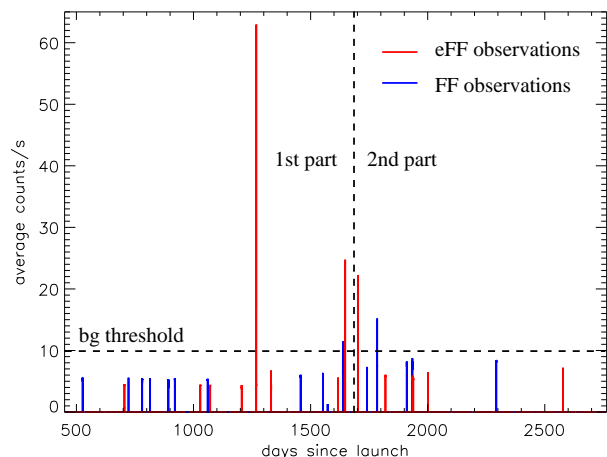


Figure 3.6: Time coverage of EPIC-pn FF and eFF observations with 'Closed' filter. The horizontal dashed line shows the threshold used for selecting the good time intervals.

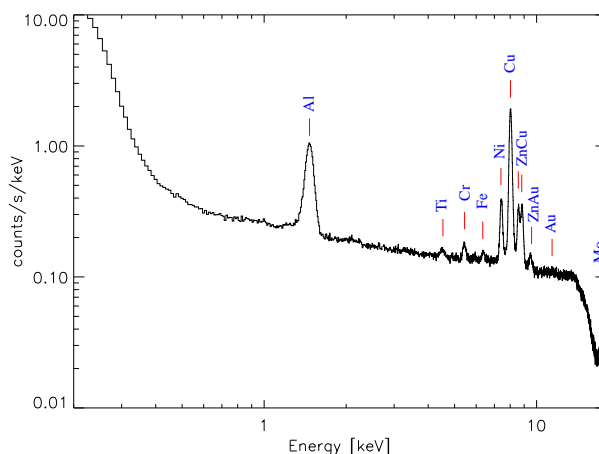


Figure 3.7: Measured EPIC-pn background spectrum in FF and eFF operation modes using the 'Closed' filter wheel position, single- and double-pixel events combined. The spectrum contains the events from all selected exposures.

A combined spectrum of the total observed time is shown in the range between 0.2 and 18 keV in Figure 3.7. The data are binned in 10 eV bins. Several prominent features can be observed in the spectrum like the fluorescence lines Al-K α , Ni-K α , Cu-K α , etc. As the spectrum also contains the recombined energies from double split events, the Mo-K α line at 17.4 keV can also be detected, which is suppressed in single events. This is due to the on-board MIP¹ rejection threshold at ~ 15 keV that removes events with higher energy values. Therefore, the spectrum above the threshold consists only of doubles with about evenly split energies. All the visible background lines are due to X-ray fluorescence produced by materials present in the spacecraft, most of them being constitutive elements of the pn-camera, close to the CCDs. The wide shape of the noise peak (below 400 eV) is due to the fact that when double events are included in the spectrum, their noise contributes twice to its spectral width.

When the dataset is separated into two parts at approximately the transition from the active half of the solar cycle into the solar minimum (see Figures 3.6 and 3.9), the measurements of the second part show on average a slightly higher background rate. The current solar cycle (#23) had two maxima in 2000 and 2002 and will reach its minimum in 2008. Although the total data are not equally distributed on the two timeframes (75.88 ks FF and 105.01 ks eFF observations in the second half), comparable spectra can still be produced. Figure 3.8 shows these spectra for

¹Minimum Ionizing Particles - see Chapter 7

the first and second part (solid and dotted line) as well as the difference between the two. It can be noted from the shape of these residuals and the ratio between the two spectra that the overall higher average background rate translates into a linear shift of the whole spectrum with a factor of about 1.5, that corresponds to the increase of the total count rate. This uniform effect on the complete energy range suggests that (as suspected) a higher cosmic ray proton flux, due to the decreasing solar activity, is responsible for the observed increase of the background. Other explanations, e.g. long-term activation of materials in the camera or instrumental effects, are not favored by this observation (see also the discussion in Section 3.6). Furthermore, this effect has been reproduced in the simulations (Section 3.5.2) by applying two different incoming cosmic-ray proton spectra for the two time intervals (see Fig. 3.10).

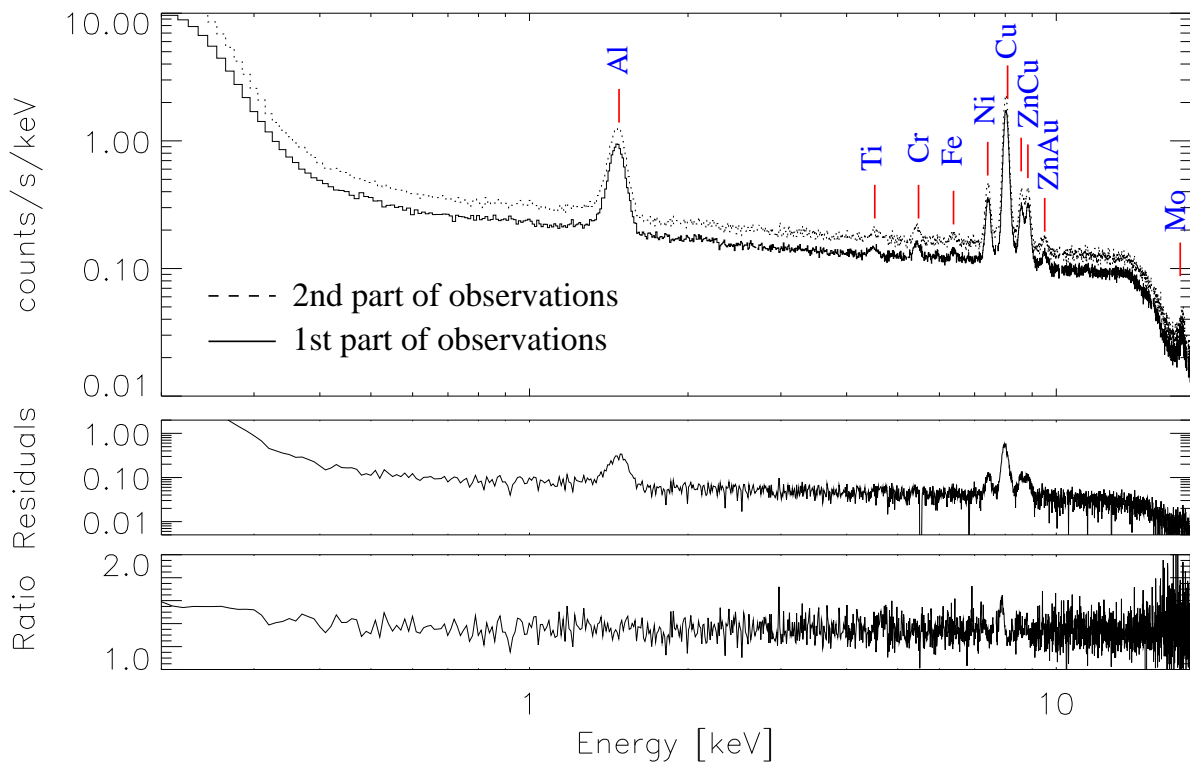


Figure 3.8: Measured EPIC-pn background during different times of the solar cycle. The residuals plot window shows the difference between the two spectra, the lowest plot window shows their ratio.

3.4 Details of the Simulations

Results from early simulations, based on an assumed flat spectral distribution of photons inside the camera, only included electromagnetic interactions (Tenzer et al., 2006). A much more detailed physics list, including also hadronic interactions (see Appendix A), which was derived from the new Simbol-X simulation environment, was used for the results presented here. Furthermore, a realistic space environment was considered as the origin of all interactions. As will be shown in the following sections, an agreement between simulations and the observed data

was obtained with this environment, confirming in turn the high quality of the predictions for Simbol-X and eRosita presented in later chapters.

3.4.1 *The Simulation Environment*

The environment outlined here is derived directly from the Simbol-X simulation environment. To avoid redundancy, more details of it are explained and motivated in Chapter 5.2. In this approach, protons, following an energy spectrum as shown in Figure 3.10, are generated on a sphere with a radius of in this case 50 m and are emitted into a small conical solid angle. The angle is calculated such, that a sphere containing mirrors and camera is exposed to an isotropic flux of particles. As explained in Chapter 5.2.4, this is necessary to obtain a normalization for the spectra or, put simpler, a conversion factor between the generated number of particles and the simulated timespan.

However, this approach leads to overall long simulation runtimes with only a few counts on a thoroughly shielded detector. In order to obtain a highly resolved background spectrum as desired in this case, a different solution was devised: In a first step, the simulation was performed as described above, but with an additional virtual detector volume in the shape of an ellipsoid, filling almost the complete interior of the camera and encompassing also the PCB and the CCDs. This virtual detector is 'ideal' in such a way that it registers all details like particle type, energy and direction for every single particle, as it first enters that volume. Thus, a lot of information about the internal radiation environment of the camera, given rise through the primary cosmic-ray protons, is obtained - much more than through the few valid counts on the CCDs.

This internal environment serves now as the input to the second simulation step, where it is artificially reproduced and is taken as the origin of further interactions. Some changes are applied, though: Only neutrons, protons, electrons, positrons and photons are generated in this second step, other particles are neglected. Energy and direction distributions are drawn from smoothly interpolated histograms that were created in the first step in order to match the original environment. In this way it is possible to enlarge the samples of generated particles by thousands. This technique allows, finally, to reach a sufficiently high number of counts to generate a spectrum that can be compared to measurements.

3.4.2 *Incoming Particle Spectrum and Flux*

In this study, only cosmic-ray protons were considered as an input for the simulations, as they have been clearly identified to be responsible for the largest fraction of the internal background on altitudes above 60.000 km, a region outside of the radiation belts where all scientific measurements take place. Figure 3.10 shows the respective spectrum and fluxes for different times of the solar cycle. These data have been calculated using the CREME86 model of the OMERE software that has also been used to predict the space environment which Simbol-X will encounter in its scheduled orbit.

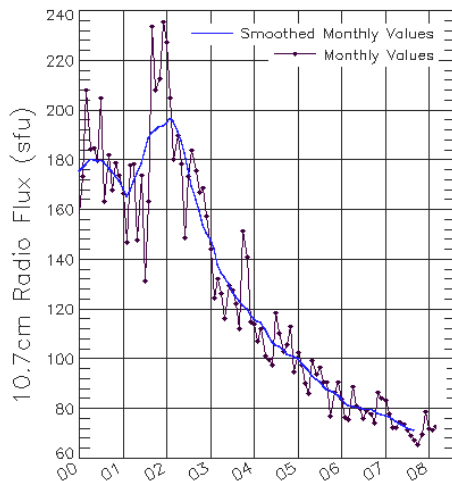


Figure 3.9: Solar flux progression (in the 10.7 cm radio band) during the current solar cycle (NOAA/SWPC, Boulder, Colorado).

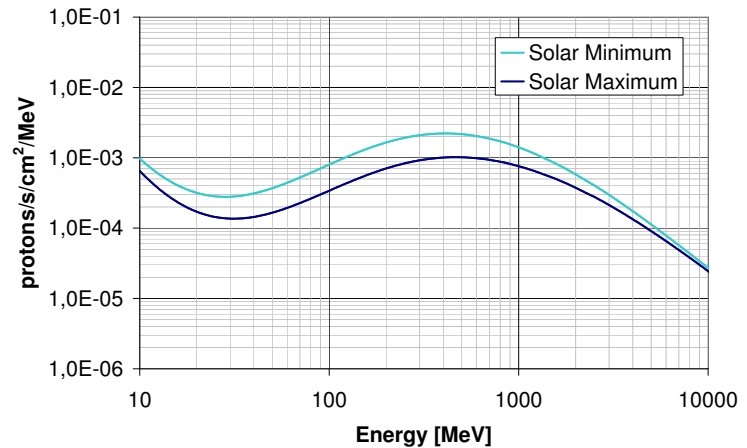


Figure 3.10: Cosmic-ray proton spectra and fluxes used to simulate the EPIC-pn background during different times of the solar cycle. The spectra are averaged over the XMM orbit and have been calculated with the CREME86 model of the OMERE software for the current solar cycle.

3.4.3 Data Generation and Storage

From each interaction of a particle or photon taking place in one of the twelve CCD volumes, the time and the deposited energy are registered. Furthermore, the coordinates of the interactions are recorded to identify the respective pixel in which the interaction took place. Since the generation and dispersion of a charge cloud is not included in these simulations, only single-pixel events are generated by the simulation. The deposited energy of a detected photon is therefore registered exactly in a simulation, i.e. the spectrum shows no broadening of lines, as is observed with real detectors due to the limited energy resolution. To account for this effect, the final energy for each event is determined by drawing from a random number generator which produces a Gaussian distribution, centered around the original energy and having a width according to the detector's approximate resolution at that energy. The approximation is derived from a simple linear interpolation between $E/\Delta E = 20$ at 0.2 keV and $E/\Delta E = 50$ at 18 keV. Actual spectral resolution measurements from the calibration of the pn-camera can be found in Briel et al. (1998).

The four parameters (time, energy, x- and y-pixel coordinates) are stored in an FITS¹ event-list utilizing a format matching those that the pn-camera itself generates. In this way, the standard XMMSAS² or commonly used IDL³ routines can be applied to evaluate both the measurements and the simulations. For tasks like the generation of spectra, images and rate curves this

¹Flexible Image Transport System - a common file format for astronomical data

²XMM-Newton Science Analysis Software - an extensive suite of software tools developed to process the data collected by the XMM-Newton Observatory

³The Interactive Data Language is a programming language that is popular among scientists for analyzing large data arrays.

is very convenient, as no new software has to be designed in order to evaluate the simulations and the comparison to the measurements is facilitated.

3.5 Results of the Simulations and Comparison to Measured Data

Three central topics have been selected for the pn-camera simulations. After the geometry was composed, the first step was to check the **quantum efficiency** of the simulated detector for X-ray photons in a range of 0.1 to 18 keV against a real measurement. With the functioning detector, the main background simulations could then be performed, each resulting in an event list from which **spectra** could be extracted. Finally, by selecting only thin energy slices around certain fluorescence lines from the event lists, images could be created, that display the **spatial distribution** of those events.

3.5.1 Quantum Efficiency of the pn-CCDs

For the simulation of the quantum efficiency (QE) 10^7 photons with a linear energy distribution between 0.1 keV and 18 keV were created. These were shot one after another at the backside of a single CCD, in a beam perpendicular to the surface of the CCDs. As stated earlier in the description of the simulation geometry, the model of the CCDs used in the simulations consists of 300 μm of sensitive silicon with 30 nm SiO_2 at the entrance window of the photons. Whenever one of the incoming photons underwent an interaction inside the silicon via the photoelectric effect and thereby deposited all of its energy, the *event* (creation of one primary particle, see Chapter 2.3) was marked. The simulated quantum efficiency shown in blue in Fig. 3.11 is then the ratio of marked vs. unmarked primary photons created with a certain energy.

The detection efficiency at high energies is determined by the thickness of sensitive silicon, while the composition and thickness of the radiation entrance window and optional filters cause the low energy response. Figure 3.11 also shows the results (circle and diamond shaped data-points) of the absolute quantum efficiency calibration at PTB (BESSY synchrotron in Berlin) and LURE (synchrotron in Orsay, Paris). These data were taken for comparison from Strüder et al. (2001). The measurement was made under conditions comparable to space operation. The solid line is a fit to the measured data with a depletion thickness of 298 μm (Hartmann et al., 1999).

As the absorption length of X-rays in silicon at 150 eV is only ~ 30 nm, the thin oxide layer already absorbs nearly one half of the incident photons at low energies. The drop of about 5% of QE at 528 eV is due to the oxygen absorption edge that provides additional absorption in the oxide layer. The other prominent feature in the measured data is the typical X-ray absorption fine structure (XAFS) behaviour around the silicon K edge at 1.838 keV, enlarged in the inset. The simulation of this behaviour was not attempted as it lies beyond the scope of the current simulation environment. Otherwise, the simulated data corresponds within statistics exactly to calculations of quantum efficiencies that were performed with the different material parameters (see e.g. in Chapter 5.3.2).

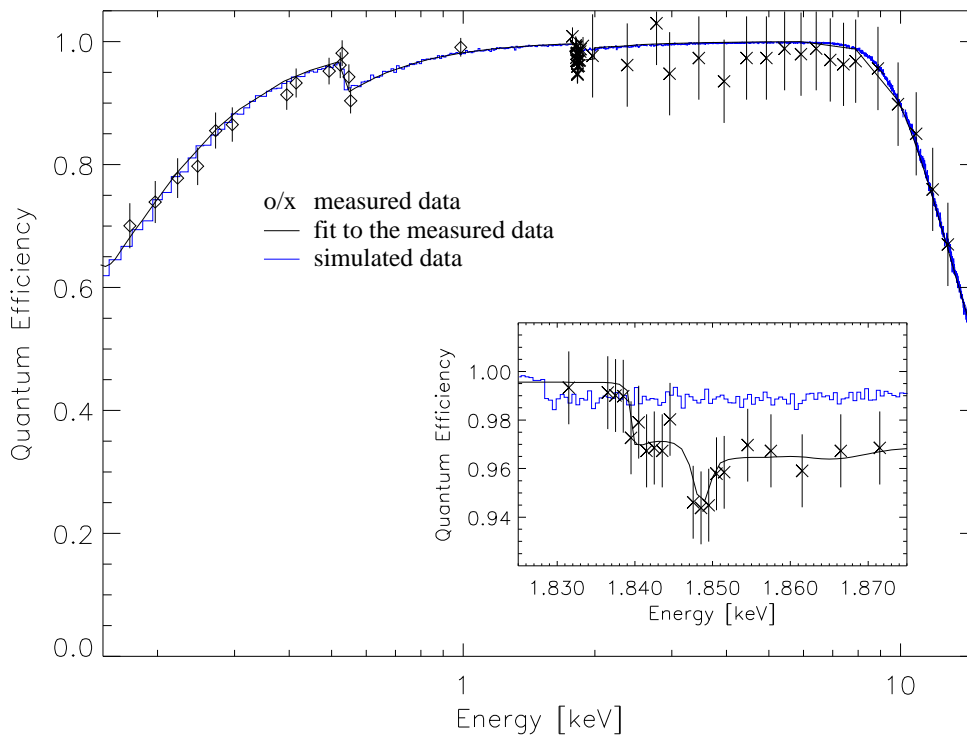


Figure 3.11: *Simulated (blue) vs. measured quantum efficiency of the pn-camera. The inset shows the enlarged region around the silicon K edge.*

3.5.2 Simulated vs. Measured Background Spectra

Each interaction with one of the CCDs in the second part of the background simulations (see Section 3.4.1 above) adds one row of data to an event list containing time, x- and y-coordinates and deposited energy. The spatial dispersion of the charge cloud produced inside of the CCD material was not simulated, therefore, no split events are produced. The spectra, which are created from these event lists by arranging the energy column in a histogram with 10 eV binsize, thus have to be put up against spectra with recombined energies when they are compared to measured data. Properties of the CCDs that relate to the readout process (e.g. charge transfer efficiency) or the readout electronics are not considered in the simulation. Only the energy resolution of the detector is taken into account as described above.

The results of two simulations with different proton input spectra (see Fig. 3.10) are presented in Figure 3.12. The upper two plot windows display the simulated spectrum for the solar maximum proton flux compared to the measured spectrum for the first part of the observations. The lower plots show the spectra for the solar minimum flux and the second part of observations. In the residuals plots, the differences between measured and simulated spectra are given. The lowest plot window shows the respective ratio between the simulated and the measured spectrum. For the first part of the observation, this ratio is about 1.5, in the second part it is 1.3.

The simulated spectra match the general shape of the background continuum quite well. Also, the background level is reproduced accurately, although the difference between solar maximum and solar minimum is slightly larger than in the measured data. A possible explanation for this effect is given in the following discussion. As only those materials have been included into the geometry that were deemed responsible for the most prominent fluorescence lines, the simulation does not generate all of the lines observed in the measurements (e.g. the lines of Ti, Cr and Fe are missing). This lack of material in the geometry could also contribute to the explanation of the fact that the simulated fluorescence lines are slightly diverging in their absolute and relative intensity from the measured data. The differing intensity of the lines could also be attributed to currently discussed details in the simulated physics and will be subject of a follow-up study.

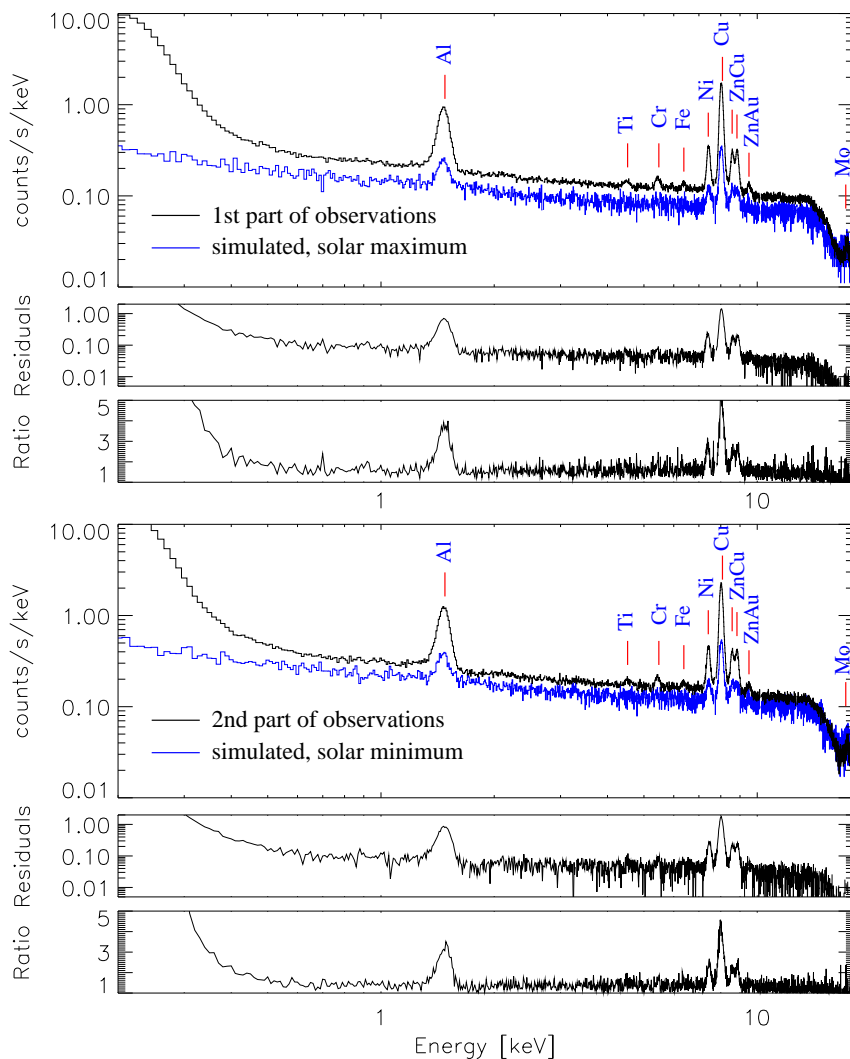


Figure 3.12: Comparison between simulated and measured EPIC-pn background spectra during two different times of the solar cycle (top: solar maximum simulation and first part of observations, bottom: solar minimum simulation and second part of observations). The residuals plot windows show the respective differences between measurement and simulation.

As no noise is simulated, there is consequently no peak below 400 eV in the simulated data. In summary, the spectral shape and the flux level are reproduced with an accuracy high enough to allow detailed predictions about the background of future X-ray observatories.

3.5.3 Simulated vs. Measured Fluorescence Images

When the spatial event distribution on the CCDs is studied in narrow energy bands of a few hundred eV width, inhomogeneities can be noticed around some of the fluorescence lines. While the Al-K α line at ~ 1.5 keV appears to have an isotropic distribution, the lines at higher energies show strong correspondence with the electronics board mounted below the CCD wafer. Careful selection and subtraction of the background is therefore required in source observations if one is interested in spectral features close to these inhomogeneous fluorescence lines (Freyberg et al., 2004; Pfeffermann et al., 2004b).

As the printed-circuit board that carries the electronics consists of two copper layers with a molybdenum core embedded in between, the fluorescence events of Cu-K α on the CCDs are detected with a distribution following the shape of the board. At the edges of the four individual quadrant plates the characteristic Mo-K α line emission can escape. Nickel is used to shield the electronic devices, so emission is correlated with the CAMEX and the TIMEX chips situated at the top and bottom of the images and also with other electronic components. At Ni-K α emission enhancements, deficits in the Cu-K α emission due to absorption can be noticed.

The measured images on the right side of Figure 3.13 are taken from Freyberg et al. (2004) and have a different normalization and colorscale than the simulated ones on the left. The latter have been composed of the events generated by the solar minimum simulations. The spaces in between the CCDs are artificially added to the simulated images when the position of an event from the CCD coordinates is reconstructed. There seems to be a small problem with the scale of the PCB compared to the CCDs, as can be noticed from the different positions and sizes of the holes in the PCB. However, this does not affect the conclusion that the images of fluorescence line emission distribution generated with the simulation environment are in good agreement with the measured images.

3.6 Discussion of the Results

Using an adaptation of the Simbol-X simulation environment for XMM-Newton, it was possible to reproduce the measured quantum efficiency and background spectrum of the pn-camera with a high degree of accuracy. Also the effect of the spatial inhomogeneity of the fluorescence emission, due to the distribution of the electronic components could be nicely simulated.

Once the measurements with the anomalously high background are excluded from the analysis (*Fig. 3.6*), it becomes evident that the averaged background rate of all observations in the second half of the analyzed data is higher than that of those in the first half. This rise in background is most likely due to the increasing particle flux at the location of the spacecraft, following the progression of the solar cycle. The more active solar wind and stronger magnetic

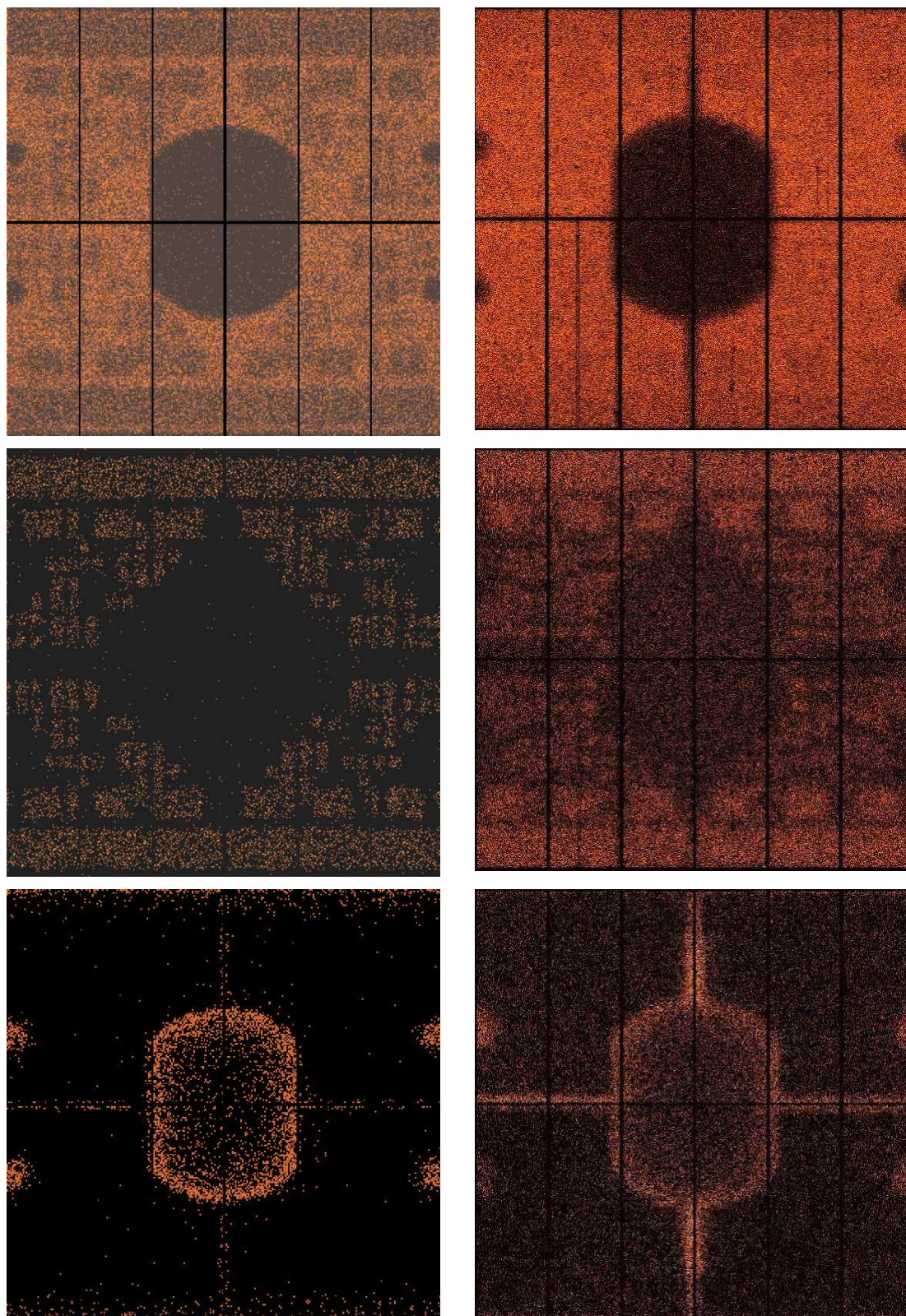


Figure 3.13: Comparison between images composed of simulated (left) and measured (right) events around three of the fluorescence lines (top: $\text{Cu-K}\alpha$ 7.8 - 8.2 keV, middle: $\text{Ni-K}\alpha$ 7.3 - 7.6 keV and bottom: $\text{Mo-K}\alpha$ 17.1 - 17.7 keV). Simulated and measured (from Freyberg et al., 2004) images do not have the same absolute normalization (different number of events and colorscale).

fields at solar maximum usually reduce the number of cosmic rays striking the observatory in its orbit. As the two measured spectra are both averaged over a timeframe on the declining half of the solar cycle, the simulations, which refer to the solar maximum and minimum, under- resp. overestimate the flux in the simulated spectra. This effect can be noticed in the fact that the difference between simulation and measurement in the second part is much smaller than in the first, although the simulations tend to produce a lower background in both cases.

The rising flux could also be attributed to the activation of materials and following radioactive decay. However, the consequences should then be observable in the shape of the spectrum and, furthermore, activation would have led to a continuous rise of the background from the very beginning of observations, reaching finally a stable equilibrium. The final confirmation can be expected in a few years when observations on the rising branch of the solar activity cycle are available.

The results on the simulated fluorescence images are of key interest for the design of future focal planes. The observation of these images in the pn-camera already directed the constructors' awareness to this problem. Simulations of a new geometry design now can help to identify the sources of fluorescence in advance and to compare different solutions for shielding or the emission from different materials. As also the overall background level and shape is nicely reproduced by the simulations, they can be an excellent tool to compare various shielding concepts from the cosmic-ray protons and camera geometries to each other in their impact on the detector background.

The results presented above display only a fraction of the possibilities offered by Monte-Carlo simulation of physics processes for in-orbit background studies. Further simulations on a range of different topics are also described in the following chapters. One of the main problems of the simulations are the long computation times (ranging from a few hours to four weeks) it takes to test even the smallest change in a geometry. Also, minute changes in the simulation physics or the evaluation code produce large differences in the outcome and the current environment reached its present quality much faster through frequent comparison of the results to the measured background and also to results of other members of the Simbol-X simulation group.

The results also nicely demonstrate the possibilities and the approximate level of accuracy that can be achieved in simulating an instrument background with this simulation environment. In the following chapters it will be used to predict and optimize the background levels and also the performance of future X-ray observatories.

CHAPTER 4

The Simbol-X Mission

Up to today, Wolter-type mirror optics have only been used to focus X-ray photons with energies below ~ 15 keV. For energies above that threshold, the required focal length, which is proportional to the energy of the focused photons due to the grazing reflection angle used in this technique, would be too large to be incorporated within a single stable spacecraft that is launched by a rocket or brought into orbit with the space shuttle. By having the mirrors and the detectors on two separate but jointly launched spacecraft in a formation flying configuration, the French-Italian-German Simbol-X mission (Ferrando et al., 2008) uses for the first time focusing mirror shells with ~ 20 m focal length and multilayer coating to focus X-rays up to 80 keV. With this novel approach, it will surpass the angular resolution and sensitivity previously achieved in this range with non-focusing instruments by two orders of magnitude.

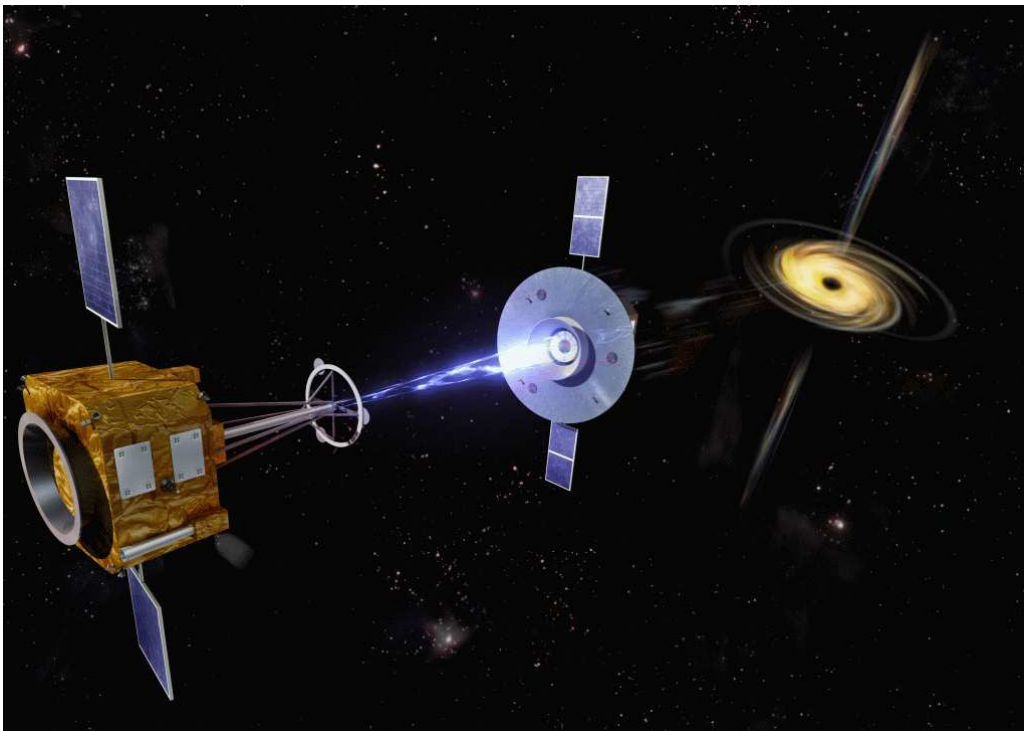


Figure 4.1: Artist's impression of the two Simbol-X spacecraft, courtesy of CNES / Oliver Sattler (March 2006).

4.1 Mission Concept and Characteristics

The mission first went through an assessment study performed by CNES¹ and completed a very successful phase A in December 2007. It currently stands at the beginning of phase B, with the launch foreseen in 2014. The two spacecraft will then be launched into a four day highly elliptical orbit (20,000 km to 180,000 km) with a starting inclination of 5° and an effective observation time of 290 ks (83% of an orbit) above 73.000 km per orbit (see Fig. 4.2). In the nominal mission lifetime of three years (with provision for a possible two-year extension), approximately 1000 pointed observations are projected with the main limiting factor being the fuel consumption for the complex realignments of the two satellites (the mirror spacecraft is simply rotated, while the detector spacecraft also has to be relocated) to a new observation pointing. The science objectives of the mission and the instrumentation are presented in the following sections below.

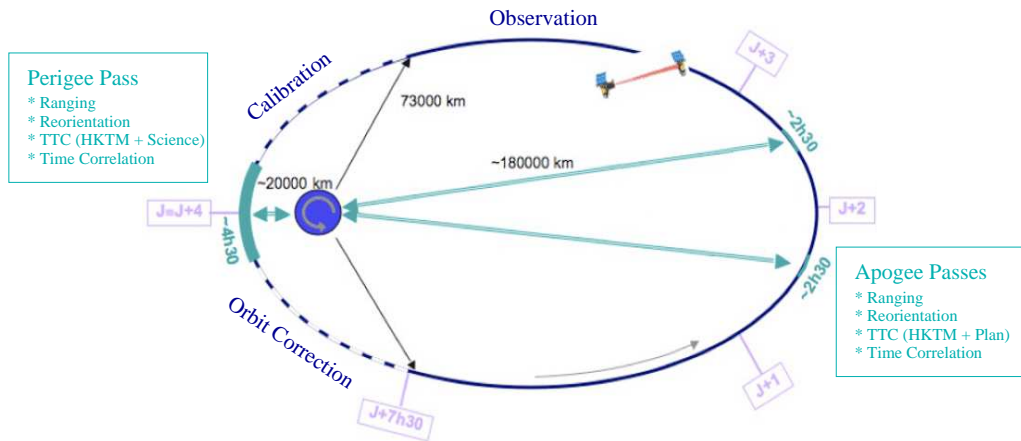


Figure 4.2: Task distribution along the projected orbit of Simbol-X.

4.1.1 Scientific Objectives

Due to the limiting maximum focal length of a single spacecraft, X-ray and gamma-ray imaging instruments working above 15 keV have until now only applied coded-mask imaging techniques, which have intrinsically a much lower signal-to-noise ratio than focusing instruments and also a much lower (~ 1 arcmin) angular resolution. Unfortunately, this drop of resolution and sensitivity, with respect to focusing telescopes, happens in a spectral region above which the identification of a non-thermal spectral component can be unambiguously distinguished from thermal emission. This limits the interpretation of today's X-ray measurements and particularly those related to the acceleration of particles (Ferrando et al., 2005). With the Simbol-X mission it will now be possible to bridge this gap of sensitivity by offering an instrument that extends the performance of current X-ray telescopes into the hard X-ray domain up to 80 keV and which will allow to fully cover the transition from non-thermal to thermal emission down to 0.5 keV.

¹Centre National d'Etudes Spatiales - French Space Agency

Two wide fields that are of outstanding importance to high-energy astrophysics and cosmology are at the core of the Simbol-X scientific program Ferrando et al. (2005): black hole physics and census and mechanisms for particle acceleration. Put more precisely, the following topics will be addressed by Simbol-X observations:

- **dynamics of matter around compact objects:**

The X-ray emitting processes that occur close to astronomical objects harbouring extreme physical conditions (regarding magnetic fields, gravity and pressure) provide a unique opportunity to explore physics beyond the conditions possible to create in the environment of a laboratory on earth. By disentangling the origins of the different spectral components (e.g. synchrotron emission in a jet, inverse Compton scattering from a hot corona or emission from a very dynamic accretion disk), the geometry of accreting Black Hole systems can be identified. The observation schedule will encompass spectral measurements of galactic Black Holes and of those in nearby galaxies in all states of accretion, as well as studies of Ultra Luminous X-ray Sources and detailed measurements of a very large sample of Active Galactic Nuclei (AGN), even highly obscured ones, which play a role in the composition of the Cosmic X-ray Background. It will also be possible to measure the spin of Black Holes via the shape of the relativistic Fe line. Last but not least, Simbol-X will measure the high energy emission of the supermassive Black Hole at the center of our galaxy (SgrA*) and therefore contribute to our understanding of the interactions taking place in galactic cores.

- **highly absorbed AGN:**

In the practically new field of Compton Thick AGN, Simbol-X is expected to extend the range for detailed investigation up to cosmological distances ($z \sim 0.5 - 1.5$), since very few Compton Thick AGN (mostly in the local universe) have been found and studied so far and many are believed to have remained yet undetected even in the deepest XMM-Newton and Chandra surveys (Della Ceca et al., 2007). Simbol-X will discover the faint population of hard X-ray sources just as the Einstein and UHURU satellites did in the soft energy band. It is the first observatory that is able to disclose the high energy part of the spectrum of X-ray binaries and allows a thorough study of the emission mechanisms for persistent and transient sources through monitoring their variability (Campana, 2007).

- **the Cosmic X-ray Background (CXB):**

Deep Simbol-X surveys will be able to resolve about half of the CXB (see Fig. 4.3) in the 10-40 keV energy range where, at present, less than a few percent of it is resolved in that band. While deep surveys with ROSAT showed that luminous unobscured quasars at high redshift ($z \sim 1.5 - 2$) were responsible for most of the soft CXB around 1 keV (Lehmann et al., 2001), it was demonstrated with Chandra and XMM-Newton observations, that the bulk of the CXB at least up to 5 - 6 keV is originating in relatively low luminosity sources, most of them obscured, at $z \sim 1$ (Brandt and Hasinger, 2005). While Simbol-X is expected to uncover the so far elusive population of Compton Thick AGN deemed responsible for the emission, it may well be possible that the content of the X-ray sky above 10 keV differs from the predictions (Comastri et al., 2007). Until now, almost nothing is known of

the CXB's origin above this energy and in particular around its spectral peak between 30 keV and 50 keV. With its extraordinary sensitivity in this energy band, Simbol-X will have the necessary instruments to detect the assumed Compton thick sources and resolve another good fraction of the CXB, thus providing further understanding of this fundamental phenomenon. The identification of the origin of the diffuse Cosmic X-ray Background at higher energies may therefore also place further constraints on the formation and evolution of structures in the universe.

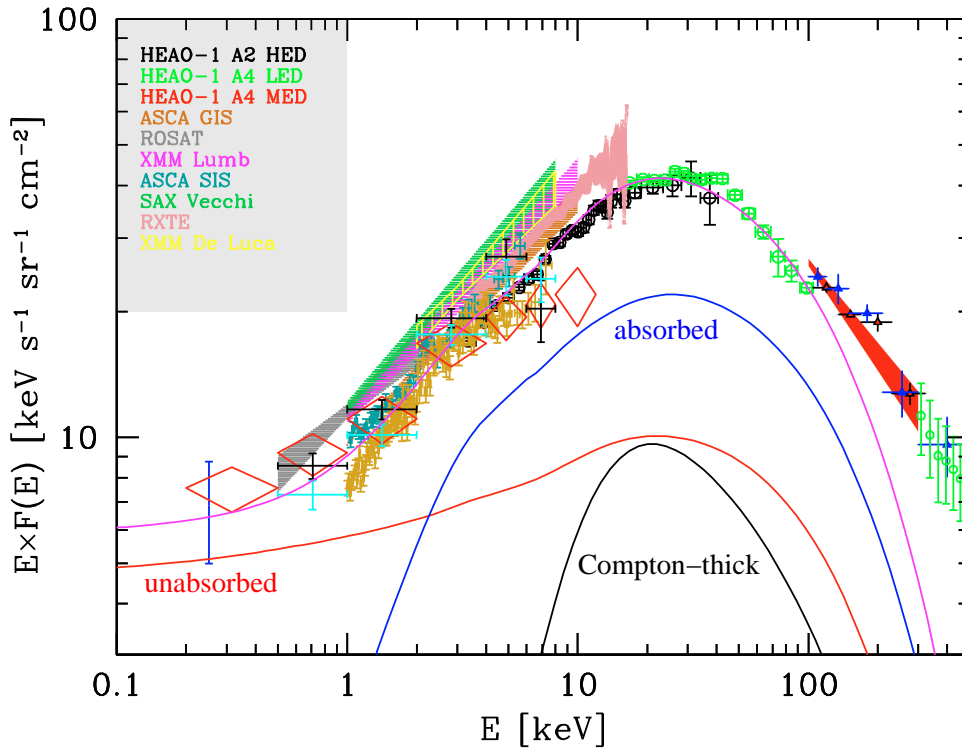


Figure 4.3: The Cosmic X-ray Background spectrum: measurements and predicted contribution from different AGN populations. The measurements are explained on the top left, the solid lines refer to the modelled contributions of unobscured AGN (red), obscured Compton-thin AGN (blue) and Compton-thick AGN (black). The total AGN plus galaxy cluster contribution is shown in the magenta curve (Gilli et al., 2007).

- **acceleration of particles:**

In order to contribute to the knowledge of acceleration mechanisms and to provide clues as to the origin of the highest energy cosmic rays, Simbol-X will observe known sites of particle acceleration like supernova remnants (SNRs) and extended X-ray jets of AGN as observed in Centaurus A and Pictor A. Being able to measure the synchrotron spectrum into the hard X-rays will allow (together with radio and TeV gamma-ray data from the H.E.S.S. observatory) to confine the maximum energy of accelerated electrons and will give hints on the responsible limiting mechanisms.

- **Nucleosynthesis in young SNRs:**

Observation of hard X-ray and gamma-ray lines, like the 67.9 keV line from the $^{44}\text{Ti} \Rightarrow ^{44}\text{Sc} \Rightarrow ^{44}\text{Ca}$ decay chain in young SNRs, is essential for our understanding of explosive nucleosynthesis since these lines trace directly the mass of the synthesized elements without further assumptions about the physical conditions. The long ^{44}Ti lifetime of 87.5 years allows to detect the lines from the above chain even after the SN envelope became transparent. With its high sensitivity, Simbol-X will allow to locate the emission regions and to measure their velocity, which will provide valuable information on the production yields and the dynamics of the explosions.

Table 4.1 shows an overview of the top-level scientific requirements resulting of each of the above mentioned science topics.

Table 4.1: *The Simbol-X top-level scientific requirements. Synopsis of the requirements for each science topic taken from Ferrando (2005). An X denotes that the best value possible is desirable, a – means that this parameter is not essential.*

Topic	Energy Band (keV)	Spectral Resolution	Angular Resolution	Time Resolution	Field of View	Sensitivity (cgs)
SgrA*	1.5 to >50	X	< 30''	–	–	X
GC diffuse	1.5 to >50	X	< 30''	–	X	X
X-ray Bin.	0.5 to 80	X	< 30''	< 1 ms	–	$\sim 10^{-14}$
AGN	1.5 to >60	E/ Δ E=40-50	< 30''	–	–	X
CXB	1.5 to 50	–	< 20''	–	X	< 10^{-14}
SNRs	1.5 to 50	X	< 30''	–	X	X
^{44}Ti	– to 80	1 keV @ 70 keV	< 30''	–	X	X
Total	0.5 to 80	E/ Δ E=40-50	< 20''	< 50 μ s	> 12'	< 10^{-14}

4.1.2 Optics

The Simbol-X mirror module profits from a rich heritage of manufacturing knowledge from the XMM-Newton nested Wolter-I mirrors. The thin nickel shells will again be obtained from super polished mandrels by an electroforming replication method. The key difference is that a platinum/carbon multilayer coating will be applied to fulfill the requirements on the large field of view and the high sensitivity as the reflection performance can be significantly improved this way at higher energies with respect to standard coating. Multilayer mirrors are based on stacks with alternating layers of high-Z and low-Z materials. This technique provides more effective reflection at angles up to three times those of mono-layer surfaces and makes telescopes effective up to 80 keV (to the K absorption edge of the high-Z reflecting material). A further gain in reflectivity, restricted to the low energy range up to 4 keV, can be achieved by using the low-Z material as the first external layer, with the role of reducing the photoelectric absorption effect when the mirror acts in the total reflection regime (Pareschi et al., 2004, 2005). A total of 100

shells will be formed with diameters from 26 to 65 cm. The desired low weight will be reached via a reduced shell thickness with respect to XMM-Newton. The necessary stability is provided by two spider wheels on each side. The optics module will have both sides covered with thermal blankets. Additionally, a proton diverter, consisting of permanent magnets, will be installed.

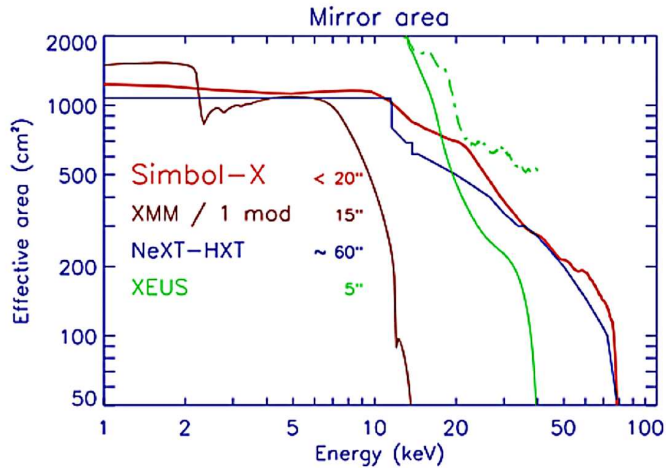


Table 4.2: Properties of the Simbol-X mirror module

Parameter	Value
Focal length	20 m
Angular resolution	20''
Field of view	$\geq 12'$
Mirror type	Wolter-I
Number of shells	100
Coating	multilayer Pt/C
Shell diameters	26 to 65 cm
Shell thickness	0.2 to 0.6 mm

Figure 4.4: Effective area of the Simbol-X mirror module (G. Pareschi, INAF)

4.1.3 Low Energy Detector

The Low Energy Detector (LED) of Simbol-X is a matrix of 128×128 pixels, which is logically divided into four equal quadrants that are integrated on a single monolithic silicon wafer (Fig. 4.6, bottom). All four quadrants connect to their own front-end electronics (CAMEX - Charge Amplifier and MULTIPLEXer) and are read out simultaneously at a frame time of $128 \mu\text{s}$ (see note below).

The LED, which is developed by the Semiconductor Laboratory of the MPI¹ (HLL), is a silicon drift detector with DEPFET (DEpleted P-channel Field Effect Transistor) readout. It consists of a large ($8 \text{ cm} \times 8 \text{ cm} \times 450 \mu\text{m}$) completely depleted silicon bulk with a p-channel MOSFET located on the surface of the front side at the center of each pixel to store, measure and clear the electrons generated by incoming radiation (Fig. 4.5). The latter are surrounded by drift rings of increasing voltage that generate a potential within the pixel to drive the charges from a larger area towards the readout structure (Fig. 4.6, top). This way, a large sensitive pixel area with a small readout capacitance can be provided (Zhang et al., 2006).

Due to the flexible concept of the drift rings, the pixel size can - in the design stage - be matched to the science requirements of the project, from $1 \times 1 \text{ cm}^2$ down to $50 \times 50 \mu\text{m}^2$,

¹Max-Planck-Institute

without affecting the energy resolution. For the Simbol-X mission these so-called Macro Pixels have a size of $625 \mu\text{m} \times 625 \mu\text{m}$.

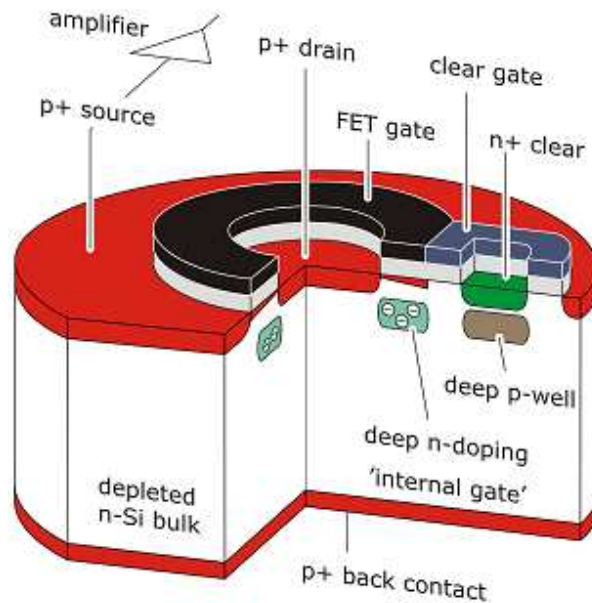


Figure 4.5: Model of a DEPFET pixel, showing the circular deep-n implant of the internal gate as well as the surface structures of the MOSFET. On the right side, the structures for the clear operation with the clear gate and clear contact are shown above a deep p-well that prevents leakage of the stored electrons (image: MPI Semiconductor Laboratory).

Up to 10^5 electrons can be collected and stored below the 'internal gate' of the readout MOSFET (see Fig. 4.5), where their signal can be measured in a non-destructive way (signal sampling) as a step in voltage when turning on the external gate. After the measurement, the charge is removed by applying a positive voltage to the clear contact. The voltage at the source node can then be measured again with an empty internal gate (baseline sampling) and the difference corresponds to the number of electrons collected during the integration time.

The detector is back-side illuminated and features an entrance window coated with a thin aluminum layer, which will suppress optical light (see Chapter 5 for details). Via the support structure, the detector wafer has an interface to a heat pipe that is connected to a radiator. Together with active heaters, this allows to stabilize the temperature of the wafer at $\sim -40^\circ\text{C}$, which is necessary to reduce the thermal noise and to ultimately achieve an energy resolution of $< 150 \text{ eV}$ (FWHM) at 5.9 keV .

With an upgrade of the readout electronics, which is currently under study, the frame time will be diminished to $128 \mu\text{s}$, either by a new generation of ASICs or by implementing twice the number of readout chips and thus reading two rows at the same time. More information on the LED can be found in Lechner et al. (2008).

Table 4.3: Parameters of the Simbol-X low energy detector (LED)

Parameter	Value
Format	8 x 8 cm ²
Pixel format	128 x 128 pixels
Layout	monolithic, 4 independent quadrants of 64 x 64 pixels
Pixel size	625 x 625 μm ²
Detector material	Silicon
Material thickness	450 μm
Energy resolution	150 eV at 6 keV
Electronic noise	low (≤ 10 el. ENC)
Readout time	≤ 256 (128) μs per frame
Window mode	± 16 pixels
Op. temperature	-40°C

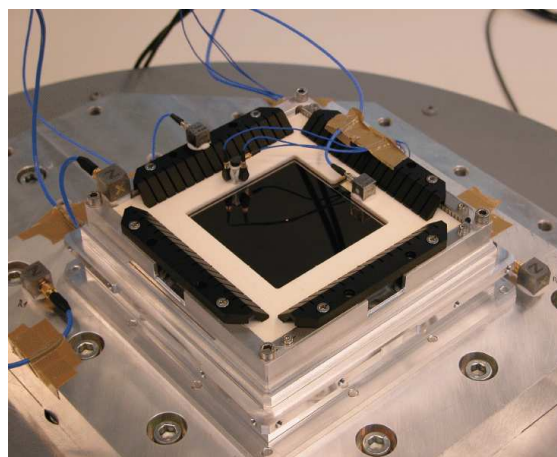
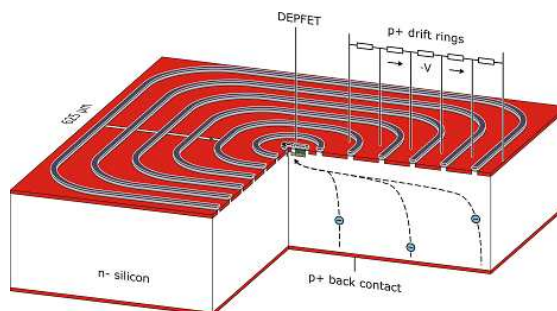


Figure 4.6: The Simbol-X Low Energy Detector. Top: illustration of a single pixel with drift rings and DEP-FET readout, bottom: prototype wafer containing 128 × 128 pixels. (images: MPI Semiconductor Laboratory)

4.1.4 High Energy Detector

The performance of the CdTe polycells in the ISGRI gamma-ray camera on board the INTEGRAL satellite has led to a choice between CdTe or CdZnTe crystals as detection material in the high-energy detector (HED) of Simbol-X. Different material configurations are under study at the moment and the final decision has not yet been taken. The detector will be composed of 64 very high quality crystals (10 × 10 × 2 (TBC) mm³), each covered with 16 × 16 pixels of about 625 μm in size. Each crystal is connected to its own read-out electronics, the IDeF-X (Imaging Detector Front-end for X-rays) chip, forming a complete individual X-ray camera (CALISTE). This device is developed by CEA/Saclay¹ and is foreseen to operate in the 5 - 80 keV range, partly overlapping the range of the LED. In the current design, eight independently operated sectors of 2 × 4 CALISTE modules will cover the focal plane. More information on the HED can be found in Meuris et al. (2008) and Laurent et al. (2008).

The addition of a Zn component to the detector material leads to a larger bandgap, which generates only a low leakage current, even at room temperature. A very high energy resolution of ~1 keV at 60 keV can thus be reached at -40°C in combination with the radiation tolerant and low-noise readout electronics, which is located directly behind the crystals (Dirks et al.,

¹Commissariat à l'Énergie Atomique, Saclay, France

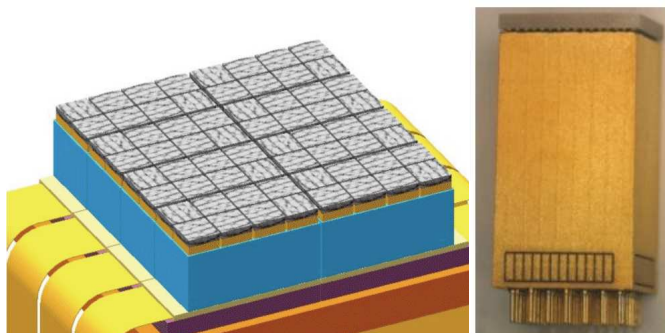


Figure 4.7: Left: illustration of the Simbol-X high energy detector (HED) and supporting structure; right: single 'Caliste'-Module (images: CEA/DAPNIA)

Table 4.4: Parameters of the Simbol-X high energy detector (HED)

Parameter	Value
Format	8.49 x 8.57 cm ²
Pixel format	128 x 128 pixels
Layout	8 x 8 modules with 16 x 16 pixels each
Pixel size	625 x 625 μm^2
Detector material	Cd(Zn)Te
Material thickness	1-2 mm
Energy resolution	~ 1 keV at 68 keV
Abs./rel. timing	$\sim 100 \mu\text{s}$ / ~ 100 ns
Op. temperature	-40°C

2006). Very short peaking times of the signals, generated by the incoming radiation, allow an excellent relative event timing of the order of 100 ns.

The HED is a self-triggered detector, which means there is no frame time as in the LED. When a signal crosses the threshold in one of the pixels, a time tag is generated and the whole module is locked after a short delay for signal shaping. During the following read-out of selected pixels, the respective module is not sensitive to new events (Ferrando and Giommi, 2007).

4.1.5 Active Anticoincidence Detector

The two detectors in the Simbol-X focal plane will be almost entirely surrounded by an active anticoincidence (AC) shield in order to minimize background caused by cosmic rays. This casing, which only leaves a small opening for the X-ray beam, focused by the mirrors onto the detectors, consists of plastic scintillator slabs which create optical photons when hit by radiation. These photons are detected by multi-anode photo-multiplier tubes (PMTs) which are connected to the sides of each slab via optical fibres. Signals from the detectors that coincide within a given short timeframe with signals from the AC can thus be removed from the scientific data, as they most likely are generated by background events and are not due to photons from the field of view. The details about the material decision and the AC logic setup are discussed in the following chapter, as they were strongly influenced by the simulation results obtained in this work in collaboration with the Simbol-X Simulation Group.

4.2 Summary

As a consequence of the emerging multilayer coating mirror technology and the formation flying concept, Simbol-X will feature a large collection area over the whole energy range and, therefore, will overcome the limits for imaging and spectroscopy of all past X-ray observa-

tories. With its low internal detector background and leading edge detector technology, the Simbol-X mission is thus expected to provide a leap in sensitivity in the 10 - 40 keV band of more than a factor 100 with respect to previous missions. This represents a large step ahead for all of the above mentioned science topics and will also allow for numerous new discoveries of yet unknown fainter sources.

As the first project to employ the formation flight concept in a scientific mission, Simbol-X will pioneer a whole new era of X-ray astronomy missions and pave the way for already projected formation flyers like XEUS. Together with the good image quality, the relatively large field of view, good detector quantum efficiency, good resolution and a low internal background, Simbol-X will allow breakthrough studies on black hole physics and census, as well as particle acceleration mechanisms.

Simulations for Simbol-X

In the course of this thesis a Monte-Carlo code, incorporating the GEANT4 toolkit, was developed to simulate interactions of cosmic radiation within the components of the Simbol-X focal plane instrument. During the Phase A of the Simbol-X project, an SPST¹ background group (see Table A.1 for a list of members) was established. This chapter should be considered as part of the more general effort conducted by the group in simulating the performance of the mission. Together with R. Chipaux and C. Klose the author expanded the simulation code to its present extent and capabilities, implementing also the numerous ideas and contributions from the members of the group.

5.1 Challenges and Goals of the Simulation Activities

The Monte-Carlo simulation code was created with the aim to estimate and optimize the detector background by evaluating different geometric configurations and material trade-offs. It contains 1) a highly configurable and expandable model of the detector spacecraft including a set of mirrors at 20 m distance, 2) macros for the generation of particles and photons with spectra and fluxes corresponding to those expected in the designated Simbol-X environment, 3) an optimized list of physics processes that are taken into account at each step of the simulation, and 4) several routines that collect, evaluate and summarize the information about the countless interactions between particles and materials that take place during simulation runtime. These four components are specified in more detail in section 5.2 below.

The development of the simulation code was - and still is - an iterative process, affecting primarily the geometric model of the detector spacecraft. Results of the simulations played a key role in the choice of material composition and thickness for the focal plane assembly, while decisions made by the mechanics group or even on project level in turn affected the simulation setup. In this manner the code was refined (and is still continuously being optimized) towards a simulation-based model, which can be used before and after launch to estimate and verify the instrumental background.

5.1.1 Composition of the Detector Background and Optimizations Measures

In order to achieve the scientific goals of the mission specified in Section 4.1.1, it is essential that a background level of below $3 \cdot 10^{-4}$ counts \cdot cm⁻² \cdot s⁻¹ \cdot keV⁻¹ and below $2 \cdot 10^{-4}$ counts \cdot cm⁻² \cdot s⁻¹ \cdot keV⁻¹ for the LED and the HED, respectively, is reached. As this figure is far

¹Science Payload Simulation Team

below the background measured in currently flown X-ray CCD cameras, e.g. on XMM-Newton or Chandra, an intense effort is undertaken to optimize the Simbol-X instrument. Each of the components that contribute to the internal background has been analyzed in detail. The input from the simulations made it possible to efficiently suppress them by mainly optimizing the detector housing (graded shield composition and thickness, anticoincidence (AC) material, segmentation and logic), the detector deadtime and the shape and weight of the collimator. More details on optimizing measures are given in the following list below.

The background of the Simbol-X detectors consists of five main components:

- **the diffuse Cosmic X-ray Background**

The origin of the nearly isotropic sky background of cosmic X- and γ -rays (CXB) has been a matter of interest and controversy since it was discovered with early X-ray counters flown on rockets. Today, attempts to attribute the CXB to uniform emission at truly cosmological distances seem to be ruled out, since discrete source populations, which extend to high redshifts (e.g. various types of AGN), have been resolved (or are predicted to exist by the current models) at the relevant energies (see *Fig. 5.4 in Chapter 4*) that account for - or even overproduce - the measured diffuse flux (Gruber et al., 1999; Worsley et al., 2005). To avoid counts on the detectors caused by this radiation coming from outside the field of view, passive shielding in terms of a graded-Z shield (see *Section 5.2.1.2 for its composition*) is implemented around the detector to stop the photons. Furthermore, a section of the calibration wheel, consisting of the same materials, can be rotated in front of the detectors to close the field of view.

- **prompt background induced by interactions of high energy protons**

Interactions of high energy cosmic-ray protons with material in the close vicinity of the detectors produce secondary particles and photons, that lead to an increase of the instrument background. In order to suppress these undesired background counts, a coincidence tagging system is implemented around the detectors, which tags detector events in a given time window after the active anticoincidence detector registered an incoming proton.

- **delayed component from induced radioactivity**

Radioactivity induced in the spacecraft materials by cosmic rays produces a delayed background in sensitive instruments. This effect can be observed, for instance, in the ISGRI instrument aboard the INTEGRAL satellite (F. Lebrun, priv. comm.). First results of our group for Simbol-X indicate that its contribution to the overall background is of the order of $< 1\%$. This might largely be due to the passive shielding mentioned above. However, radioactivation strongly depends on the implemented materials and their respective locations, and thus a more precise evaluation is foreseen as soon as a more detailed and realistic mass model of the spacecraft is available.

- **soft proton interactions with the detector**

Another source of background in focusing instruments that shows a strong and unpredictable variability are *soft proton flares* which are attributed to low energy protons (below

~ 300 keV) that are funneled onto the detectors by the telescope mirrors (see *Strüder et al., 2000* and *Strüder et al., 2001*). To prevent this effect, a magnetic diverter, consisting of strong permanent magnets on the mirror satellite, is discussed at the moment.

- **other contributions**

The fact that the Simbol-X mission features two spacecraft makes the prevention of stray-light contamination a more difficult task, compared to previous missions with only one satellite. To confine the field of view of the detectors in a way that only X-rays which are correctly focused by the mirrors can reach the detectors, several measures are foreseen: a sky baffle with a diameter of 3 meters surrounding the mirrors, radial shielding in between the mirror shells and a long (~ 2 m) collimator on the detector spacecraft, all consisting of heavy, X-ray absorbing materials and/or a graded Z-shield, were introduced (see *Fig. 5.1*). In addition, the LED will possibly be coated with a 150 nm thick aluminum layer in order to make it insensitive to the optical photons created by the positioning system of the two satellites.

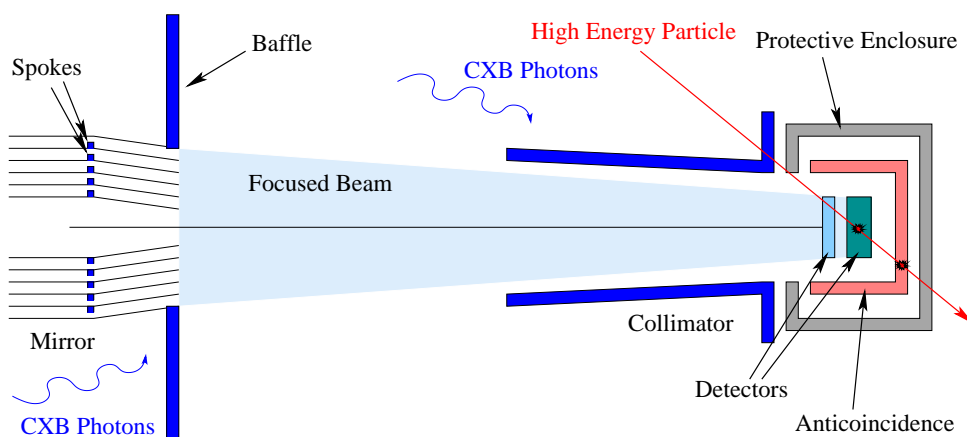


Figure 5.1: Simplified schematical drawing (not to scale) of the two Simbol-X spacecraft illustrating the geometry of the shielding measures against straylight contamination (reproduction of an illustration by Yvon Rio, CEA, Saclay).

Background induced by magnetospheric and solar particles has not been considered important, as observations with Simbol-X are scheduled only above 73,000 km (see *Fig. 4.2*) and outside of the solar flare periods.

Each of the five components above has been investigated and provisions to reduce them are described in more detail in the following. With the input of the simulations it was possible to identify suitable solutions to reduce the respective contributions of those components to the overall background below the required limits.

5.2 Parameters and Characteristics of the Simulation Environment

The following sections contain a more detailed description of the main components of the simulation environment, created for the estimation and optimization of the instrument background.

5.2.1 The Geometric Model

The geometric model used for the simulations is an approximation of the latest technical drawings of the Simbol-X Focal Plane Assembly (FPA) by using only the simple geometric volumes (cylinders, boxes, etc) that are supported by Geant4. Although hard-coded in C++, it is still rather flexible and has a lot of variable parameters such as material thickness and material composition of most detector elements, which can be edited even during runtime via so-called *macros* (batches of simulation control commands).

As mentioned already in Section 5.1 above, the geometric model for the simulations evolved over time with the progress of the mission. However, there were three major releases of the model (see Fig. 5.2), which were used in simulations, each for a little less than one year and each one superceding its predecessor in the level of accuracy and detail.

Addendum: A fourth version of the geometry was developed only recently, implementing all the improvements suggested after previous simulations. This version and first results obtained with it are described separately in Section 5.3.9. The term 'current version' for the third version used throughout this chapter is hence no longer valid.

5.2.1.1 Model History

In the first version of the geometric model the HED design still consisted of a hexagonal matrix of CdZnTe modules, and the LED was mounted on an aluminum structure at a distance of almost 6 cm. The cube-shaped aluminum detector box was positioned in the center of the spacecraft, which was then represented by an empty cylinder with walls also made of 5 mm thick aluminum. Inside the box was an anticoincidence detector (AC) and a graded shielding (GS), with already the thicknesses used today but at that time still on the outside of the AC.

The collimator on top was at first simplified as a straight tube also made of the GS composites. Later, a function for the wall thickness was implemented to maintain a desired constant effective thickness with respect to the angle of incident radiation on the detector. This allows to save most of the weight, as in this way the wall thickness is rapidly decreasing with the distance from the detector.

For a collimator that is shaped as an ordinary tube with parallel inner walls, this wall thickness at a distance d from the detector is given by:

$$\text{thickness}(d) = \text{thickness}_{\text{eff.}} \cdot \cos \left(\arctan \left(\frac{d}{R_{\text{tube}} + \frac{1}{2} \cdot \text{LED}_{\text{dia}}} \right) \right) \quad (5.1)$$

with R_{tube} : radius of the collimator tube, LED_{dia} : diagonal of the LED

In the second version of the geometric model, the detector box was placed on top of the spacecraft and inside a protective box with 1 cm aluminum walls. The detector case itself was separated in two halves, allowing cables to pass through a small gap in between. In order not to allow particles to enter through this gap unnoticed, an additional inner AC slab was placed on each side of the detectors, leaving no possible tracks towards the detectors unless the AC was also hit. The HED configuration was changed to an 8×8 grid and the distance to the LED was reduced to 4 cm (see Fig. 5.2, middle).

Furthermore, a thin metal foil between the detectors was introduced into the design in order to prevent electronic crosstalk between them and to stop potential X-ray fluorescence photons, 'backscattered' from the HED, that could be detected by the LED (see Chapter 6 for more details on this effect).

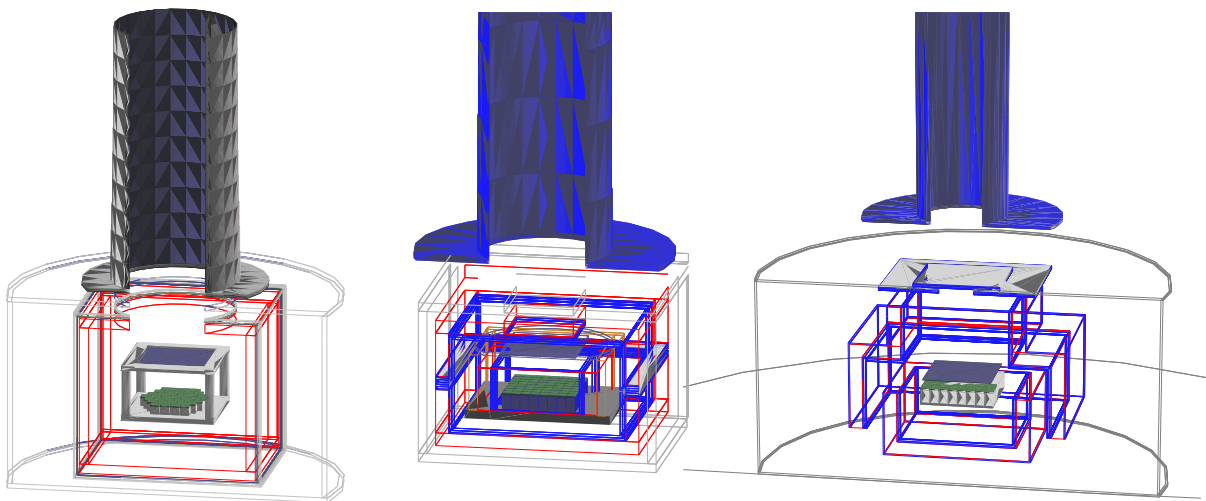


Figure 5.2: Evolution of the geometric model during Phase A. From left to right versions 1 to 3 of the model are depicted. Different materials are shown in different colors: light grey - aluminum, red - anticoincidence detector, dark blue - LED, green - HED, dark grey to light blue - graded shielding (see also Fig. 5.3).

5.2.1.2 Current Version

The first three versions of the geometry have been originally designed by the author. Beginning with the third one, the geometries have been developed in collaboration with R. Chipaux and other members of the simulation group. In the current model (see Fig. 5.2 right and also Fig.

5.3), the detector box is located inside a 5 mm thick aluminum cylinder, called *protective enclosure*, which is placed on top of another cylinder representing the spacecraft. In section 5.4 below, the results of a simulation run with the most recent parameters (physics list, cuts, input spectra, etc) are presented, comparing the background of the older versions to the current one.

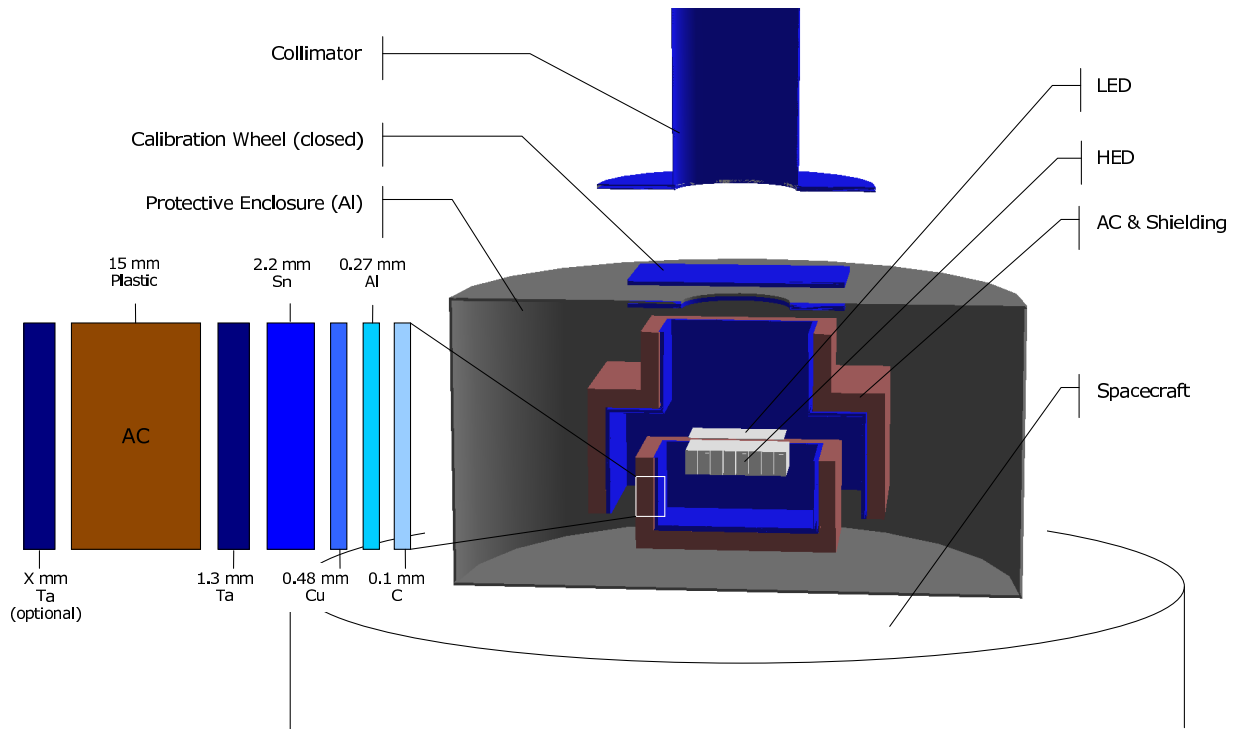


Figure 5.3: Current model of the Simbol-X focal plane used in the GEANT4 Monte-Carlo simulations. An optional external shield can be placed around the AC. The indicated cylinder below the geometry represents the detector spacecraft.

The central elements of the current model are (as in all previous models) the two detectors. The low energy detector is as before represented as a monolithic slab of silicon with dimensions of $80 \times 80 \times 0.45 \text{ mm}^3$. To allow a much more compact design of the detector box and to minimize the effects of the different positions on the focus, the distance to the high energy detector was reduced to 1 cm. The HED is composed of 8×8 modules of cadmium zinc telluride ($\text{Cd}_{0.9}\text{Zn}_{0.1}\text{Te}$, $10 \times 10 \times 2 \text{ mm}^3$), separated by 0.625 mm gaps. The electronics of each module is located directly underneath and represented by a small box (height: 17.5 mm) with a material composition approximating that of the real Caliste modules.

The two detectors are surrounded by two nested individual cases and a top section of AC, which consists of 15 mm thick plastic scintillator slabs, segmented into top, lateral and bottom parts, leaving some room for cables, heat pipes and supporting structures. On the inside of the AC, towards the detector, a graded-Z shield is mounted to reduce the photon flux. With its baseline composition of (outside to inside) 1.3 mm tantalum, 2.2 mm tin, 0.48 mm copper, 0.27

mm aluminum and 0.1 mm of carbon, it is designed to absorb photons below 100 keV and to leave X-ray fluorescence below 0.3 keV and therefore below the detection limit of the LED. An aluminum protective enclosure surrounds the above described parts of the camera.

Above the aperture of the camera, but still below the collimator, is a $10 \times 10 \text{ cm}^2$ plate of graded shield, which represents the closed position of the calibration wheel as it can open or close the field of view during the simulation by user command. All the background simulation results given in this work are performed with the calibration wheel *closed*, where not stated otherwise.

The collimator itself consists of three independent tubes, which are also made of the GS composition and that are connected together end to end, constituting the collimator's total length of now $\sim 1.8 \text{ m}$. As in the earlier models, the thickness of the tubes decreases with the distance from the detector in order to save weight and to maintain a constant effective thickness for incoming radiation. The inner radius of the tubes, however, increases with the distance to compensate for the dimensions of the focused X-ray beam (*as illustrated in Fig. 5.1*).

The detector spacecraft is roughly approximated by a cylindrical volume filled with aluminum with a height of 1 m, a radius of 0.5 m and a mean density of 0.4711 g/cm^3 , located directly below the protective enclosure (*see Fig. 5.3*).

The mirror spacecraft is an optional extension to the simulations. In its present state, it is derived from a model that was developed for XMM simulations (Nartallo et al., 2001). It consists of 58 mirror shells at a distance of 20 m from the LED. It has not been used in this work as the only important influence of the mirror spacecraft onto the detector background is through the focusing of low energy protons, which has not been simulated. Therefore, it is only mentioned here for completeness.

5.2.1.3 *Discussion of the Current Version of the Geometric Model*

The current version of the model described here omits a lot of details like cables, front-end electronics and structures, but otherwise accurately represents the central components of the mechanical design as of January 2007. Especially the structures, components and materials that are close to the detectors have the most influence on the background, so they will be addressed in more detail in upcoming models that will also incorporate an adequate representation of the mirror spacecraft. Recently a new model of the latest focal plane design has been created. Technical drawings of it are shown in Fig. 5.16 and first results obtained with it are presented in Section 5.3.9.

5.2.2 *Incoming Particle Fluxes and Spectra*

The isotropy of the flux of cosmic photons and particles in the designated space environment for Simbol-X is simulated by emitting particles from random points on a sphere surrounding the detector spacecraft. The radius of this sphere (20 m) is much larger than the size of the detector

spacecraft model, which would fit into a box of $3 \times 1 \times 1 \text{ m}^3$. The direction of emission from the sphere is restricted to a small cone containing a sphere around the spacecraft in order to save computation time and to allow conversion from *number of particles generated* into the *duration the spacecraft has been exposed to particles* (see section 5.2.4 for details).

In this work, only impinging cosmic photons and protons are studied (neglecting other primary particles such as ions and electrons) as these are the major causes for the relevant types of background depicted in section 5.1.1.

5.2.2.1 CXB Photons

For studies regarding the effects of the Cosmic X-ray Background (CXB) photons we use the intensity and spectrum given by Gruber et al. (1999). In their paper on the spectrum of diffuse cosmic hard X-rays, the authors give an empirical analytical expression (Eqn. 5.2) to fit the measurements obtained with the *High Energy Astronomical Observatory 1* (HEAO 1) below 500 keV and also above those from the COMPTEL and EGRET instruments on board the *Compton Gamma Ray Observatory* (CGRO). For our simulation purposes, this formula is extrapolated down to 1 keV and an upper limit is set at 100 MeV where the flux becomes negligible. The total flux integrated over this range and over 4π is equal to $197.23 \text{ photons} \cdot \text{cm}^{-2} \cdot \text{s}^{-1}$, which is later used again to calculate the normalization of simulated count rates.

$$\begin{aligned}
 3\text{-}60 \text{ keV:} & \quad 7.877 \cdot E^{-0.29} \cdot e^{(-E/41.13)} \frac{\text{keV}}{\text{keV cm}^2 \text{ s sr}}, \\
 > 60 \text{ keV:} & \quad 0.0259 \cdot \left(\frac{E}{60}\right)^{-5.5} \\
 & \quad + 0.504 \cdot \left(\frac{E}{60}\right)^{-1.58} \\
 & \quad + 0.0288 \cdot \left(\frac{E}{60}\right)^{-1.05} \frac{\text{keV}}{\text{keV cm}^2 \text{ s sr}} \quad (5.2)
 \end{aligned}$$

5.2.2.2 Cosmic-Ray Protons

Concerning the protons, we implemented a spectrum that was computed by Claret (2006) for the expected launchdate. This document aimed at giving a first estimation of the total ionization dose for Simbol-X during the whole mission. For different launchdate scenarios, the fluxes of trapped electrons and protons, solar particles and cosmic rays have been calculated. The spectrum of cosmic ray protons at solar maximum (calculated with the CREME86 model of the OMERE software) was adopted for the simulation and the range of the spectrum was restricted to between 10 MeV and 100 GeV, as protons with energy below the lower limit did not penetrate the protective enclosure at all and the flux above 100 GeV is negligible for the durations simulated. The integral proton flux over 4π equals $2.31 \text{ protons} \cdot \text{cm}^{-2} \cdot \text{s}^{-1}$.

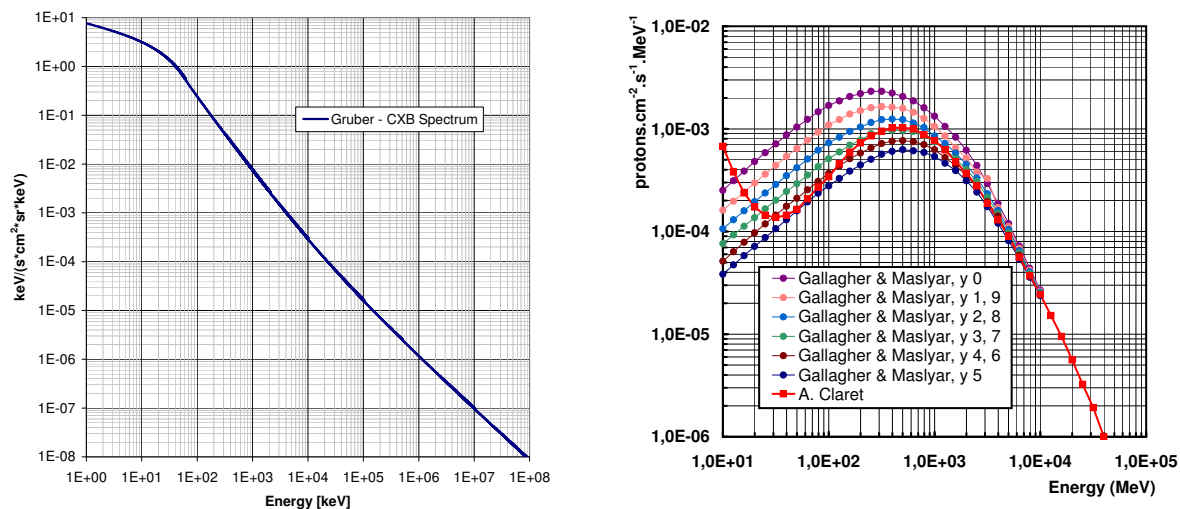


Figure 5.4: Photon spectrum of the Cosmic X-ray Background (left figure) as given by Gruber *et al.* (1999) in Equation 5.2 and proton spectrum given in Claret (2006), calculated with CREME86 (squares) for a Simbol-X launchdate in mid 2013 and used in the presented simulations (right). Spectra published by Ogallagher and Maslyar (1976) for different periods of the solar cycle are shown for comparison.

5.2.3 Considered Physics Processes

As stated in Section 2.4, GEANT4 permits the application developer to select the physics that is relevant for his simulation. In fact, the user has to specify exactly the processes that might possibly be applied to the particles during their steps along their tracks. This opportunity to switch specific parts of physics and particular interactions simply on and off provides an excellent way to probe the causes of not readily understood phenomena, and to identify the contribution of a single process. It also provides an option to debug the simulation code by reducing it to very simple physics and well-known cases.

In preliminary studies, only electromagnetic interactions were included in the simulations (Tenzer *et al.*, 2006). For simulations in this work, hadronic interactions were added and also an optional radioactive decay module is included. The rather voluminous Tables A.3 and A.2 in the Annex give a complete list of all physics processes and particles from the *PhysicsList* included in the simulations.

A default *cut length* (see Sect. 2.4.1.2) of 0.01 mm was chosen after a study identified it as the best compromise between accuracy and computation time (see Fig. 5.5). For the region containing the 'spacecraft' cylinder, the cut length was raised to 1 mm in order to save computation time without affecting the count rates at all.

5.2.4 Event Data Evaluation

To collect data about the interactions and particle tracks generated during the simulation, so-called *sensitive detectors* and *hits collections* were implemented by R. Chipaux of the SPST background group. These allow to access and record information like particle type, position, momentum, interaction process type and deposited energy at every interaction within regions declared as *sensitive* via special functions provided by GEANT4. Simulations presented in the frame of this work make use of an older interface that does exactly the same without resorting to these built-in functions, but using custom-designed ones instead. All the information mentioned above about such a *hit* of a detector is recorded and can be stored in a FITS¹-file during or at the end of a simulation run. In addition, a short summary text displays the sum of all interactions within the energy range of each detector.

The resulting data are processed further with IDL to detector *events* by filtering the respective detector energy range (LED: 0.5 keV to 20 keV; HED: 5 keV to 100 keV; AC: above 100 keV) and *by adding up (for each detector) all energy depositions caused by one common primary particle*. A time offset is added to the time of each event, as the simulation code only tracks one primary particle (and all its triggered secondaries) at a time and then resets the time to zero with each newly generated particle.

Due to this 'per particle' approach of the Monte-Carlo simulation, the user is provided only with information about the number of primary particles that have been generated and has to conclude from here onto the elapsed time. This calculation of the time offset, that denotes the amount of time in which the spacecraft has already been exposed to particles or radiation, is done via the incoming particle flux as shown in Equation 5.3.

$$\text{elapsed time} = \frac{n_P}{4\pi(\tan(\alpha) \cdot r_S)^2 \cdot \text{flux}_{int}} \quad (5.3)$$

n_P is the number of primary particles, α the opening angle of the momentum cone, r_S the radius of the outer particle generation sphere and flux_{int} the integrated flux from the input particle spectrum. Thus, a simulation with a number of 10^{10} primary CXB photons corresponds (with standard settings) to roughly 1.6 kiloseconds exposure to CXB radiation in reality.

This concludes the description of the environment in which all of the following simulations were performed (where not explicitly stated otherwise) and which can and will be used as a solid foundation for future work and extensions.

5.3 Details of the Performed Simulations and their Results

As mentioned in the introduction to GEANT4 in Chapter 2, the toolkit, as well as its dependencies and extensions, are upgraded regularly. In addition, our own simulation code evolved quite

¹FITS - Flexible Image Transport System, a common file format in astronomy

a bit over time, which makes track-keeping of all the different versions and releases essential in order to compare results. Table 5.1 lists all the versions used in standard simulations. The following sections each report on one or more different aspects of simulations that were performed in the frame of this work to investigate, judge and optimize the properties of the Focal Plane Assembly (FPA).

Table 5.1: Overview of versions of currently implemented simulation modules, GEANT4 toolkit and implemented extensions.

Module / Software Package	Implemented Version
Geometry	version 3, including spacecraft
PhysicsList	from Darmstadt, with correction
Data Evaluation	from Tübingen
Geant4	Geant4.8.2
CLHEP library	version 2.0.3.1
low energy electromagnetic processes	G4EMLOW 4.2
NeutronHPCrossSections	G4NDL 3.10
G4LevelGammaData	PhotonEvaporation 2.0
G4RadioactiveData	RadioactiveDecay 3.1

5.3.1 Particle Production Cuts, Accuracy and Computation Time

As explained in Chapter 2, GEANT4 employs range cuts to suppress the generation of secondary particles in some interactions, when their range (internally converted to an energy for each respective material) would be below a certain user defined threshold. However, for our investigation of the instrument background, the default cut length of 1 mm is too large, as a lot of - from the view of collider physics - 'low energy photons' are not generated. Instead, their energy is deposited locally in the surrounding materials. In this regard, a study was conducted to analyze the effects of changing the cut length in the detector materials. With the resulting count rates it has been decided to fix the length to 0.01 mm for all the materials close to the detector (including also the collimator) and to leave the later introduced large spacecraft region below the detector at the default cut length of 1 mm. This allowed to keep the computation time at a tolerable level while being close to the maximum count rate obtained with even shorter cuts.

Figure 5.5 shows a plot of the normalized HED count rate and corresponding simulation times of a recent re-simulation of that study with the current geometry and physics list, confirming the first results and decisions. The strong increase of computation time when decreasing the cut length below our selected value forbids further refinement at the moment, because in the same simulation time less statistics can be accumulated, introducing eventually an even larger uncertainty in the results.

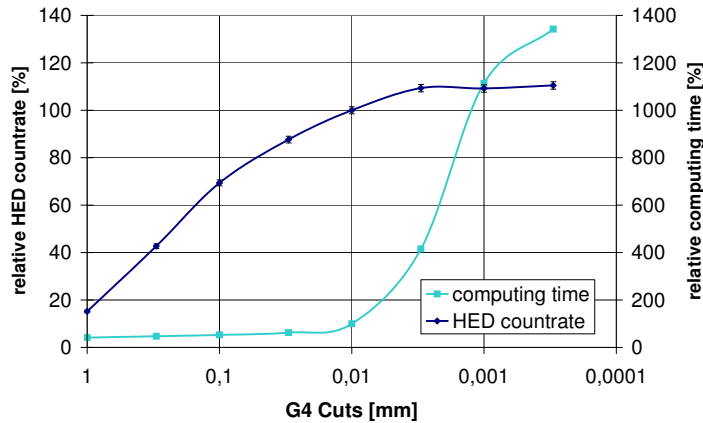


Figure 5.5: HED count rate (normalized to 0.01 mm cut length) as a function of cut length (logarithmic scale). Also plotted is the corresponding normalized computation time of each simulation. There is only a $\sim 10\%$ change and a clearly observable saturation of HED counts when going below 0.01 mm, while the computation time increases dramatically with this transition.

5.3.2 Simulation of the Quantum Efficiency of Both Detectors

In this simulation, the quantum efficiencies (QE) of both detectors are simulated. As the final composition and structure of the detector materials is yet to be defined, this simulation can only assist in confirming the calculations of the manufacturing labs (LED: MPE/HLL, HED: CEA, Saclay) and help in comparing different configurations. Furthermore, it constitutes another way of verifying the correct implementations of the geometric models and low energy physics processes into the simulations.

While in the standard simulations for Simbol-X only a $450 \mu\text{m}$ slab of silicon is used to represent the low energy detector, different tentative structures are implemented in this particular study. Above the active $450 \mu\text{m}$ of silicon, a realistic 6 nm layer of dead (i.e. non-sensitive) silicon is added. To stop photons of the inter-satellite positioning system, which are known to create an optical load of $5 \cdot 10^4$ photons per frame ($128 \mu\text{s}$) and pixel on the LED, an aluminum layer of about 100 nm - 150 nm thickness has to be imposed on top of the silicon. To filter additional UV radiation, a layer of 40 nm of SiO_2 and another of 40 nm Si_3N_4 can be inserted in between the Si and the Al (P. Lechner, priv. comm.).

The high energy detector consists of a 2 mm slab of CdZnTe with a composition of (mass fractions) 45% Cd, 5% Zn, 50% Te and a density of 5.81 g/cm^3 . None of the detectors is pixelized or has any dead areas for this simulation.

The QE is simulated by shooting a flat spectrum of photons at the detector and returning the ratio of registered vs. generated particles for a respective energy bin. The results of the simulations for various layer configurations of the LED are shown in Figure 5.6. In the plots, the prominent absorption edges of (left to right) nitrogen, oxygen, aluminum and silicon can be observed clearly. The nominal LED energy range starts at 0.5 keV, but with more material layers on top of the LED, the QE drops significantly at those lower energies. Thus, the material composition and layer thickness is still discussed at the moment in order to achieve the lowest impact possible on the scientific performance of Simbol-X.

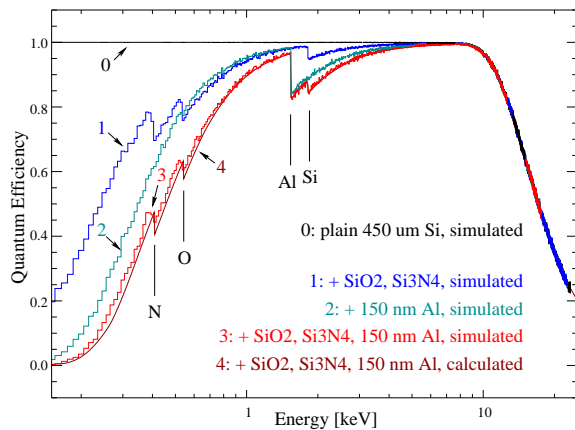


Figure 5.6: Quantum efficiency of the Simbol-X low energy detector for different material compositions / layer structures

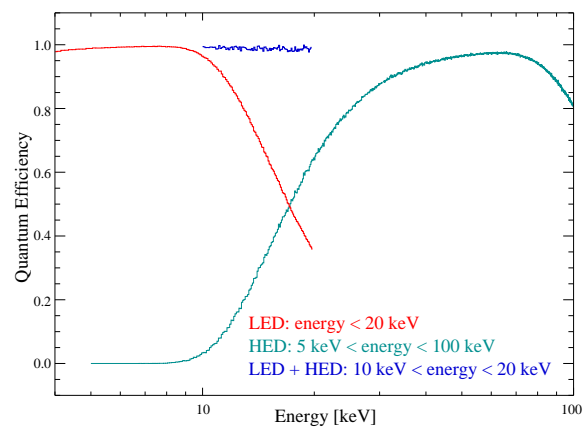


Figure 5.7: Quantum efficiency of the Simbol-X high energy detector and the combined quantum efficiency for the transition range

To provide a comparison with work done at MPE/HLL, a calculated curve of the most probable final configuration is added (lowest curve in Fig. 5.6). The simulation perfectly agrees with it, even below the 250 eV accuracy limit of the low energy physics of GEANT4.

In Figure 5.7, the simulated transition range between the two detectors is presented, showing the QE of the LED again on the left in red and that of the HED on the right in green. In addition, the sum of both detectors in the range between 10 keV and 20 keV is shown in blue. As it was designed, this value is close to 1.0 over the whole range. It can be noticed from this figure, that wherever the upper energy threshold of the LED is finally placed, a sudden drop in the camera's total QE will result at this point.

5.3.3 Expected Simbol-X Detector Background

The estimation of the Simbol-X detector background reported here is obtained from several simulations, each analyzing a different component of the background. Preliminary results for the Simbol-X instrument background caused by the CXB component in this 'closed' condition have been already published in Tenzer et al. (2006) but are already surpassed in accuracy within this work, due to a much more detailed detector model and a more comprehensive list of physics processes. In the current simulation environment, the count rates are clearly dominated by the cosmic protons with a contribution of around $6 \cdot 10^{-3} \text{ cts} \cdot \text{cm}^{-2} \cdot \text{s}^{-1} \cdot \text{keV}^{-1}$ in both detectors (see Fig. 5.8 and Table 5.2 below). The anticoincidence detector (AC) is designed to tag most of these background events and allows an effective reduction of the proton background to about $4 \cdot 10^{-4} \text{ cts} \cdot \text{cm}^{-2} \cdot \text{s}^{-1} \cdot \text{keV}^{-1}$. In addition, the Cosmic X-ray Background (CXB) photons give rise to a rate of $1 \cdot 10^{-4} \text{ cts} \cdot \text{cm}^{-2} \cdot \text{s}^{-1} \cdot \text{keV}^{-1}$ for the LED and $3 \cdot 10^{-4} \text{ cts} \cdot \text{cm}^{-2} \cdot \text{s}^{-1} \cdot \text{keV}^{-1}$ in the HED. As expected, the AC is not efficient in this case.

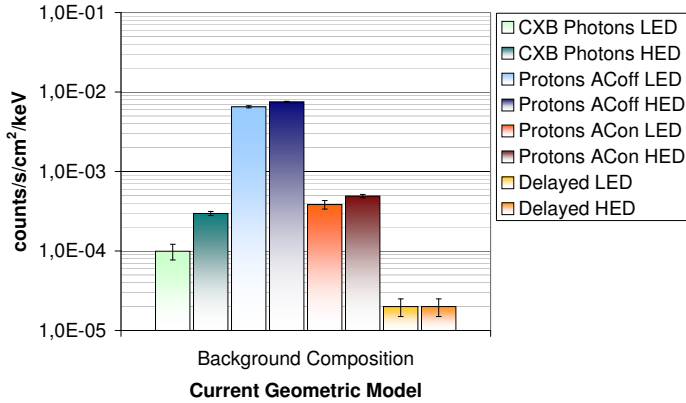


Figure 5.8: Composition of the Simbol-X detector background for geometry version 3

Table 5.2: Composition of the Simbol-X detector background for the third geometry version

LED	counts/s/cm ² /keV
CXB photons	$0.93 \pm 0.22 \times 10^{-4}$
Protons (AC on)	$3.84 \pm 1.00 \times 10^{-4}$
Delayed	$0.20 \pm 0.10 \times 10^{-4}$
Total (AC on)	$5.03 \pm 0.75 \times 10^{-4}$
HED	counts/s/cm ² /keV
CXB photons	$2.97 \pm 0.17 \times 10^{-4}$
Protons (AC on)	$4.91 \pm 0.55 \times 10^{-4}$
Delayed	$0.20 \pm 0.10 \times 10^{-4}$
Total (AC on)	$7.45 \pm 0.46 \times 10^{-4}$

Radioactivity induced by cosmic rays in the materials close to the detectors leads to a *delayed* background component. First results of simulations reported in Klose (2007) indicate that its relative contribution to the overall background is rather negligible. However, further studies are foreseen when a more detailed mass model of the spacecraft is available. Studies regarding the background level caused by soft protons which are directed by the mirrors onto the detector have not yet been completed (see Section 5.3.8 for further results of the simulation group).

All of the above values were obtained using non-pixelized detectors, i.e. by adding the deposited energies of all secondary particles that are generated by a common primary particle and reach a detector. In this way, only one count can be generated in each detector with each new primary particle, just as if there was only one large pixel. For the LED simulations, the accepted energy range is $0.5 < \text{energy} < 20 \text{ keV}$, for the HED it is $5 \text{ keV} < \text{energy} < 100 \text{ keV}$. The default AC trigger threshold is at 100 keV. At the end of a simulation *run*, the total number of those counts in both detectors is divided by the elapsed time (given in Eqn. 5.3), the detector area and the energy range of the detector to calculate the background values. This implies a rather simplified treatment of the background flux, which is averaged as if it were constant over the whole energy range of the instrument. However, this assumption is justified by the shape of the simulated background spectra, presented in the section below.

The total background count rate (AC on) amounts to $(5.03 \pm 0.75) \cdot 10^{-4} \text{ cts} \cdot \text{cm}^{-2} \cdot \text{s}^{-1} \cdot \text{keV}^{-1}$ for the LED and $(7.45 \pm 0.46) \cdot 10^{-4} \text{ cts} \cdot \text{cm}^{-2} \cdot \text{s}^{-1} \cdot \text{keV}^{-1}$ for the HED. As the necessary total background level to meet the top-level scientific requirements is of the order of below $2\text{-}3 \cdot 10^{-4} \text{ cts} \cdot \text{cm}^{-2} \cdot \text{s}^{-1} \cdot \text{keV}^{-1}$ for both detectors, the SPST group, together with scientists and engineers from the involved labs, is working hard on improving the instrument. Some of the more interesting ideas to further reduce the background level are presented in subsequent sections.

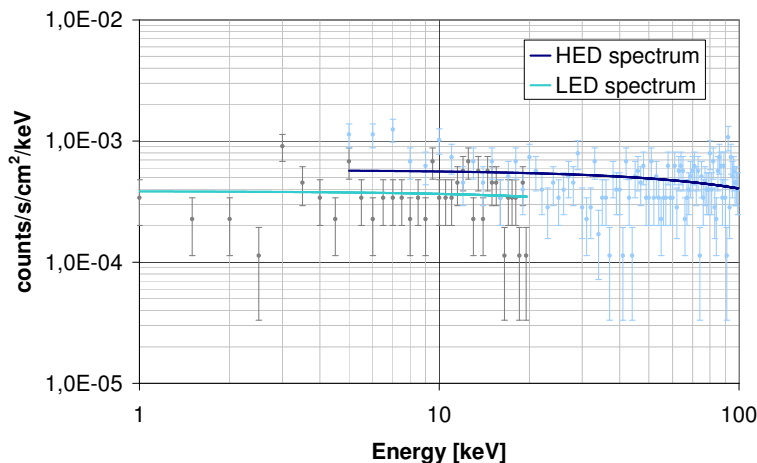


Figure 5.9: Simulated LED and HED spectra of the remaining (after AC reduction) background events induced by protons and CXB photons as estimated to be measured during an observation with the calibration wheel closed. The lines are just a simple average and do not represent any kind of fitting.

5.3.4 Simulated Remaining Background Spectra

Due to the overall low instrument background, very long computing times are required for a simulation to accumulate sufficient statistics to constitute a reasonable spectrum of the background. Figure 5.9 shows the combined (from protons and CXB photons simulations) LED and HED background spectra as expected to be measured in a calibration observation with the calibration wheel closed. As stated in the previous section, each detector consists of only one pixel, and the energies of secondary particles belonging to one *event* are added up. The total amount of particles handled in this simulation corresponds to a ~ 0.69 ks 'closed' measurement.

To assemble the two spectra of the detectors, the valid energy range of the LED is divided into 0.5 keV wide bins, that of the HED into 1 keV bins. Events that are tagged by the anticoincidence detector are removed. The resulting spectra are virtually flat, with only subtle variation over the whole instrument range, supporting the averaging specification of the total background in the previous section. Unfortunately, the statistics, consisting of only a few counts per bin, is still insufficient to identify lines in the spectra. This will be helpful in optimizing the shielding measures and the positions of materials very close to the detectors.

5.3.5 Performance of the Graded Shield

As mentioned in Section 5.2.1.2 above, the graded shield is designed to stop photons below 100 keV and to leave the induced X-ray fluorescence below the detection range of the LED. The rather heavy material composition (weighing 4.30 g per cm²) is used in many locations of the detector and mirror spacecraft to stop photons impinging from outside the field of view. Thus the performance of the GS is of crucial importance to the instrument background.

In Figure 5.10, the result of a simulation study, conducted to check the actual efficiency of the graded shield over the relevant energy range, is presented. For the baseline material configuration and for a GS with an enhanced tantalum layer, the stopping power was simulated by

shooting photons with a flat spectrum between 100 and 500 keV at the GS and by summarizing the energy of all the emerging particles (including e.g. X-ray fluorescence photons) on the other side. The probability of this sum to be below the detection range of the LED is plotted in the graph as a function of the energy of the primary photon.

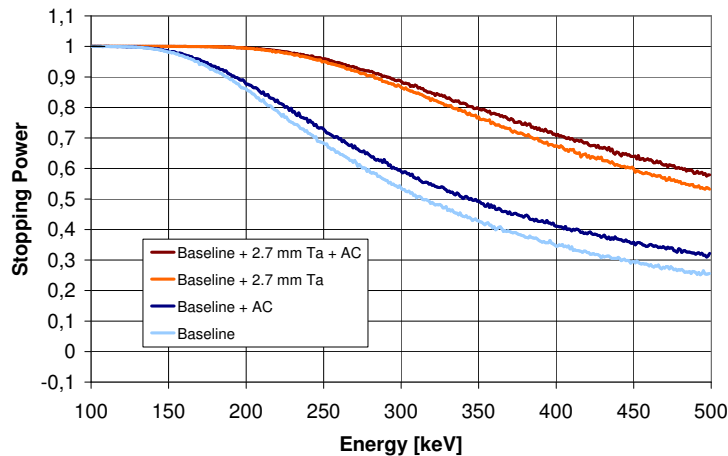


Figure 5.10: Efficiency of the Simbol-X graded shield as used, for instance, in the collimator: The probability for the primary photon and all induced secondary particles to be stopped within the graded shield or to have a remaining energy below 0.5 keV is shown as a function of the energy of the primary photon. Presented are curves for the baseline material composition (see Sect. 5.2.1.2) and for a GS with an extended tantalum layer (4.0 mm in total) with and without AC.

The results validate the previous calculations and confirm that the intended effectivity of the GS for the region below 100 keV is reached. However, the additional tantalum layer proved quite effective against photons up to 250 keV and was, in spite of its weight, adopted for further studies.

5.3.6 Effects of Thickness Variation of the Tantalum Component in the Graded Shield

With the intention to further reduce the instrument background, a study on the effect of increasing the tantalum layer thickness within the graded shield of *only the detector box* was performed, using the full geometric model. Starting with 1.0 mm, which lies even below the baseline thickness, and going up to 4.0 mm (as in Fig. 5.10), the detector count rates were simulated again for incident protons and gammas, the values at current baseline thickness being the same as presented in Table 5.2.

It can be observed from the results of this study, summarized in Fig. 5.11, that the additional tantalum affects only the photon induced background in a positive way, i.e. the LED and HED count rates decrease over the whole analyzed range by $\sim 20\%$ and $\sim 50\%$ respectively. On the other hand, one can observe that the count rate induced by protons (AC off) increases at the same time by a factor of 1.35 in both detectors. Although these additional counts are all tagged by the AC and thus the proton induced background (AC on) remains stable, the increase of tantalum leads to an unwanted higher AC count rate, which has a negative impact on the scientific performance of the detectors, especially on the LED as shown in Section 5.3.7 below. Due to this effect and also because of the increased weight of the heavy additional material, the final conclusion of this study was to leave the baseline tantalum thickness at 1.3 mm.

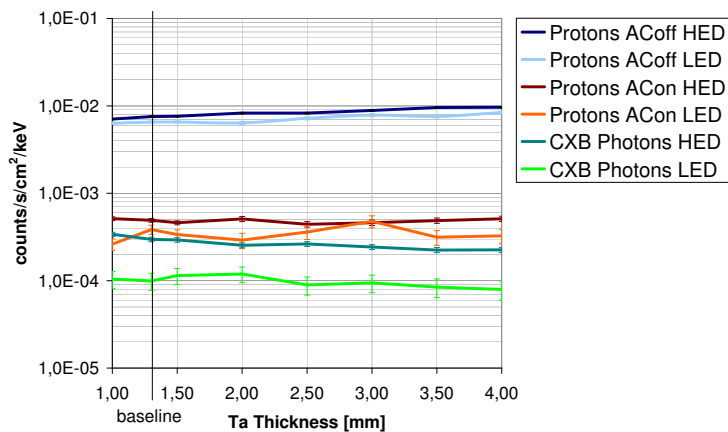


Figure 5.11: The Simbol-X detector background composition as a function of the thickness of the tantalum component in the graded shield: Although the CXB photon induced background decreases, the proton induced component (AC off) intensifies and causes a higher AC count rate. The proton induced count rate after AC remains constant.

5.3.7 Reducing the LED Deadtime by Optimizing the Anticoincidence Detector

The anticoincidence detector is designed to tag all charged particles passing through the FPA. This implies that no holes must be left in the AC layout, except for the field of view. The baseline configuration for the AC has always consisted of 15 mm thick plastic scintillator slabs divided into three (top, lateral and bottom) groups, with each slab connected individually via a set of optical fibers to multi-anode photomultipliers. Other scintillator materials like CsI, NaI and LaBr₃ were also under study by the SPST background group but were discarded for different reasons, as detailed in Section 5.3.8.

In order to cope with the HED time resolution, the anticoincidence should have a time resolution of the order of 50 ns. In this way, the AC assures that the detectors reach the low background level required in the top-level scientific requirements. However, the larger the total surface area of the AC slabs around the detectors is, the more particles pass through it and the AC count rate increases without being any more effective. With the count rate going up, a higher deadtime of the detectors is induced, as more frames of the LED and more events in the HED are vetoed. This effect is especially severe for the LED (as shown in Fig. 5.12) because of its fixed long exposure and readout cycle. The HED on the other hand has an event triggered readout, so only a very short time interval is affected. The fraction of deadtime caused by the AC in a detector is given by the probability of an AC signal to fall into a measurement and readout interval (for the LED, this is the *frame time*) of that detector, thus vetoing the measured signal:

$$\Delta T_{\text{dead}} = 1 - e^{-(\text{AC counts/s}) \cdot (\text{interval length})} \quad (5.4)$$

A high deadtime in a detector seriously affects its scientific output, as the signal to noise (S/N) ratio for faint sources drops and the sensitivity of the instrument deteriorates.

In Figure 5.13 the S/N ratio for a faint source in the LED is calculated for the two most probable frame times. In this calculation, the source is assumed to generate 100 counts (flat

spectrum over 10 keV) within an extraction area of 0.03 cm^2 in an exposure time of 100 ks. For the background, a total of $3 \times 10^{-4} \text{ cts} \cdot \text{cm}^{-2} \cdot \text{s}^{-1} \cdot \text{keV}^{-1}$, as requested by the top-level scientific requirements is accounted for. This calculation is a 'worst case' consideration as for the background statistics, the background has been extracted from an area with the same size as the source. The respective deadtimes resulting from AC vetoes reduce these two count rates then equally by the deadtime fraction. In this study, the S/N ratio is calculated according to the following formula:

$$\text{signal/noise ratio } [\sigma] = \frac{(S + B) - B}{\sqrt{\sigma_{(S+B)}^2 + \sigma_B^2}} \quad (5.5)$$

S+B: Source_{on} count rate, B: Source_{off} count rate, $\sigma_{(S+B)}$: standard deviation of Source_{on} count rate, σ_B : standard deviation of Source_{off} count rate

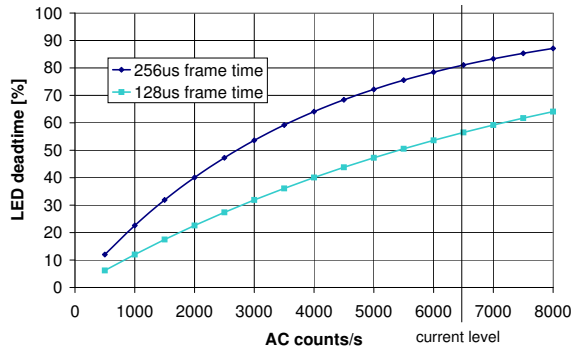


Figure 5.12: Calculated deadtime of the low energy detector at different AC count rates for 128 μs and 256 μs frame readout time.

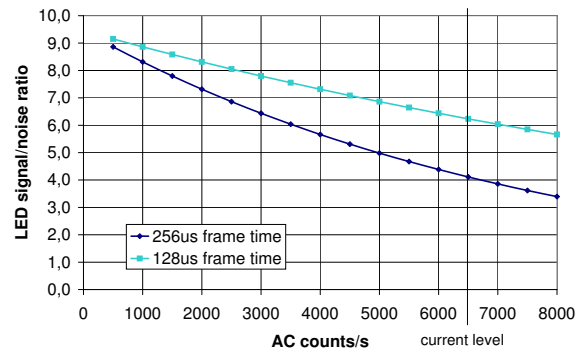


Figure 5.13: Calculated signal/noise ratio in the LED for a weak source at different AC count rates and for different readout times.

From these figures it becomes evident that a low deadtime and, therefore, a low AC count rate has to be achieved ultimately. As the simulated AC count rate with the current geometric model is above 6500 cts/s, it has become one of the critical items of the design to which special attention is paid.

Although it has been stated, that an active anticoincidence detector system for background reduction can not be implemented for a device with typical CCD integration and readout time cycles (~ 20 frames/s), because of the resulting high deadtime (Pfeffermann et al., 2004a), the SPST group has agreed, that in this case a deadtime of below 25% would be satisfactory and is, in the long run, achievable. Different approaches, introduced below, have been proposed to reduce the count rate.

A first attempt was made by simulating different AC trigger thresholds for the two detectors. However, when increasing the threshold, the AC effectivity drops significantly, so the gain in

sensitive time is paid for by a higher background (see Fig. 5.15). This is due to the spectral shape of the particle background that can be 'observed' at the location of e.g. the lateral AC group (see Fig. 5.14), which features a reasonable particle flux at high energies.

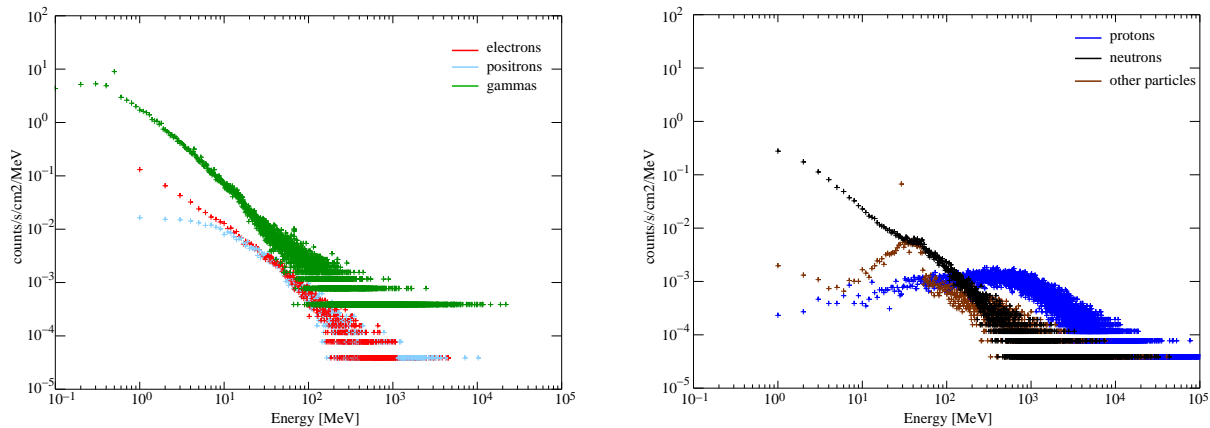


Figure 5.14: Proton induced secondary particle spectrum at the location of the lateral AC slabs separated in two plots for better viewing. Left: spectra of electrons, positrons and photons, right: protons, neutrons and heavy ions. Due to the shape of the incoming proton spectrum, the flux of high energy primary and secondary particles reaching the AC is still considerably high.

Another idea currently under study is to allow only the lateral and top part of the AC to contribute to the anticoincidence signal for the LED, or even to include the HED events into the trigger logic, leaving only those triggers, where the HED also shows an event. However, first simulation results suggest that simultaneous events in both detectors caused by the same primary proton are not as common as expected (<10% of background counts). That implies that a lot of background events would remain untagged when using this scheme. Also high energy photons from observed sources could in this case cause additional LED deadtime.

The most promising improvements for this issue are to be expected from reducing the exposure and readout cycle of the LED to shorter frame times. Although currently no shorter times are possible with the baseline readout ASICs¹, at least the 128 μ s should definitely be reached.

By building the AC geometry in a more compact way and closer to the detectors, the detection surface area can be further reduced. Thus, the same event tagging effectivity can be maintained, while the count rate scales down with the area, avoiding counts of particles that would only hit the AC but not the detectors. Following this recommendation, a new layout of the detector geometry was designed. It is reviewed in Section 5.3.9. The simulation group also studied the effects of attaching part of the graded shield to the *outside* of the AC, thus creating a kind of external shielding for the AC (see Sect. 5.3.8).

¹Application Specific Integrated Circuit

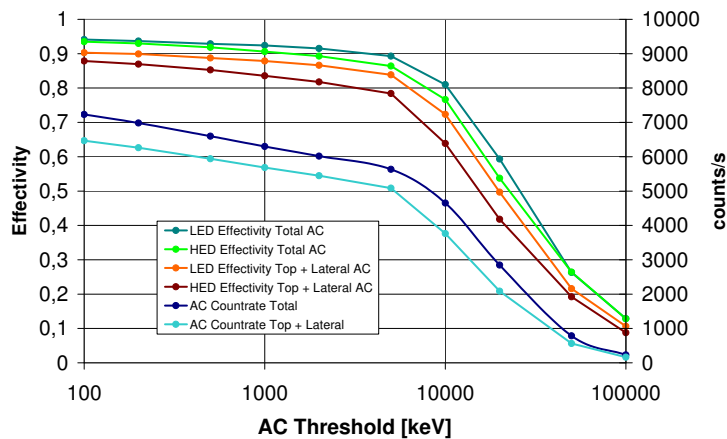


Figure 5.15: The AC effectiveness (left axis) and count rates (right axis) are plotted for both detectors as a function of the AC trigger threshold. The plotted curves illustrate the different rates for the whole AC and only the top and lateral part of it respectively. 'AC effectiveness' denotes the fraction of the total background events (induced by protons) in a detector that are tagged by the anticoincidence detector.

5.3.8 Further Results of the SPST Group

The correctness of the Simbol-X simulation environment has been cross-checked in many tests, conducted by R. Chipaux of CEA and C. Klose from the university of Darmstadt. After some initial discrepancies, the total background composition has been confirmed and agreed on after independent simulations in all three involved institutes.

A recent internal study by R. Chipaux regarding the particle emission sphere geometry proved as expected, that with larger emission spheres but constant inner sphere sizes and, therefore, smaller emission angles, the detector count rates stay the same (within statistics). Chipaux also investigated different AC materials to replace the plastic scintillators by crystals such as NaI, CsI or LaBr₃. However, this replacement leads to an increase of mass of material and consequently of the number of proton interactions and finally to a higher AC count rate (Chipaux et al., 2008). Studies with LaBr₃ and external shields around the AC are still in progress.

Further simulation results obtained by other members of the SPST Group have also partially been published already in the context of the first Simbol-X science workshop in Bologna (Chipaux et al., 2008). They include the background levels due to the activation induced in the spacecraft and in the detector materials by cosmic rays. These simulations were performed by C. Klose, who expanded the Simbol-X simulation environment by including also a module for treating radioactivity during his diploma thesis (Klose, 2007).

Another preliminary analysis of low energy 'soft' protons (500 keV), that are scattered in the mirror shells was conducted by A. Bulgarelli and L. Foschini. They found that with their generated statistics (10^6 protons generated in an annular source on top of the mirror shells with emission angle towards the detectors of ± 0.5 degrees) no proton or secondary reaches the HED (Chipaux et al., 2008).

5.3.9 Improvements of the Mission Design as a Consequence of Simulations

Although simulations were mostly used to estimate and verify the performance of certain components of the detector design, like e.g. the collimator or the detector box shielding, some important decisions for the design were based on their results, too. One of these concerned the location of the graded shield (GS) - inside or outside the AC material. While first considerations suggested to place it outside, in order to encompass and also shield the AC detector, reducing the count rate, simulations showed that high energy protons produce a lot of secondary particles in the graded shield, that *increase* the AC count rate instead, while the stopping power of the GS for low energy protons is rather poor.

Another simulation by R. Chipaux also confirmed these results by showing that when only the tantalum component of the GS is placed outside the AC as an external shielding, the proton background with AC *off* increases, while after tagged events are removed, the AC *on* background remains the same, which indicates also a higher AC count rate.

The idea of having separate AC trigger thresholds for the two detectors, to further reduce the AC count rate, originated from the results of the simulations shown in Fig. 5.15. As the effectivity of the AC is always higher for the LED, a higher threshold can be applied in order to have fewer counts at an effectivity comparable to the HED. As a far more effective way to reduce the AC count rate for the LED it has been considered to employ an anticoincidence scheme which uses only part of the total AC.

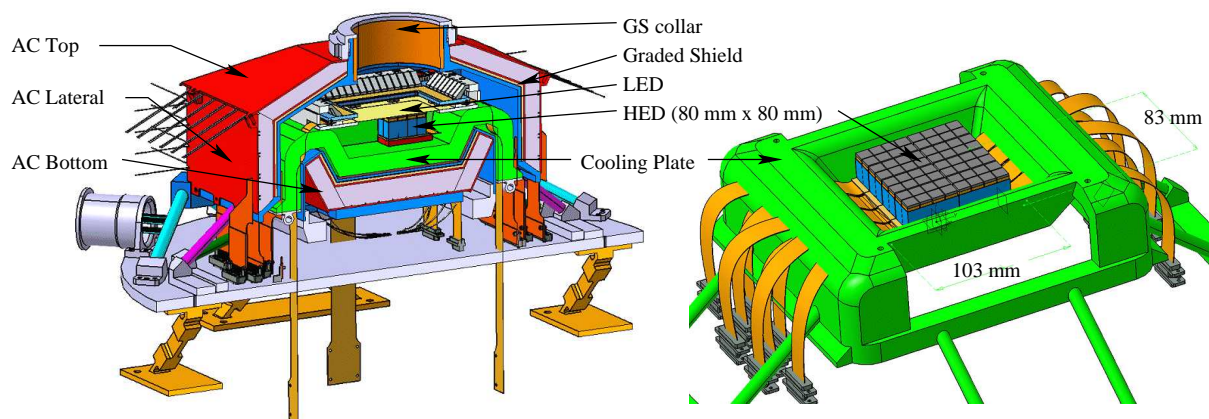


Figure 5.16: Updated drawings of the Simbol-X focal plane assembly. Left: section through the FPA, right: the HED and the aluminum cooling bed (images courtesy of CEA, Saclay).

Only recently, a new version of the focal plane layout has been designed and then re-created for simulations. This fourth geometry version has been optimized to address all of the issues detected with the simulation environment, most notably the large LED deadtime. Figure 5.16 shows the new layout. The AC is now much more compact around the detectors (outside di-

mensions: 288 mm \times 256 mm); in fact, the total surface area has been reduced from 0.311 m² to 0.214 m² by over 30 %. Besides the effect on the AC count rate, this allows also for more compact casing structures and a better compliance with the overall mass budget. In the new geometry, the AC detector has therefore less detection surface while maintaining the same detector coverage, therefore, the same effectivity. Furthermore, the segmentation of the three AC groups is now better adapted to the detector positions. Thus, in the new geometry, only its top part and possibly also the HED can be used for coincidence detection for the LED. Different AC thresholds have also been implemented: 300 keV for the HED and 1 MeV for the LED. All these improvements allowed to reach a current AC rate for the LED of \sim 3500 counts/s, corresponding to a deadtime of \sim 36 %, as shown in Figure 5.18.

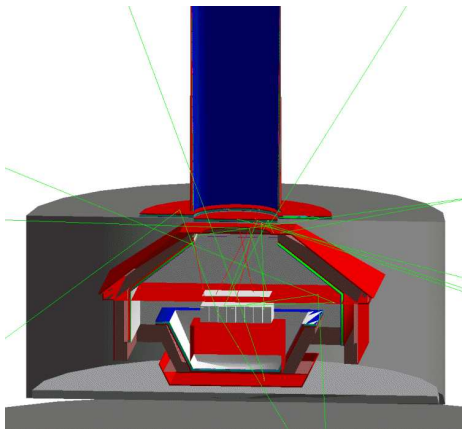


Figure 5.17: Snapshot from an ongoing simulation with CXB photons.

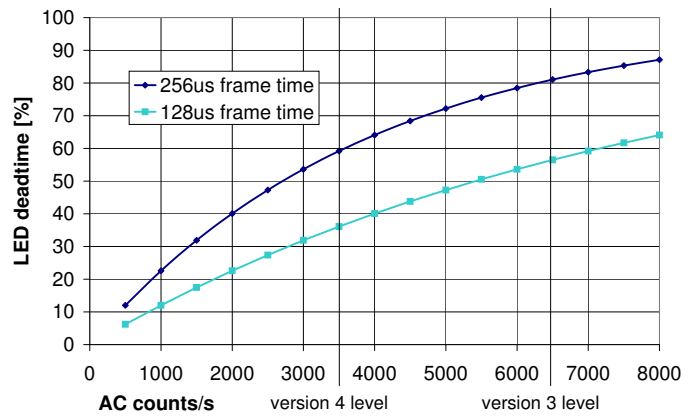


Figure 5.18: Calculated deadtime of the LED at different AC count rates and for different readout times.

Earlier simulation studies for the CXB induced background showed that almost all remaining background counts were due to high-energy CXB photons which can enter the FPA through scattering on the top (see Fig. 5.17). A collar of graded shield was eventually introduced on the top of the AC (see Fig. 5.16) to prevent these unwanted events. This helped to reduce the CXB component of the background by over 50 %.

The values for the total background, resulting from simulations with the new geometry are $(5.06 \pm 0.31) \cdot 10^{-4}$ cts \cdot cm⁻² \cdot s⁻¹ \cdot keV⁻¹ for the LED and $(8.37 \pm 0.24) \cdot 10^{-4}$ cts \cdot cm⁻² \cdot s⁻¹ \cdot keV⁻¹ for the HED. The background composition compared to the previous geometry versions is shown in Figure 5.22. These values are still above the requirements but those were originally derived for a near earth orbit and will be hard to achieve in a highly elliptical orbit. The impact on the sensitivity can be seen in Figure 5.20.

5.3.10 Simulated Observation of the Diffuse Cosmic X-ray Background Spectrum

With a simulation that is almost identical to the one performed to investigate the spectral shape of the instrument background, it is now possible to give a good estimate of the outcome of

an observation targeting the diffuse Cosmic X-ray Background. When the calibration wheel is turned to its 'open' state, and only the photons from the CXB macro are shot at the detector and finally the instrument background fraction is subtracted, the result will be the CXB as seen through the collimator alone (Fig. 5.19 left). Unfortunately, the geometric model does not yet include an adequate representation of the mirror spacecraft to also simulate X-ray focusing. However, this simulation can still be used as a prediction of the outcome of a measurement taken during the short period, where the mirror spacecraft is not in the detector's field of view. This interesting situation (Fig. 5.19 right) may arise whenever a satellite repointing is commanded in order to observe a new target. The procedure involves first the adjustment of the mirrors to the new observation angle and subsequently the movement of the detector spacecraft along a large radius, maintaining a constant distance to the mirror spacecraft, and finally its alignment to the new line of sight. As about one reorientation per day is foreseen during the mission, this might prove an excellent time for calibration tasks and background measurements.

The overall level of the flux in the spectrum depends, of course, on the field of view, restrained mainly by the length of the collimator. After background subtraction, a binning of 100 eV for the LED (HED: 1 keV) was applied to the resulting data from the simulation. More or less prominent lines can be identified in the spectrum at ~ 25 keV and ~ 8 keV. These are X-ray fluorescence lines from Sn and Cu, triggered at the edges of the graded shield, which are not covered completely in the simulation geometry. They are likely to be generated so dominantly only in the case of an open calibration wheel, where the inside of the FPA is exposed to direct radiation. The drop at the transition between the two spectra is following the diminishing quantum efficiency of the low energy detector where it becomes transparent at higher energies. The excess at the high end of the HED spectrum is due to higher energy photons that are scattered down to lower energies on interactions with the camera materials.

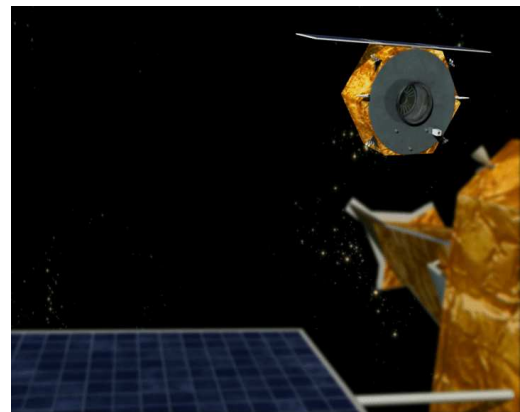
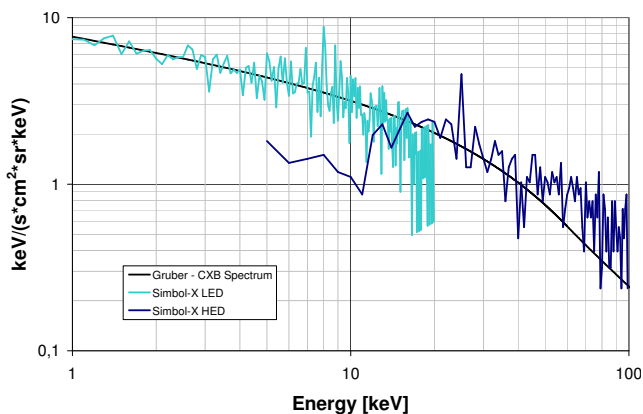


Figure 5.19: Spectrum of the diffuse CXB obtained in a simulated observation of the empty sky with no mirrors in front of the detector. Such a spectrum could be measured during one of the many repointings of Simbol-X (image courtesy of CNES).

5.3.11 Calculations Regarding the Sensitivity of Simbol-X

The Simbol-X top-level scientific requirements ask for a final on-axis sensitivity (3σ) of 10^{-14} $\text{erg} \cdot \text{s}^{-1} \cdot \text{cm}^{-2} \cdot \text{keV}^{-1}$ in the 10 - 40 keV range (for a 1 Ms observation of a source with a power law of $\Gamma=1.6$). With the results obtained from the above simulations it is now possible to give a substantiated estimation regarding this aspect. The minimum detectable flux with each detector in $\text{photons} \cdot \text{s}^{-1} \cdot \text{cm}^{-2} \cdot \text{keV}^{-1}$ is calculated according to Equation 1.7 from the introduction of this thesis with parameters that are detailed in the following. The results are plotted in Fig. 5.20. The required statistical significance of a detection (n_σ) was fixed at three sigma, the integration time T_{int} was set to 1 Ms, ΔE was $E/2$. The assumed area of the detection cell A_{det} is 0.03 cm^2 , encompassing a fraction of $\eta = 0.5$ of the source photons. The calculation was performed using the effective area of the telescope $A_{eff}(E)$ provided to the simulation group by G. Pareschi. The quantum efficiencies $\epsilon_{1,2}(E)$ are taken from the simulations in Section 5.3.2 and the overall estimated background flux in the two detectors, $B_{1,2}$, is that of the newest simulations.

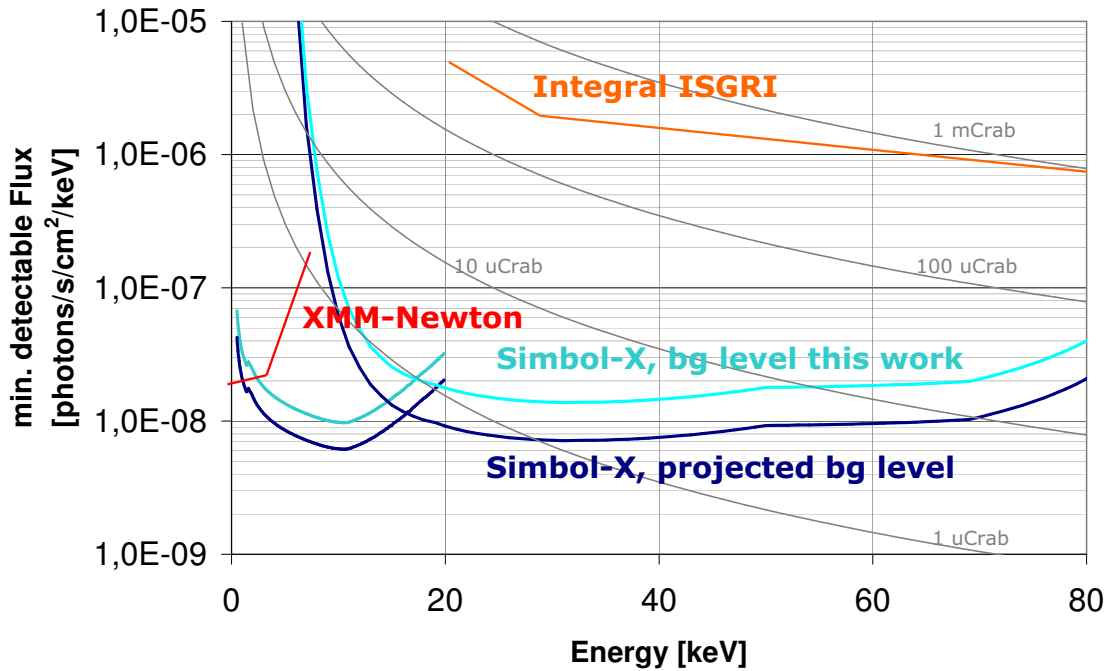


Figure 5.20: The minimum detectable flux, using the Simbol-X detectors. The curves are generated with the projected background level ($0.0002 \text{ counts} \cdot \text{s}^{-1} \cdot \text{cm}^{-2} \cdot \text{keV}^{-1}$) and the results obtained in this work. An observation time of 1 Ms was assumed. Detector deadtime is not accounted for. The approximate curves of the XMM-Newton pn-camera and the Integral ISGRI instrument are shown for comparison.

This usual form of presentation allows to compare the sensitivity to that of other instruments. From the data it is apparent, that Simbol-X will - with the present level of background - be about two orders of magnitude more sensitive in its nominal energy range than the currently

flown instrument ISGRI on board of the Integral satellite. The same is true for the Suzaku HXD and the SAX PDS that have a sensitivity only one or two times better than ISGRI. The level of flux sensitivity will be over the whole energy range around 10^{-8} photons \cdot s $^{-1}$ \cdot cm $^{-2}$ \cdot keV $^{-1}$, which is still a factor of two better than the NeXT Hard X-ray Imager.

In addition, this sensitivity can also be expressed in units of energy by a simple conversion, accounting for the respective photon energy. Plots of the converted data are shown for the LED and HED separately in Fig. 5.21, allowing the conclusion that the scientific requirements on sensitivity are more than fulfilled.

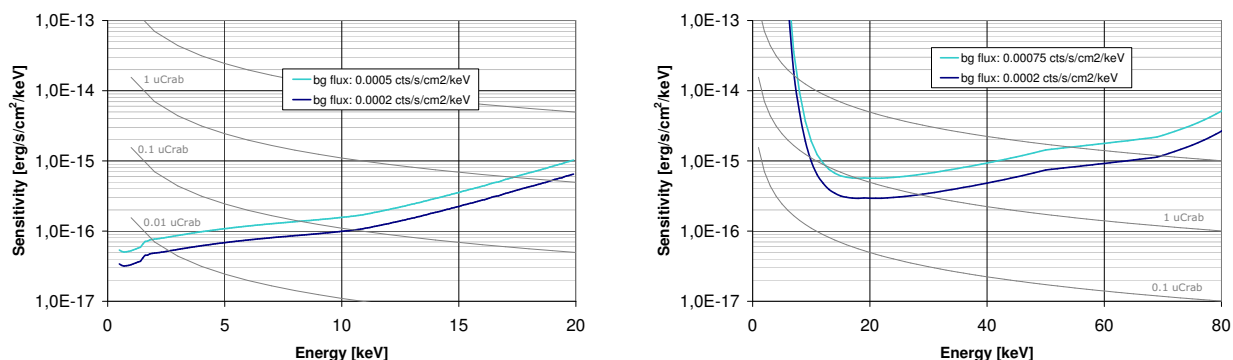


Figure 5.21: Estimated sensitivity for the LED (left) and HED (right) using the projected background (lower curve) and the background results from this work. An observation time of 1 Ms was assumed. Detector deadtime is not accounted for.

5.4 Discussion of the Results

In a kind of retrospective on the history of the simulation environment, it is interesting to observe how the predicted background changed over time with the evolution of the geometric model used in the simulations (see Fig. 5.22 and also Fig. 5.2). The comparison shown here was obtained in a re-simulation of the older geometries with the newest simulation environment. While the background due to the CXB photons remained roughly the same for all geometries, the proton induced background changed significantly. These differences can be mainly attributed to the modification of the AC detector geometry. While in versions one and two the AC had a larger total surface, resulting in about two times more AC counts/s than that of the current version, version two introduced an enhanced AC material thickness and was therefore able to detect protons up to higher energies with respect to version one. The implementation of the correct material composition of the HED detector electronics (replacing an assumed mix of Cu and Au) below the HED in the transition to the current version added also its small contribution to the background. Beginning with version three, a representation of the rest of the detector spacecraft was introduced and the detector geometry was made much more compact. Both measures resulted in more materials being actually placed closer to the detector. On interaction with the cosmic-ray protons, these materials act as strong sources of background. However, not only the geometry changed over time but also the physics processes that were taken into account. From

the first attempts with only electromagnetic interactions to today's complex physics and particle lists (*Tables A.3 and A.2 in the Annex*) with all kinds of hadronic interactions and radioactive decay, the Simbol-X environment has more than once undergone a complete renewal.

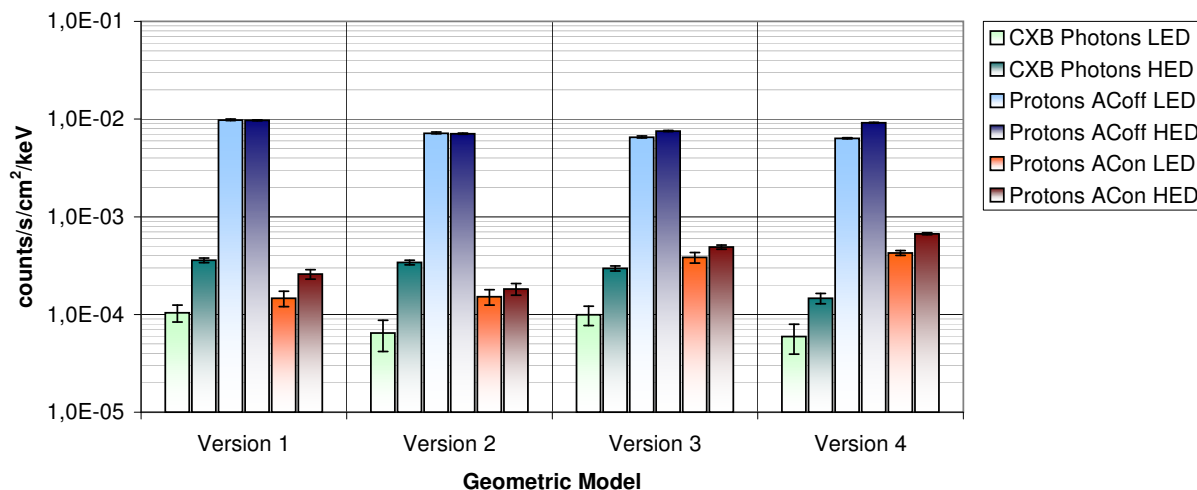


Figure 5.22: Comparison of the latest background composition to that of previous geometry versions.

The simulations presented in this chapter have highlighted all of the Simbol-X instrument design issues from a point of view concerned mostly with the background level and its composition. The results presented in the sections above and also the many smaller advancements that paved the sometimes rocky road for today's simulation environment were well received by the SPST group. Also other scientists involved in the field have shown interest and were appreciating them. As stated before, the simulations provided a valuable and solid basis to important decisions regarding the design of the mission. Furthermore, the simulations have shown, that an active anticoincidence detector around the two main detectors is absolutely required to achieve the requested low background.

With their accuracy, correctness and reliability now proved on several occasions, simulations performed within this simulation environment provide a unique opportunity to test and evaluate different geometries and detector concepts without having to carry out actual measurements on time-consuming and expensive prototypes.

The next steps will also include the addition of the mirror spacecraft to the geometry. With an environment that contains both satellites, the importance of focussed low energy protons can also be estimated with simulations. Ultimately, the mirrors will allow to simulate the normal observation of X-ray sources and the quality of the imaging in the presence of all kind of background. In a few years maybe, the outcome of scheduled observations (images and spectra) for Simbol-X can be simulated before they take place on the basis of an upgraded version of this environment.

Simulation and Measurement of X-ray Fluorescence Backlight from CdTe

X-ray fluorescence photons that are generated by materials in the focal plane assembly, close to a detector, have serious effects on the overall instrument background. Due to their origin, they affect the background only in particular areas of the detector and only in certain spectral regions, making it difficult to compensate for their effect on the scientific data. In the design of the Simbol-X focal plane, the prevention of detectable fluorescence photons is consequently a crucial objective. In Chapter 3 it was shown for the pn-camera of XMM-Newton that their intensity and distribution can be reproduced with the simulation environment. Simulations are therefore an effective tool for camera designers as they can help to reveal sources of fluorescence and to optimize the geometry in order to avoid or shield them.

However, the position of the Simbol-X High-Energy Detector (HED) and its associated read-out electronics must be directly below the Low-Energy Detector (LED) (see *Fig. 5.16*). Already early in the design phase it was therefore discussed how the fluorescence from the HED would influence the LED, if at all. A thin foil of yet undefined material is foreseen between the two detectors to absorb these fluorescence photons, but also to prevent electronic crosstalk between them. This is essential because of the high frequencies and voltages that are applied.

The results of an experiment that attempts to first simulate and then measure the influence of the HED onto the LED via X-ray fluorescence are presented in this chapter. The experiment aims to give an estimate on the intensity of these photons relative to the overall instrument background. It was prepared and performed in a vacuum testchamber at our institute. This setup is usually used to operate a small 64×64 pixel prototype of a DEPFET matrix detector for the wide field imager of the XEUS mission. Although constructed for measurements on photon pile-up and noise, it could easily be extended for the fluorescence measurement.

6.1 The Experimental Setup

The experimental setup is located inside an aluminum vacuum tank which features various flanges providing sealed access for cables and manipulators (see *Fig. 6.1, left*). Through the flange on top of the vacuum vessel, a coldfinger allows to connect the setup on the inside to a helium compressor cooling system on the outside. This coldfinger is connected via thick heat conducting copper wires to the copper cooling mask that encases the ceramics board carrying the DEPFET matrix (see *Fig. 6.1, right*). A constant temperature of $-40^\circ \pm 1^\circ$ can be maintained using a heater coil with adjustable power.

Cut-outs in the cooling mask at the position of the detector allow illumination with two ^{55}Fe sources. One of them is installed on the front side (side with the readout structure) and the other on the back side (photon entrance window) of the detector. The front side illumination is usually used for calibration purposes and noise measurements (see Section 6.1.1 below) but is in this case not of interest. On the back side an additional ^{241}Am source has recently been installed for this fluorescence experiment. This source and the ^{55}Fe source already present at this position can be switched on and off separately or jointly by means of a rotatable cover.

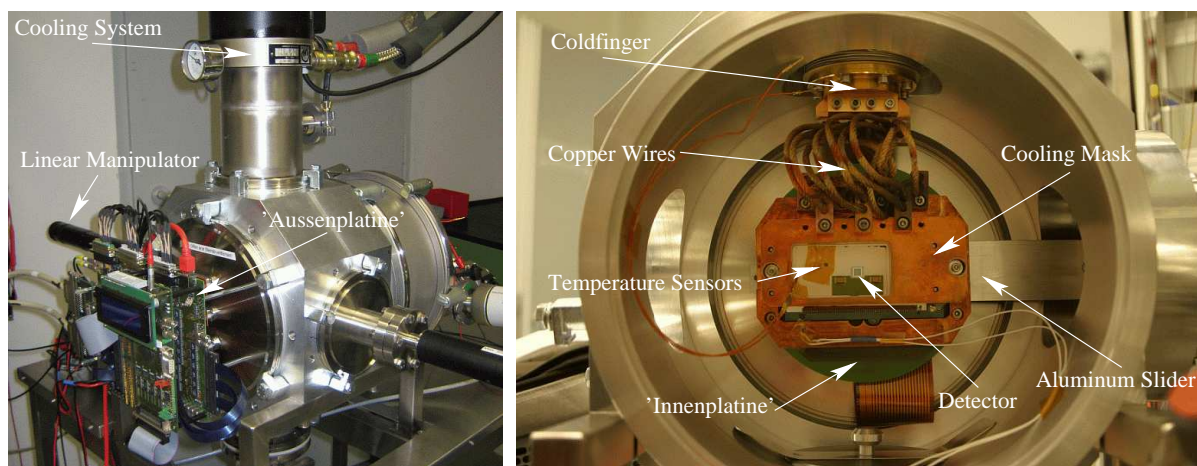


Figure 6.1: Lab setup for the measurement of the CdTe fluorescence lines as seen from the outside (left) and through the removed front from the source position (right). The photos in this section were taken by M. Martin who operates the lab setup at IAAT.

An aluminum slider, which is mounted onto a linear manipulator, is inserted behind the cooling mask at a distance of ~ 2.8 cm from the front side of the DEPFET matrix. With its help, the experimental setup can be easily altered from the outside. The slider can be moved in the horizontal direction and be arrested in three predefined positions. In this way, different materials can be positioned behind the detector. The first position is the plain 1 mm thick aluminum of the slider, the second has an additional layer of ceramics substrate, which is the same material that holds the detector and its surrounding electronics. The third position, however, is intended to simulate the Simbol-X case where the high energy detector is below the low energy detector. For this purpose, four CdTe crystals that were kindly provided by CEA, Saclay, are attached to the ceramics with a Kapton polyimide tape (see Fig. 6.2).

As the quantum efficiency of the DEPFET matrix is already negligible at the high energies of the photons from the ^{241}Am source (59.54 keV), it is transparent for this kind of radiation and they will pass right through it. When the source is turned on, background measurements with the detector in all three slider positions will thus show the fluorescence lines from the different materials behind the detector (along with the low-energy lines from ^{241}Am above 13 keV). The impact of the HED on the LED background can be estimated this way.

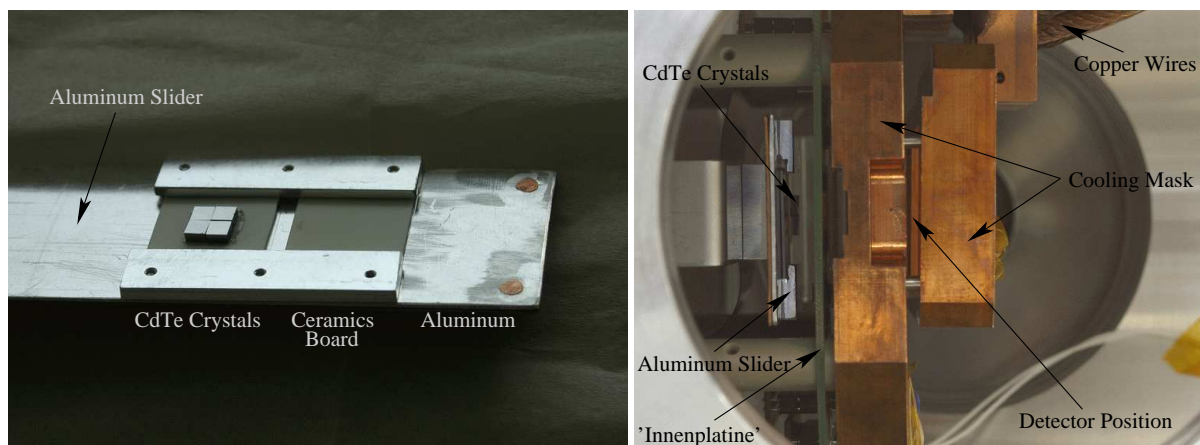


Figure 6.2: The aluminum slider holding the ceramics substrate and the four CdTe crystals (left). View of the assembled setup through a flange in the side (right): The ^{241}Am source is later positioned on the right from where it illuminates the cooling mask, detector and slider, which are seen edge on.

6.1.1 The DEPFET Active Pixel Sensor Matrix

The DEPFET matrix used in the lab setup is an array of DEPFET pixels (as introduced in Chapter 4 for the Simbol-X LED) that are integrated onto a monolithic silicon bulk with common back contact. In each row, the gate, clear and cleargate contacts of the individual pixels as well as the sources of all transistors within one column are connected. By applying the correct voltages to the common gate contacts of a single row using the switchers (see Fig. 6.3, left), it can be selected (turned on). The measured voltage changes on the source nodes then correspond to the number of trapped electrons in the internal gate of the currently active row (Treis et al., 2005).

This matrix prototype consists of 64×64 pixels with a size of $75 \times 75 \mu\text{m}^2$. In contrast to the Simbol-X LED, no drift rings are implemented around the transistors in this matrix. The total sensitive area amounts to $4.8 \times 4.8 \text{ mm}^2$ and is integrated on a $450 \mu\text{m}$ thick silicon bulk.

The spectral resolution at -40° (FWHM of the $^{55}\text{Mn-K}\alpha$ peak in the single-events spectrum) is about 130 eV. Due to the large thickness of the device and the small pixel size, the fraction of single events is reduced in back side illumination, making it difficult to collect a sufficient number of singles for gain determination. This is the reason why front side illumination results in a slightly better spectral resolution. It is also implemented in our lab setup, although the spectra for back side illumination with this kind of DEPFET matrix show a better peak-to-background ratio because the front side illumination background is dominated by partial events due to the structures on top (Treis et al., 2006).

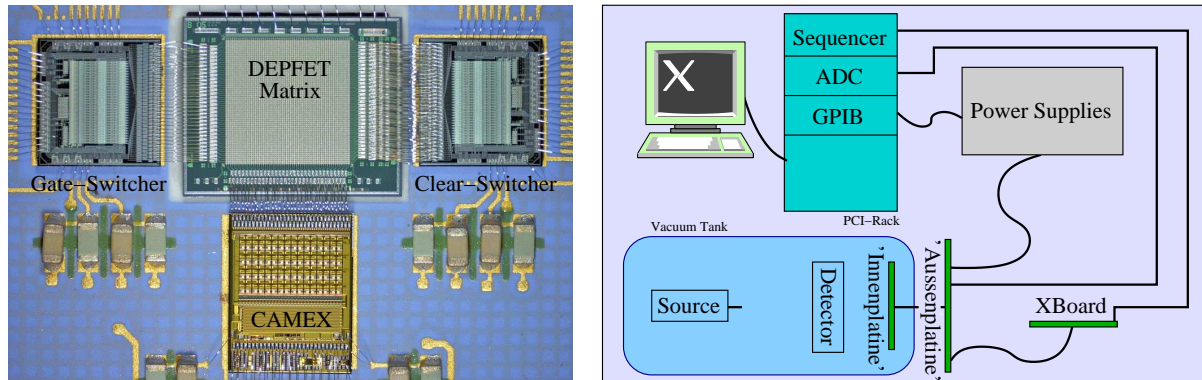


Figure 6.3: Close-up on the central area of the detector (left). The DEPFBET matrix and the ICs that are necessary for operation and readout are visible. A simplified functional block diagram of the lab system setup is shown on the right. The power supplies that provide the many different voltages necessary for the operation of the detector are computer controlled via a General Purpose Interface Bus (GPIB). The sequencer generates the digital control signals that configure and drive the switchers and the CAMEX via the FPGA on the XBoard. The Analog-to-Digital Converter (ADC) converts the CAMEX output into 14-bit values that are returned to and stored on the experiment computer.

6.1.2 The CdTe-Crystals

Four CdTe crystals are used in this experiment. They are positioned on top of the ceramics with Kapton tape on the aluminum slider as shown in Fig. 6.2. Each crystal is $4 \times 4 \times 2 \text{ mm}^3$ large and has a mean density of 5.85 g/cm^3 . They are totally unprocessed material samples, which means that there is yet no pixel structure on the surface of the crystals and no connection to the readout electronics below them.

All the $K\alpha$ and $K\beta$ fluorescence emission lines of Cd and Te are well above the upper detection threshold (which will be around 15 - 20 keV) of the Simbol-X LED. Thus, only the L-shell emission lines between 3.1 keV and 4.5 keV can be measured in this setup. A separate simulation has been performed with CdZnTe which was also an option for the HED material and the Zn- $K\alpha$ and $K\beta$ lines are well in range at 8.6 keV and 9.6 keV, respectively (see Table 6.1). Unfortunately, no prototype crystals of CdZnTe were available at the time of the measurements.

Table 6.1: Energies [eV] of selected X-ray emission lines (Bearden, 1967).

Element	$K\alpha_1$	$K\alpha_2$	$K\beta_1$	$L\alpha_1$	$L\alpha_2$	$L\beta_1$	$L\beta_2$	$L\gamma_1$
30 Zn	8,638	8,615	9,572	1,011	1,011	1,034	-	-
48 Cd	23,173	22,984	26,095	3,133	3,126	3,316	3,528	3,716
52 Te	27,472	27,201	30,995	3,769	3,758	4,029	4,301	4,570

6.1.3 X-ray Sources

Two radioactive sources, ^{55}Fe and ^{241}Am , are used in the experiment to illuminate the detector and to create the fluorescence emission from the materials. They are both located on the back side of the detector at a distance of 9.5 cm and can be activated individually by a rotation manipulator that allows to turn a shielding wheel positioned in front of the sources inside the vacuum setup. ^{241}Am has a half-life of 432.6 years and the source had at the time of measurement an activity of 2.84×10^6 Bq. ^{55}Fe has a much shorter half-life of 2.7 years and at the time of measurement, this source had an activity of 1.93×10^6 Bq. While the ^{55}Fe source produces a significant count rate above the background at the Mn- $K\alpha$ and K β energies, the detector is almost transparent to the high energy photons originating from the ^{241}Am source.

6.2 Simulation of the Experiment

For the simulation of the experiment, the same environment as for the XMM-Newton and Simbol-X simulations is used. Only the most crucial components of the setup have been included into the geometry for the simulation of the experiment. These components are described in more detail below and their arrangement can be seen in Figure 6.5. If switched on, the sources emit photons of a chosen energy in the direction of the DEPFET matrix. If the photons are not absorbed in the detector material, they interact with the materials on the slider behind the detector and can there be the source of fluorescence emission. All energy depositions on the detector are registered by the simulation with information about pixel coordinates, time and deposited energy.

Fluorescence yields for the K and L shells for the elements $5 \leq Z \leq 110$ are plotted in Fig. 6.4; the data are based on Krause, M. O. (1997). These yields represent the probability of a core hole in the respective shells being filled by a radiative process in the simulation. Auger processes are the only non-radiative processes competing with fluorescence for the K shell and L_3 subshell holes. For the filling of the L_1 and L_2 subshell holes, Auger and Coster-Kronig non-radiative processes compete with fluorescence (Kortright, 2001). Only one curve is presented for the three L subshells, representing the average of the L_1 , L_2 , and L_3 effective fluorescence yields. It can be noted from the plot that the fluorescence yields for the L-shells are generally much lower than those of the K-shells, which is important as only L-shell emission lines are produced from CdTe in the energy range of the DEPFET matrix, in contrast to the K-shell lines from zinc in CdZnTe.

6.2.1 The Geometric Model of the Experimental Setup

The geometric model used to simulate the experimental setup consists only of those components that are close to the detector and crucial for the experiment (see Fig. 6.5). A 450 μm thick silicon slab represents the DEPFET matrix, which is located on a 1 mm thick ceramics plate inside the 15 mm copper cooling mask. At a distance of 28 mm to the front side of the DEPFET matrix, the aluminum slider is represented by a 1 mm aluminum plate on top of 1 mm copper. The task of the copper in the real experiment is to shield the additional source included for

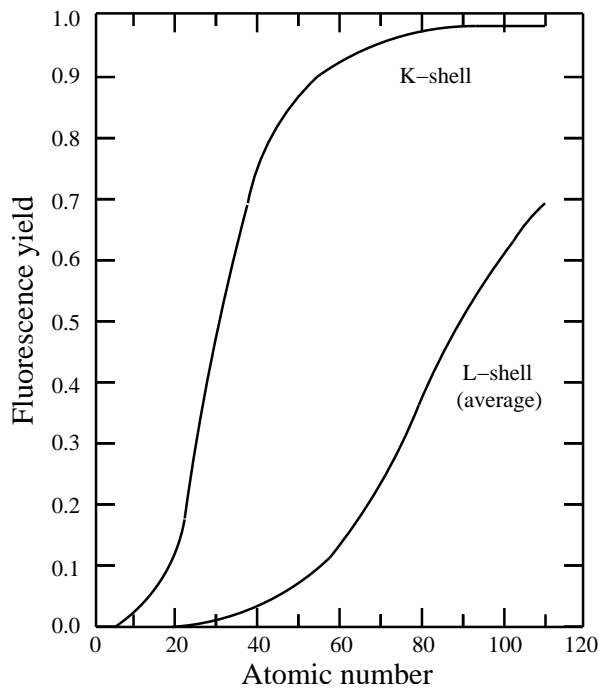


Figure 6.4: Fluorescence yields for K and L shells for $5 \leq Z \leq 110$. The plotted curve for the L shell represents an average of L_1 , L_2 , and L_3 effective yields (Krause, M. O., 1997).

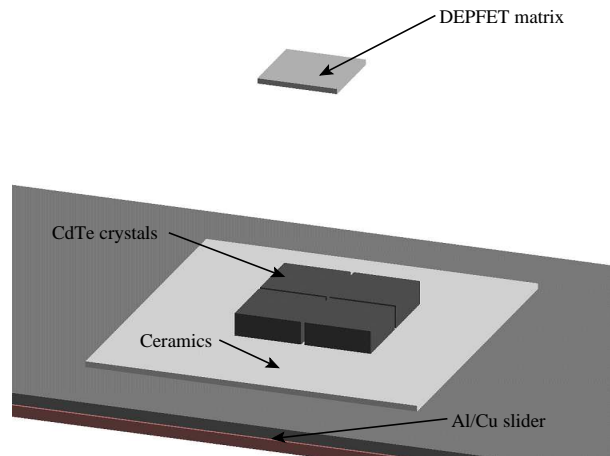


Figure 6.5: Simulation model of the X-ray fluorescence setup. The DEPFBET matrix is positioned above the aluminum slider, which carries the CdTe crystals. The ceramics board of the LED and the cooling mask are left out of the drawing to achieve more clarity.

front illumination if it is not used. Program parameters of the geometry code allow to switch the ceramics plate and the four HED crystals on and off, thus simulating the different slider positions. The material of the HED crystals can also be switched from CdTe to CdZnTe to simulate the fluorescence in both cases. The crystals themselves are positioned with 0.5 mm gaps to represent their actual alignment on the slider. Their location is also slightly offset with respect to the center of the LED in order not to have the beam center from the source coincide with a gap. Not included in the geometry are the vacuum tank itself, the necessary cables and supporting structures as well as the 'Innenplatine' printed-circuit board.

6.2.2 Simulation of the X-ray Sources

The radioactive sources in the simulation are purely virtual, i.e. they are not associated to any material in the geometry. Both are positioned at a distance of 9.5 cm from the back side of the DEPFBET matrix and emit photons into 2π (just as the real sources) with the center of the emission coinciding with the center of the matrix. The sources can be switched on and off individually, allowing to illuminate the setup with photons of different energies. The ^{241}Am source is simulated such as to imitate an activity of 2.84×10^6 Bq. With a probability of 35.9 %, it generates a photon with an energy of 59.541 keV, with a probability of 9.6 % a 13.946 keV photon and a 17.751 keV photon at 5.8 %. The other channels of decay are not simulated. The ^{55}Fe source has a simulated activity of 1.93×10^6 Bq, at this rate it emits with a probability of

8.5 % a photon with 5.888 keV (Mn-K α_2), with 16.9 % at 5.899 keV (Mn-K α_1) and with 3 % at 6.490 keV (Mn-K β_{1+3}). Also in this case, no other decay channels are simulated.

6.2.3 Data Generation and Storage

The only sensitive detector in this simulation is the silicon slab representing the DEPFET matrix. Whenever a photon undergoes an interaction within that volume, its deposited energy is registered and pixel coordinates are reconstructed from the position of the interactions. The elapsed simulation time, the energy and the coordinates are stored in arrays that are written into a FITS-file at the end of a simulation run. In this simple case of a photon emitting source, the elapsed time can be calculated from the generated number of primary photons via the activity of the source. After the simulation, the FITS-file is processed once more, whereas additional flags and information are supplemented in order to create an eventlist that matches the format of those returned by the *hllsas* software that is applied to process the measurements. In this way, both kind of data - simulated and measured - can be analyzed later on with the same IDL-routines.

6.2.4 Simulation Results

Six simulation runs have been performed in total (see Table 6.2), three with the ^{241}Am source and the other three with the ^{55}Fe source. For each source, the slider was set to the 'ceramics only' position in the first run, then in the 'CdTe' position and in the 'CdZnTe' position in the final run. An event-list was generated each time, containing the records of all energy deposited in interactions within the DEPFET matrix.

Table 6.2: Overview of the simulations performed for the X-ray fluorescence experiment.

No.	Slider Position	Source(s)	Duration
01	ceramics	^{55}Fe	754.571 ks
02	ceramics	^{241}Am	902.527 ks
03	CdTe	^{55}Fe	754.571 ks
04	CdTe	^{241}Am	902.527 ks
05	CdZnTe	^{55}Fe	754.571 ks
06	CdZnTe	^{241}Am	902.527 ks

The simulated duration amounted to 902 ks for simulations using the ^{241}Am source and to about 754 ks for those with the ^{55}Fe source. From the event-lists, spectra were generated by sorting the data in 10 eV bin histograms. Figure 6.6 shows the relevant region for fluorescence lines in the exemplary spectra from simulations #4 and #6. As can be observed clearly, the L α and L β lines from Cd and Te are generated by the code and detected at their respective energies (see also Table 6.1 above). The background continuum consists of the energies deposited in the DEPFET matrix by scattered photons. It can be subtracted later on with the help of simulations #1 and #2. The energy resolution of the detector is not simulated in the plots shown here.

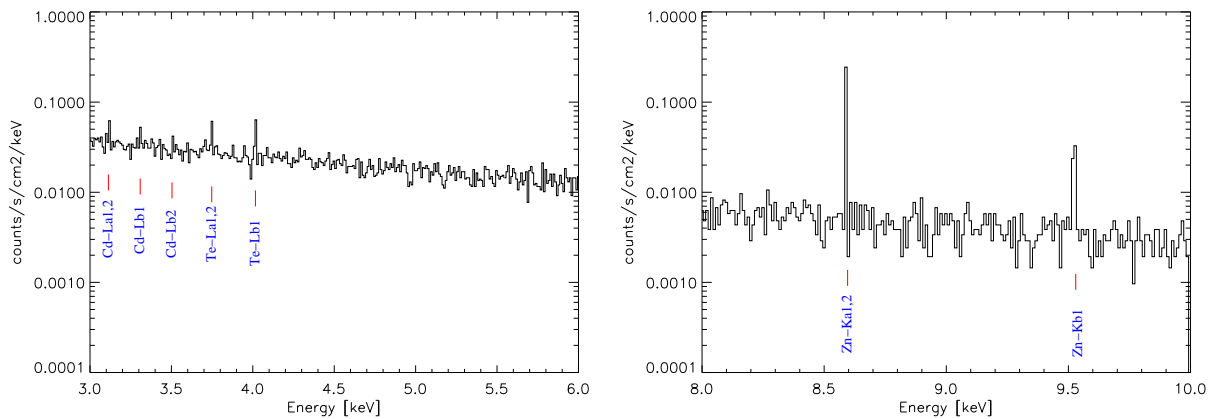


Figure 6.6: Spectra generated from the simulation runs #4 (left) and #6 (right) with the ^{241}Am source (linear energy scale). The plots show the relevant region for the expected fluorescence lines from Cd, Te and Zn. They can be identified above the continuum of scattered photons.

No spatial inhomogeneity of the events constituting the fluorescence lines could be found in the analysis. They are equally distributed among the pixels of the simulated matrix. It was originally assumed, that the arrangement of the CdTe crystals would be reflected in the distribution of the fluorescence photons. However, this is not the case due to the distance (26 mm) between the crystals and the matrix.

6.3 Description of the Measurements

The measured data described in this section were collected by M. Martin who operates the DEPFET matrix setup at IAAT with the experimental setup explained above. A total of ten datasets were obtained with different experimental configurations concerning the position of the slider and different source parameters. An overview of the measurements used in this analysis is presented in Table 6.3. Due to data storage limitations, the duration of a single measurement was limited to ~ 8 minutes; longer measurements could only be achieved by joining several datasets together.

Table 6.3: Overview of the measurements performed with the X-ray fluorescence experiment setup.

No.	Slider Position	Source(s)	Duration
02	empty (Al/Cu)	–	477.19 s
03	empty (Al/Cu)	^{55}Fe	475.07 s
04	empty (Al/Cu)	$^{241}\text{Am} + ^{55}\text{Fe}$	476.59 s
09	empty (Al/Cu)	^{241}Am	476.08 s
05	CdTe	–	477.19 s
06	CdTe	^{55}Fe	475.58 s
07	CdTe	$^{241}\text{Am} + ^{55}\text{Fe}$	476.08 s
08	CdTe	^{241}Am	478.14 s

Spectra between 0.2 keV and 20 keV of the measurements #3, #7 and #8 are plotted in Figure 6.7. A logarithmic bin size of 0.0396 (~ 252 bins/decade) is used. The different colors characterize events with different patterns. The grey area is the total flux on the detector *including also invalid events*. Selected spectral features that can be noticed in the three measurements are explained in the following.

In measurement #3, only the ^{55}Fe source was active and the slider was set to the empty (only Al/Cu) position. In the spectra of valid events (singles to quadruples) the Mn-K α and K β lines are clearly observable. Lines at twice their energies are detected in the spectrum from multiple events. These are generated when multiple photons hit adjacent pixels on the detector during the integration time of a single frame, thus generating *pattern pile-up*. The Si-Escape-Peak is visible around 4.16 keV. It corresponds to the energy of a detected Mn-K α photon minus 1.74 keV, which are lost due to an emitted silicon fluorescence photon.

During the measurement #7, both sources were active and the CdTe crystals were positioned behind the DEPFET matrix. In the resulting spectra, the Np-L α and L β lines from the americium source are detected at 13.7 - 14 keV and at around 17 keV, respectively, mostly in the double, triple and quadruple events. Fluorescence emission from the copper cooling mask can be detected at 8 keV, which is also prompted by the high energy photons from americium.

In measurement #8, the ^{55}Fe source is shielded by an aluminum cover in order to illuminate the setup only with the americium source. Obviously, either straylight photons from the ^{55}Fe source used for front illumination (which is only covered by the slider) still reach the detector or, more likely, fluorescence photons triggered on the vacuum casing (see Fig. 6.7, bottom). The lines are still clearly visible, though reduced by a factor of ~ 400 . Due to the finer resolution on the y-scale in this plot, the Cu-K β emission line from the cooling mask is also resolved at 8.9 keV. In this representation, however, no hints on the fluorescence emission from CdTe can be detected. A result, which can be attributed to the low statistics in the range of interest between 3 and 4.5 keV (see Section 6.4 below).

6.3.1 Data Selection and Processing

For further analysis of the measured data, the events of all measurements are filtered separately with the following criteria: PAT_NEVT-flag=1 (only single events) and STAT_TYPE=0 (no split-patterns, no pile-up, no out-of-time events, no MIP events, no partial, detector rim or re-emission events). The remaining events of each measurement are then used to generate spectra that can be compared against the results from the simulations.

6.4 Comparison Between Simulated and Measured Data

Figure 6.8 allows to compare the simulation result for CdTe to results from measurement #8 in the range of interest between 3 and 10 keV. An energy resolution of $\Delta E/E = 0.2$ has been assumed for the simulation of the line widths. A binsize of 10 eV is used for the simulated and 100 eV for the measured data. As the copper cooling mask has not been included in these

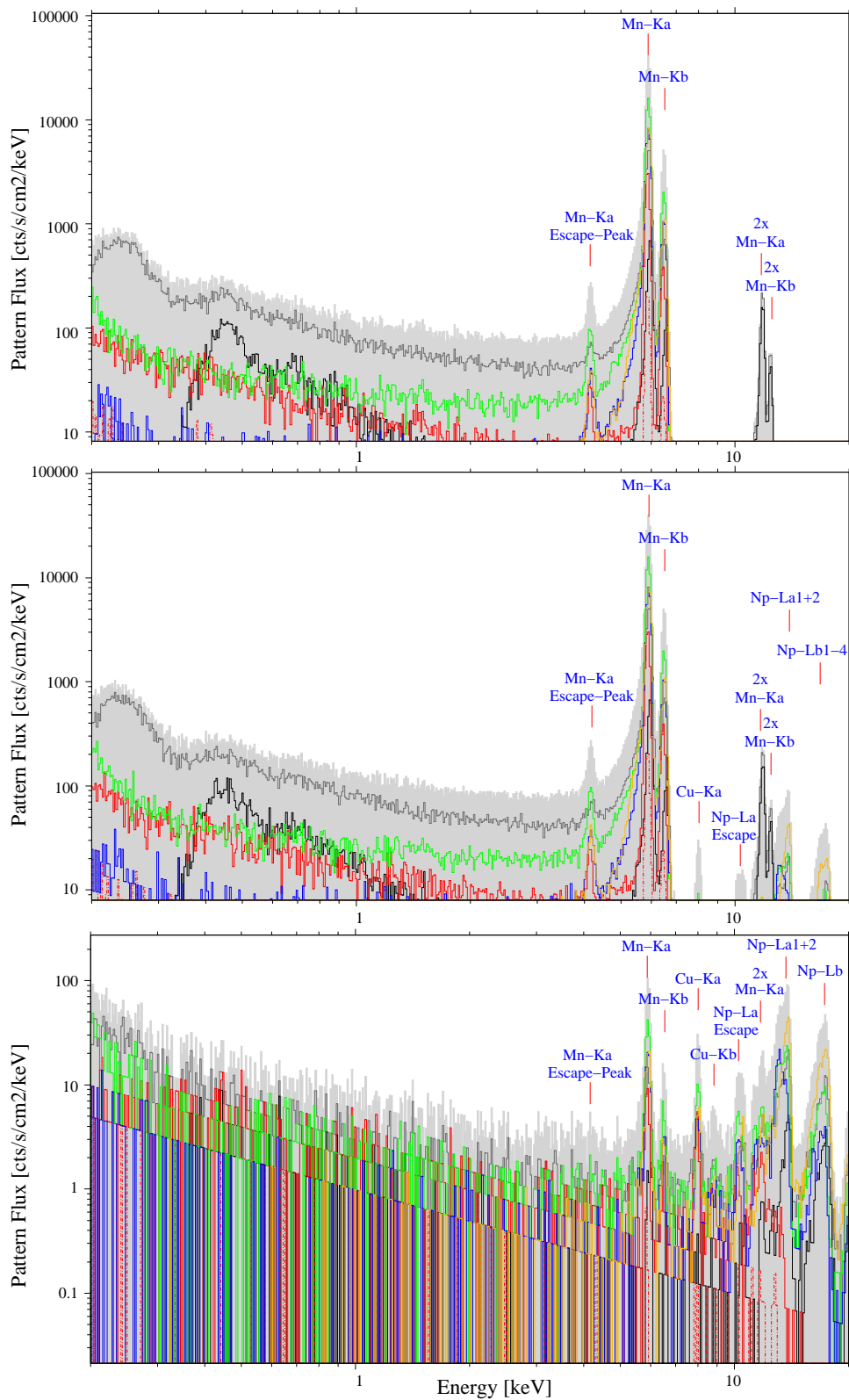


Figure 6.7: Pattern flux of fluorescence measurements (top to bottom) #3 (^{55}Fe on Al/Cu), #7 (^{241}Am and ^{55}Fe on CdTe) and #8 (^{241}Am on CdTe). Red: single events, green: doubles, blue: triples, yellow: quadruples, black: above quadruples, grey: invalid, light grey area: all.

particular simulations, the Cu-K α and the Cu-K β line can only be seen in the measured data. Furthermore, the not completely shielded Mn-K α and Mn-K β line are still visible, as was mentioned above. The background in the measurement is composed mainly from undetected split partners of split events from these Mn-Lines. This detector effect is not included in the simulations and has a strong impact on the experiment, given the weak intensity of the simulated lines.

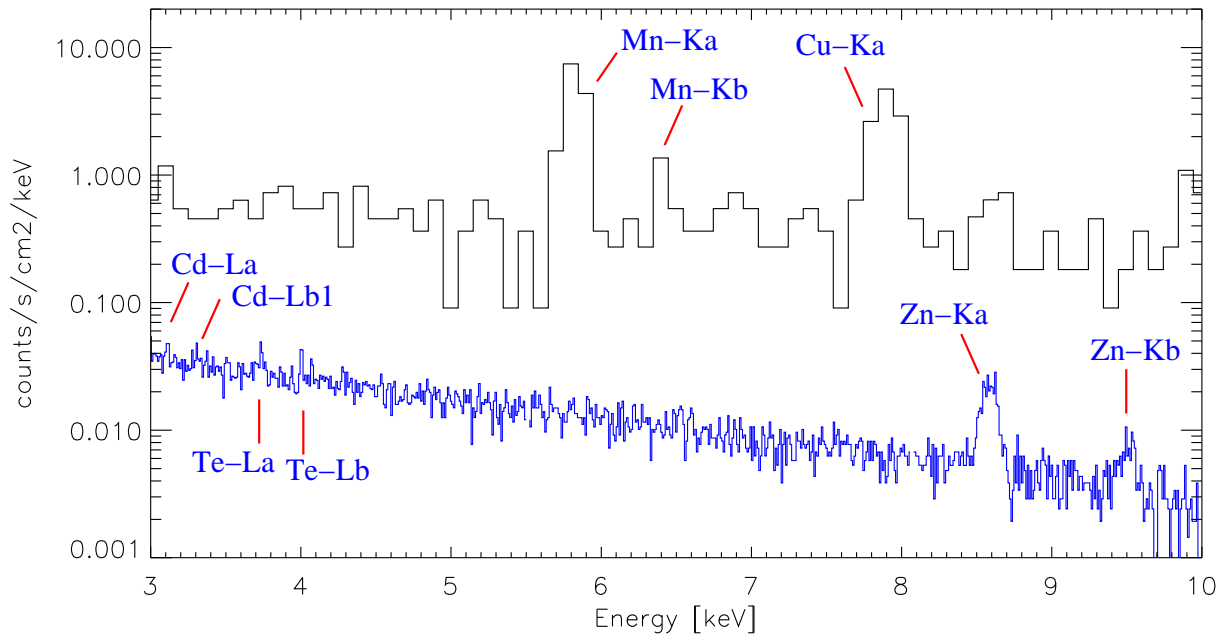


Figure 6.8: Direct comparison between spectra generated from simulation run #6 (blue) and measurement #8 (black) with the ^{241}Am source. The plot shows the region for the expected fluorescence lines. They can be identified in the simulations above the continuum of scattered photons ($a=\alpha$, $b=\beta$). The high background in the measured data is composed mainly of undetected split partners of split events from the not sufficiently shielded Mn-K lines.

The simulated spectrum shown here corresponds to a measurement of 902.5 ks, the measured data covers 478 s. From this plot, it can be calculated (using Equation 5.5) that at least an observation of 21 ks would have been necessary to detect the most prominent Cd-L α , Te-L α or the Te-L β_1 emission lines at their respective energies with a significance of 5σ above the measured continuum.

6.5 Discussion

For the next set of measurements, a different, vastly improved experimental setup will be used. In line with the progress of the Simbol-X phase B, a Science Verification Model (SVM) will be assembled at IAAT. The model will contain a working quadrant of the Simbol-X LED with correctly dimensioned pixels and one operational Caliste module of the HED with only 1 cm distance between the two detectors. It will be used to confirm their scientific performance and to collect for the first time experience with the two detectors working together in one camera.

With this setup, the fluorescence measurements can be repeated under much more realistic conditions. By then, also longer measurements and better shielding of the materials and sources inside the setup will be possible.

For future simulations, it is foreseen to integrate the radioactive decay module that is an add-on for the GEANT4 toolkit. It will then, hopefully, be easier to simulate the necessary radioactive sources.

The results from the simulations have shown that the respective intensity of the L-lines from Cd and Te is around 7×10^{-5} counts/s for the ^{241}Am source with an activity of 1154 Bq towards the solid angle containing the area of the DEPFET matrix. With the HED 1.6 cm closer to the LED in reality than in this experiment, this count rate will increase a bit more. As was reported in Chapter 3, the simulations for the pn-camera of XMM-Newton tended to underestimate the actual measured flux of the fluorescence lines. This effect, which will be investigated further, must also be taken into account here.

For scientific observations with Simbol-X, the contribution of these lines is, however, negligible as the sources observed are several orders of magnitude fainter than the radioactive source at energies above the peak of the LED quantum efficiency. As also an ^{241}Am source is foreseen on board of Simbol-X in the calibration wheel, one might be able to observe these lines in the calibration spectra, depending on the exposure time.

The Simbol-X Event-Preprocessor

In Chapter 5 it was shown that the Low Energy Detector (LED) of Simbol-X has to be read out with a very high rate (about 4000 Hz or 8000 Hz with double CAMEX readout) in order to avoid a large deadtime. However, each frame contains information about the energy (14 bit), the position (14 bit) and occasionally the time (32 bit) of every single one of its 16384 pixels - whether they are hit by a photon or not. Thus, a constant amount of $(14 + 14) \times 16,384 \times 8,000 = 3.670$ Gbit of information is generated by the LED every second - a rate that exceeds the capabilities of the telemetry or the foreseen data storage devices by far. In order to solve this problem, an on-board Event-Preprocessing chip (EPP) is introduced for each LED quadrant between the Analog-to-Digital Converter (ADC) output of the detector and the interface to the Event-Processing Electronics (EPE) of the spacecraft. Its purpose is to select only valid photon events by filtering the data with criteria explained in the following. This way (depending on the actual brightness of the sources in the FOV), only the few tens of desired events per second will be transmitted.

This chapter gives a functional description of the EPP, which is developed in collaboration with the electronics lab at IAAT. First results on the performance of the EPP are also presented. These were obtained with a testbench setup that was created in the course of this thesis and which simulates all necessary peripheral devices like the detector, the EPE and the sequencer.

7.1 LED Electronics Overview

The LED assembly (LEDA) consists of the four detector quadrants and their dedicated front-end electronics. Each quadrant is connected via bond wires to four ASICs: two first stage amplifier chips (CAMEX), that are connected to pairs of pixels from two lines, as well as the gate and clear switchers. Figure 7.1 shows a block diagram of the LEDA and its associated electronics. The 64 analogue values of pixel charges that are read out in parallel by a CAMEX are transmitted serially from the CAMEX to a 14 bit ADC. The emerging raw energy values are then further transmitted to the EPP, where several data corrections are applied and valid events (see *below*) will be identified and passed on. The output of each quadrant's EPP is in turn delivered to an interface controller (IFC), which has a serial (SpaceWire) connection to the EPE.

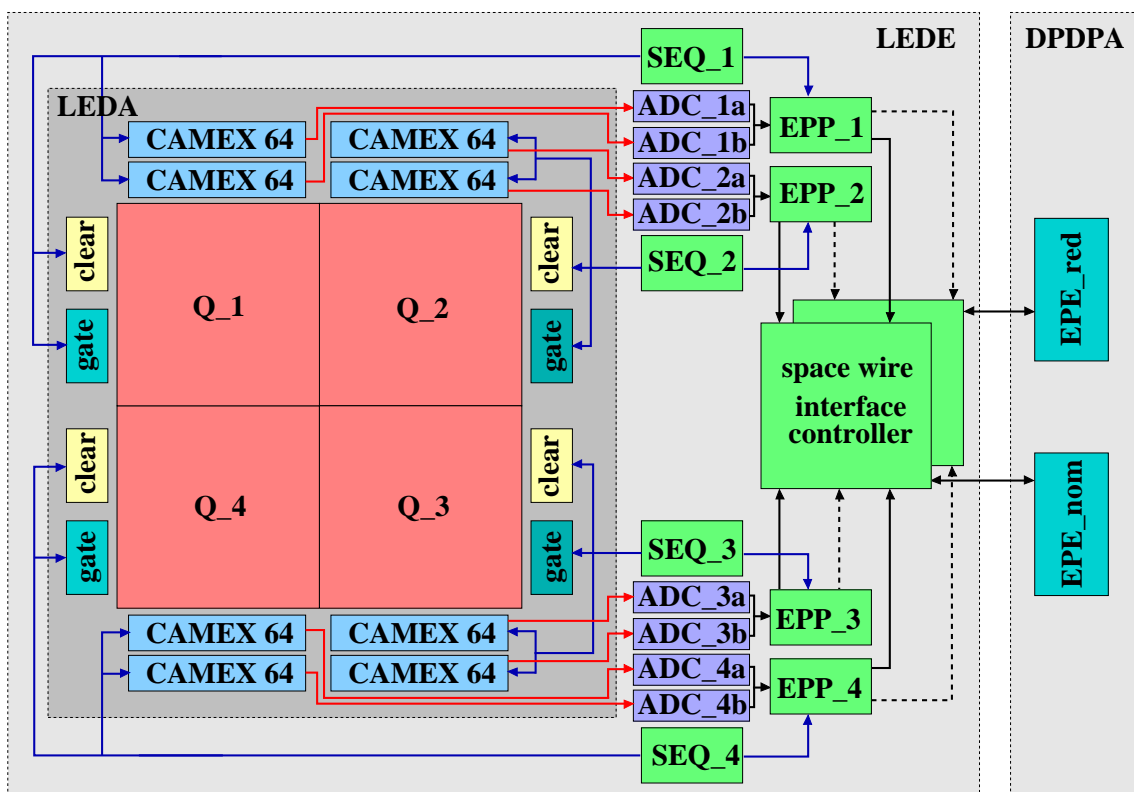


Figure 7.1: Functional block diagram of the Simbol-X low energy detector assembly (reproduction of a figure by E. Kendziorra). Surrounding the quadrants of the LED (Q1 - Q4) are the CAMEX amplifiers and the gate- and clear-switchers necessary for the selection, readout and clearing of one line. Each CAMEX needs its own ADC to digitize the data and each detector quadrant has a dedicated EPP and sequencer (SEQ) unit to operate independently of the others in case of a device failure.

7.2 Tasks of the Event-Preprocessor

The main task of the EPP is to correct the raw energies for common mode noise (see below) and also the dark current amplitude of each pixel (offset) has to be subtracted. The gain (conversion from number of electrons to ADU) for each pixel is slightly different, thus, each pixel amplitude has a different energy scale. Due to this fact, individual lower amplitude thresholds have to be applied to distinguish between signal and noise. Finally, invalid pixel patterns are filtered from the data.

The operations are performed in the following order:

- **offset correction**

An individual offset amplitude, which is afterwards subtracted, is determined for all pixels by the dark current generated during the integration time and further electronic offsets. A matrix containing these offset values for all pixels of a quadrant is called *offset map*.

The offset map can either be calculated on board from closed filter wheel observations or uploaded to the EPP from ground by command. The Most Significant Bit (MSB) of the map is used as an indicator to flag the pixel as bad (not to be processed further). This flagging is always done by commands from ground.

- **MIP/misfit rejection**

A minimum ionizing particle (MIP) usually creates a track of hit pixels in one frame corresponding to a projection of its incoming direction. The mean energy loss of MIPs is $1.5 \text{ MeV}\cdot\text{cm}^2/\text{g}$. Therefore, a MIP deposits in the LED at least 78 keV in one pixel ($450/2 \mu\text{m} \times 2.33 \text{ g}/\text{cm}^3 \text{ (density)} \times 1.5 \text{ MeV}\cdot\text{cm}^2/\text{g}$). As this is far above the energy range for photons to be measured ($\sim 20 \text{ keV}$), at least one pixel of a MIP track is typically above a high amplitude MIP-threshold or will have triggered the overflow flag of the ADC. These pixels and all adjacent pixels will be excluded from further processing. *Misfit* events occur when photons hit a certain pixel during the short readout time interval between signal sampling and baseline sampling. In this case the baseline will be higher than the signal, resulting in a negative value of the pixel amplitude. Such events can also be rejected or simply corrected.

- **common mode**

The amplifiers within the CAMEX are not compensated for changes in their own supply voltage. Thus, a small variation of the supply voltage will cause notable changes in the pixel amplitudes. As the 64 pixels of one line are converted simultaneously in parallel, the same supply voltage change is seen by all 64 channels, causing the same offset in all pixel amplitudes. This *common mode noise* can be effectively removed by the EPP with a filter, where the median value of all pixels of a line is subtracted from the pixel amplitudes.

- **valid pattern recognition**

Due to the widening of the charge cloud, electrons from one incoming photon are sometimes collected in more than one pixel, if the event occurred near a pixel border (so called *split events*). This occurs in about 35% of all events for the Simbol-X LED prototype and depends strongly on the pixel size and potential shape (*P. Lechner, priv. comm.*). The valid event patterns that can result from this process are shown in Fig. 7.3. Other connected pixel patterns are rejected by the EPP as invalid.

- **event filtering**

Only information from valid events will be passed on to the EPE for further transmission to ground. Valid events must meet all the following requirements:

- pixel has an amplitude above a lower threshold
- pixel is not flagged as bad
- pixel is not a MIP event, adjacent to a MIP event or a misfit event
- event has a valid pixel pattern

7.3 On Board Event-Preprocessing

The current design of the EPP is based on a pipeline concept inside an FPGA¹, which interconnects the digital output of the ADC with the input of the interface controller of the EPE. RAM memory holds the various lookup tables for the offset maps and thresholds. In the following, the details of the digital event-preprocessing (see also Figure 7.2) are explained.

7.3.1 Pixel Correction Unit

The output of the CAMEX analogue shift register is converted by a 14 bit ADC. These digital energy values for each pixel enter the EPP pipeline through a FIFO-buffer. They are first marked with their corresponding pixel coordinates and then pass on to the following units. Each processing step of the pipeline takes an amount of time $< 2 \mu\text{s}$ for a complete line of 64 pixels.

The pixel offsets are stored as 16 bit words in an external RAM. For each pixel, an individual offset is subtracted. A new offset table can be calculated from raw event amplitudes on board or uploaded from ground. The most significant bit of the offset table is used to flag pixels as bad. The MIP-flag is applied to those events that after the offset subtraction still have energies above the MIP-threshold and the misfit-flag, respectively, to those with energies below a certain misfit-threshold. All pixels then pass on to the common mode correction.

7.3.2 Common Mode Correction Unit

The common mode is corrected by subtracting from each pixel of a line the median of their energy values. In order to calculate the median, a whole line is accumulated within an internal register. Pixels with badpixel-, MIP- or misfit-flags are excluded from the median location. Finding the median with only the basic digital logic of an FPGA in the short available time-frame is quite a challenge and a special algorithm that avoids the usual sorting and rearranging of the energy values has been devised in cooperation with T. Schanz of IAAT for this purpose:

At the basis of the median algorithm is an array of 6-bit counters (the length of the array corresponding to the number n of not already excluded pixels in the respective line) that stores for each pixel the number of pixels in the same line with a larger (offset corrected) energy value. This array can be filled by having n comparators (one for each pixel) and multiplexing in n clock cycles through the line, thus changing the pixel compared to, increasing, as the case may be, the value of the counter. The median of the energy values is then the value whose counter registered $\text{floor}(n/2)$ larger values in the line. In the case when two or more pixel of one line hold the same energy value, such a value does not exist and the median value is then to be found at the position of the next smaller counter value. This recursive search can take another 32 clock cycles at maximum, when all pixels of the line have the same 64 valid energy values.

Finally, the correct median is subtracted from each pixel of the line and a constant value is added again in order to avoid negative values. This implementation of a fast median locating

¹Field Programmable Gate Array - a chip that can be configured with arbitrary digital logic

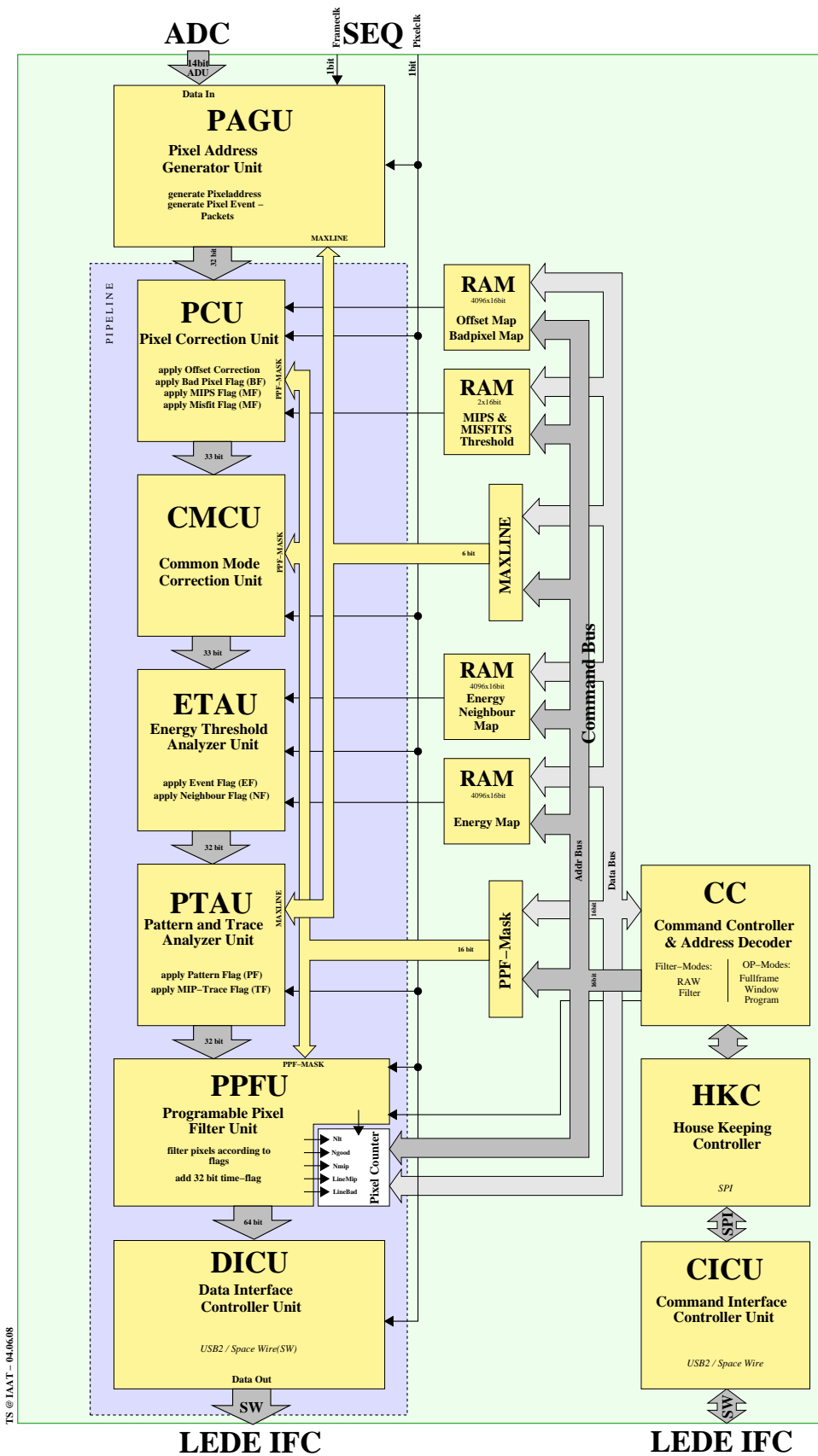


Figure 7.2: Functional block diagram of the Simbol-X Event-Preprocessor (T. Schanz)

algorithm in hardware will be presented at the SPIE¹ conference on astronomical telescopes and instrumentation in Marseille in June (Schanz et al., 2008).

7.3.3 Energy Threshold Analyzer Unit

Each pixel of the LED has its own preamplifier and all 64 pixels of a column are connected to an individual CAMEX channel. Thus, the conversion between raw amplitude in ADU and amplitude measured with a common scale in ADU must be done individually for each pixel. This correction of gain variation and the conversion into eV is not done on board, but has to be performed on ground.

Two different low energy thresholds are used to determine the occurrence of an event, whereas the MIP-threshold acts as an upper event threshold. The Lower Event Threshold Analysis flags all pixels with an energy above it as valid events, while the slightly lower Neighbour Pixel Threshold is only used in the pattern recognition, when an adjacent pixel is above the Lower Event Threshold. This method is applied to allow better identification of split partners that receive only a very small fraction of the total energy. Both thresholds are applied to all pixels at this stage and the respective flags are set. Both thresholds are also configurable individually for each pixel from ground.

7.3.4 Pattern and Trace Analyzing Unit

In this unit, as in the Common Mode Correction Unit, the EPP analyzes more than one pixel at a time. To perform its task of distinguishing valid from invalid pixel patterns, three complete detector lines have to be available inside an internal register. The algorithm then searches the middle line for pixels with one of the event flags set and checks their surrounding eight pixels for further events. As mentioned above, if the amplitude of a pixel is only above the Neighbour Pixel Threshold, but the pixel is adjacent to a pixel with energy above the Lower Event Threshold, the pixel is considered a split partner of that event. All valid patterns defined for the Simbol-X LED which are recognized by this unit are shown in Fig. 7.3. It can be seen that a valid pattern fulfills the requirement of fitting into a 2x2 grid with no further surrounding events. Therefore, all patterns that extend over three and more columns or lines are considered invalid. They can be flagged and later filtered by applying only logical operations on the event flags (EFs) of the relevant eight pixels:

$$\begin{aligned}
 \text{line analysis} &= (EF_{i-1,j-1} \vee EF_{i-1,j} \vee EF_{i-1,j+1}) \wedge (EF_{i+1,j-1} \vee EF_{i+1,j} \vee EF_{i+1,j+1}) \\
 \text{col. analysis} &= (EF_{i-1,j-1} \vee EF_{i,j-1} \vee EF_{i+1,j-1}) \wedge (EF_{i-1,j+1} \vee EF_{i,j+1} \vee EF_{i+1,j+1}) \\
 \text{invalid pat.} &= \text{line analysis} \vee \text{column analysis}
 \end{aligned} \tag{7.1}$$

i is the line number of the currently analyzed event and j is its column. The equation thus expresses that an otherwise valid pixel belongs to an invalid pattern, if the three closest pixels in the preceding and in the following line both have a valid event flag set (line analysis), or if the three closest pixels in the preceding and in the following column both have a valid event

¹The Society of Photo-Optical Instrumentation Engineers

(column analysis). With the help of this equation, the pattern recognition is reduced to pure logic evaluation for which an FPGA is perfectly suited and which can be accomplished in a single clock cycle.

The method applied in this stage to identify the valid patterns is significantly different from the commonly used method of comparing each pixel pattern with a library of valid patterns, using a DSP¹. It has also been co-invented by the author especially for the Simbol-X EPP chip and will be presented together with the common mode algorithm (Schanz et al., 2008). As the filter analysis is performed individually for each quadrant, some invalid events, which are located at the edge of a quadrant and spread over the quadrant boundaries, are also transmitted if they appear as valid events in the individual quadrants. Those events have to be filtered later on ground.

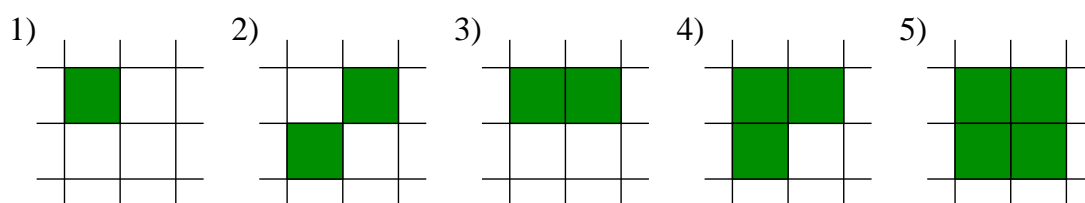


Figure 7.3: Valid pixel patterns recognized by the Simbol-X EPP: 1) single event, 2) two singles, 3) double, 4) triple, 5) quadruple event. The EPP is also able to recognize these patterns if they are rotated around the center of the depicted grids.

Valid pixels that are situated adjacent to a MIP pixel must also be flagged as MIP events, because they are most probably part of the MIP track or split partners of a MIP event. The majority of MIP tracks will be rejected by the pattern filter because they do not match any of the valid patterns. However, those that show equal patterns are in the case of containing one MIP flag event correctly flagged as a MIP pattern, indicating that the pattern is not a valid X-ray event but a MIP track.

7.3.5 Programmable Pixel Filter Unit

During the complete event-preprocessing procedure, the following flags, attributed to pixels, can be set:

- Bad Pixel Flag
- Misfit Flag
- MIP Flag
- Event Flag
- Neighbour Event Flag
- Invalid Pattern Flag

¹Digital Signal Processor

Events flagged as invalid can be filtered out at this stage and a timestamp is added to the valid data packets. In the normal operation mode, only pixel information from valid events will be transmitted to the EPE for further transmission to ground. Also, a few invalid patterns from the borders of the quadrants may leak through the event filter. This is acceptable as long as their contribution to the telemetry load is negligible. These events can later be rejected on ground. However, all valid event patterns have to be transmitted. As the pixel filter is programmable, it is an option to transmit also events that are properly flagged as invalid to the EPE (for statistical analysis or anticoincidence schemes).

7.3.6 Generation of Housekeeping Data

During event processing, several different event counters are used. Some are only needed internally within the EPP and some are also transmitted to ground. These can be used to check the correct behaviour of the EPP and to correct the transmitted event rate for dead time. It is today foreseen (but still preliminary) to count the number of pixels above their Lower Event Threshold, the number of good pixels transmitted to EPE and also the number of pixels rejected due to classification as MIPs.

7.4 EPP Testbench Environment

The Simbol-X EPP design has been developed in the hardware description language VHDL. The correctness of the design has been verified with a functional simulation. A synthesis for a Xilinx Virtex-IV FPGA has also been performed and a prototype has already been built. Equipped with a 100 MHz clock oscillator (which is in range of the allowed specs obtained from the synthesis results), the design will take $1.92 \mu\text{s}$ to process a line of 64 pixels. The currently FPGA based EPP is connected to three lab computers via three USB modules that allow to read and write data using a parallel bus interface. Each USB module is connected to a different computer, which all run the same testbench software. One of them is used to simulate the detector output, another one receives the output of the EPP. A laptop simulates the interface controller used to upload tables or telecommands (see Fig. 7.4 and 7.5).

The software, which has been developed in the frame of this thesis, provides the possibility to send simulated raw energy information of single pixels to the EPP and to receive the event packets returned by it on another computer. The original raw energy information can be edited by hand or read in from a prepared file. The software is able to display the output of the EPP again and allows some operations for analysis. It also allows to control the operation of the EPP by switching certain units on and off or uploading new tables (see Fig. 7.6). The whole testbench setup is stored in a 19" case that fits into a laboratory rack.

7.5 Results of the EPP Tests

With the EPP running in the lab setup and the testbench providing input data and receiving the processed events, a lot of tests - for functional verification and on long term stability - were accomplished. Unfortunately, the conversion to USB data packets and the maximum transfer rate

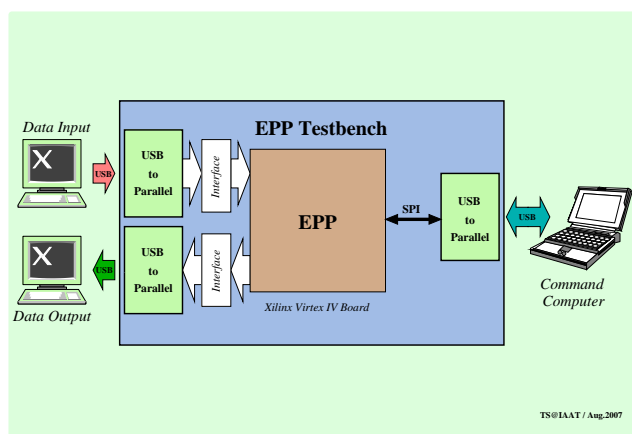


Figure 7.4: Block diagram of the EPP testbench setup. One computer simulates the detector output, the other one the interface to the EPE. A laptop is used to send the telecommands (T. Schanz).



Figure 7.5: The actual lab setup with the three computers and the EPP prototype in its case below the laptop (T. Schanz).

of the USB protocol is rather slow and cannot handle the necessary data throughput mentioned at the beginning of this chapter. Therefore, the data input of the EPP is now provided at only $\sim 0.1\%$ of the foreseen Simbol-X rate, but the EPP is still processing the arriving pixels with its designated speed of below $2 \mu\text{s}$ per line. For the time being, this is absolutely sufficient for the functional verification of the hardware EPP prototype.

The testbench software suite shown in Figure 7.6 consists of four windows: a master controller (bottom right), the input editor (left), the output console (top right) and the command controller (bottom middle). In the figure, the input editor window shows an input frame as it is typical for testing. The frame contains the logo of the IAAT, biased by all kinds of noise and distortion, which the detector or its readout electronics may produce. It can be sent to the EPP inside the Virtex-IV FPGA board by the data input computer. The EPP then processes the data and sends event packets to the data output computer. This output is finally visualized in the data output window of the output console. The frame is clean from any distortion, only valid data has passed the Event-Preprocessor.

The software not only generates and visualizes the test data, but also automatically compares input and output data frames to each other with the help of the 'compare quadrants' function in the user interface. This function allows to display and store all differences between two frames in a human readable file. The software is designed in a way, that raw frames from measurements with a real detector can also be sent to and processed by the EPP, allowing a comparison between the EPP and the software used by the HLL for event processing. However, this comparison has not yet been performed, while in the current version of the EPP all tests have shown that its mode of operation complies with all the requirements for the flight device given in the previous sections.

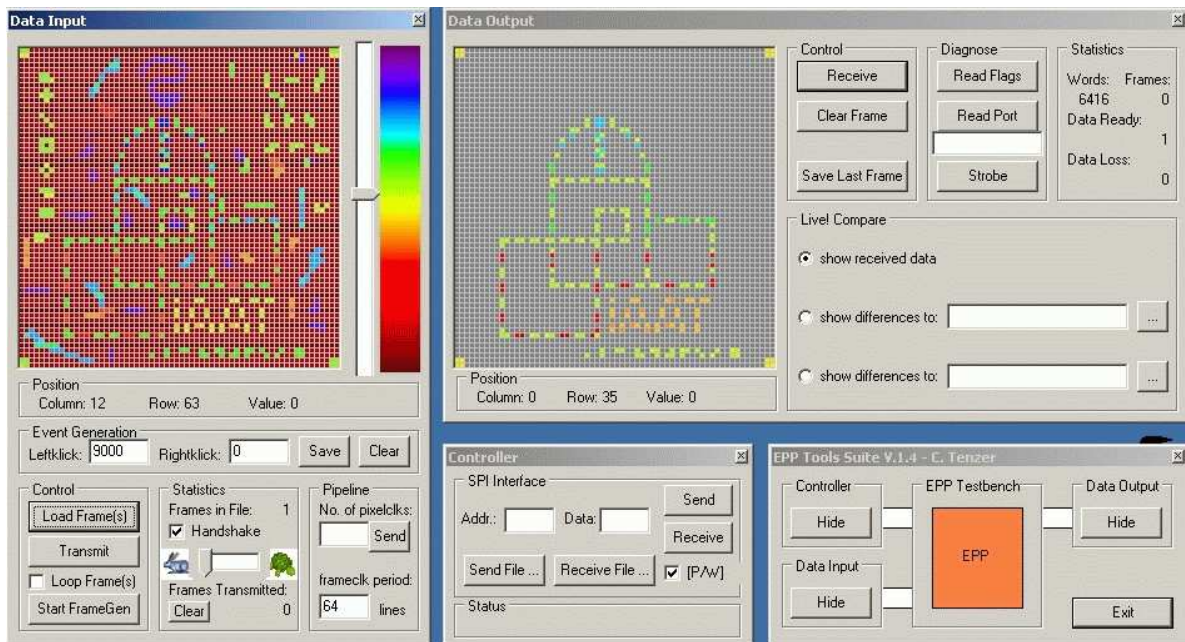


Figure 7.6: Screenshot of the in- and output of the running EPP testbench. The input data frame contains all sort of pixel structures including events above the MIP threshold and different common modes in various lines. These are all detected, flagged and filtered from the remaining 'scientific' data by the EPP, which is returned to the computer. Note that the data shown in this figure is not the least close to the data expected in orbit, where, depending on the source and background intensity, only very few frames contain a valid event at all.

In order to test the telecommand interface of the EPP, the software is equipped with a command controller window. This feature allows to send single commands and addresses to the telecommand interface of the EPP and can also process files containing batches of commands as is necessary for the upload of new tables. The EPP allows to control its modes of operation by these telecommands and its different modules can also be switched on and off. During the upload of a new offset table or threshold map, the EPP is put in a 'program'-mode where all incoming data is flagged as bad and thus no event packets are generated. This is done as a precaution to avoid processing one part of a frame with the old and the other with a new table.

Special effort was made to test the correctness of the implemented median calculation. For this purpose, a study was performed at our institute in order to compare the results of a software version of the median counting algorithm for randomly filled arrays to the *median* function of Perl¹ and to the sorting algorithm applied in the data processing of the EPIC pn-camera. Neither in this study nor in the tests with the running hardware device could any discrepancies from the expectations be found. Also, the precise application of the offset maps, individual thresholds and the effective functioning of the invalid pattern filter were confirmed.

¹Perl is a general-purpose programming language used for a wide range of tasks including system administration, web development, network programming, GUI development, etc.

To summarize, it can be noted that with the current version of the EPP hardware, the results of all tests turned out as projected and the EPP is now working as intended. The testbench environment was a vital part of the setup during the development and is absolutely necessary to perform all the required tests on the device.

7.6 Discussion and Outlook

As stated above, the testbench made efficient development and testing of the EPP for Simbol-X possible. On board event-preprocessing is definitely required to reduce the huge amount of data generated by the LED down to only few tens or hundreds of remaining event packets every second, depending, of course, on the sources in the field of view and the background strength. This considerably reduces the demands for the on board storage and telemetry capacities. In addition, the EPP plays an important role in background reduction, as invalid patterns and - more important - the MIP events created by particle interactions are flagged. The rate of such particle impacts was measured to be about $2.2 \text{ counts/s/cm}^2$ on the MOS cameras of XMM-Newton (Ferrando et al., 2003). Identification and removal of these events therefore lowers the overall instrument background significantly. Furthermore, counting and transmitting the rate of particle impacts with the housekeeping data, makes it possible to estimate the current local radiation environment. Collecting this information is not only constituting an intrinsically meritorious science investigation but can be valuable when judging the quality of the scientific data obtained in a certain interval. It can also be used as a trigger to close the calibration wheel in order to cover and protect the instruments when the impact rate is higher than a predefined threshold value.

The next step in line of verification will be the comparison of the processed data between the EPP and the software already in use at the HLL. However, both systems have been designed with common specifications to perform the same tasks - so no surprises are anticipated here. With the intention to run functional tests with the EPP at full input speed, another FPGA will be added to the testbench. This device can then be programmed at the usual slow rate via USB with a certain number of frames, whose pixels will then be transmitted repeatedly to the EPP at exactly the rate of the final ADC output. The output of the EPP will be buffered and then be transmitted via the foreseen SpaceWire interface to the testbench software. A detailed documentation of the EPP will be available after the testing stage has been completed.

During the development of the testbench it was noticed that a device which can simulate and reproduce the (already digitized) output of a detector is a very useful tool for the development of detector electronics or event analysis software. Current lab setups for detectors in X-ray astronomy require substantial machinery to generate a high vacuum and strong cooling. Of course, one of the rare detector prototypes must also be available. Hence, only few such setups exist and the available experiment time is limited. With a small, cheap and portable device that can generate the same output as the detector setup, electronics development for such detectors would become much simpler. The device could be programmed via a software user interface with the properties of multiple sources (position, spectrum, timing behaviour, etc.) and the rel-

evant detector parameters (number of pixels, response matrices, background, noise and readout cycle) and would finally generate the ADC output in an also configurable format. We are convinced that such a flexible *detector simulator* would be of interest for a lot of workgroups in this field. Mostly because of the fact that detectors and their event processing electronics are often developed in parallel - sometimes even at different institutes - and the time of testing both together is therefore always limited, while the definition of interfaces usually happens quite early in the progress. It is thus our aim to pursue this idea further in the near future, as it will also contribute to the successful completion of the EPP at our institute.

Simulations for eROSITA

The eROSITA (extended ROentgen Survey with an Imaging Telescope Array) instrument consists of seven individual co-aligned X-ray telescopes - each with its own camera and mirror module (see Fig. 8.1). Its launch is currently foreseen at the end of 2011 on board the Russian satellite Spectrum-RG together with the all-sky-monitor LOBSTER (GB), the high-energy telescope ART (Ru) and a high-resolution X-ray calorimeter. This chapter describes a simulation study on the expected background of the eROSITA cameras, depending on the selected orbit and time of launch. First results of this study have been presented at internal meetings and are taken into consideration for the selection of the not yet fixed orbit.

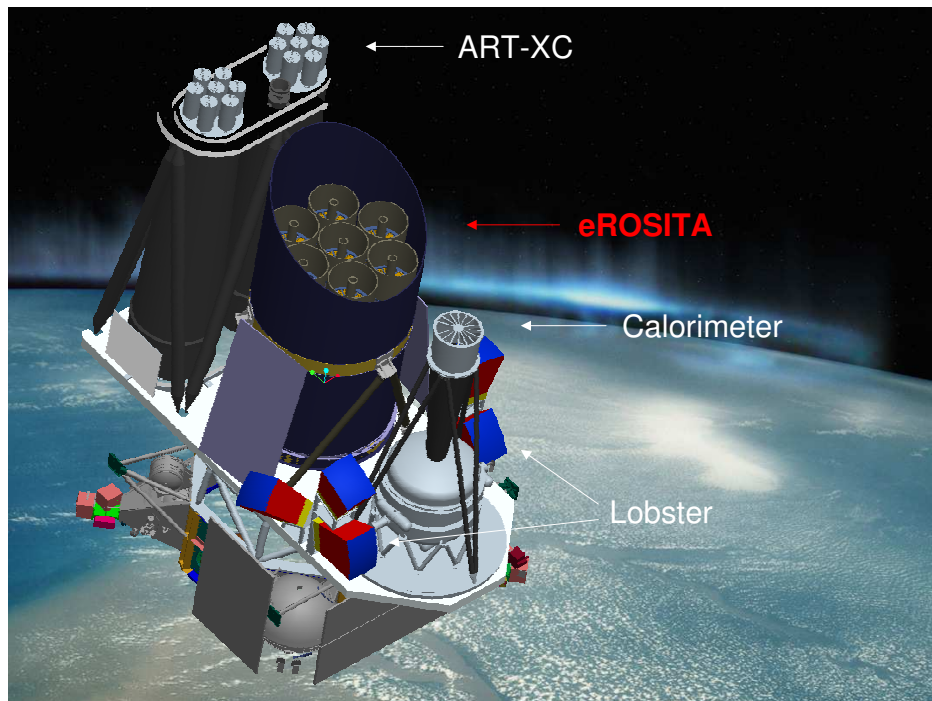


Figure 8.1: Artist's impression of the eROSITA instrument on board the Spectrum-RG mission (spacecraft drawing courtesy of MPE).

8.1 Introduction

The concept of eROSITA (Predehl et al., 2006), which consists of seven Wolter-I telescope modules, is an heritage from three previous projects: the German mission ABRIXAS (A Broadband Imaging X-ray All-Sky Survey), which failed in 1999 due to a malfunction in the power system, ROSITA, a telescope which was planned to be installed on the International Space Station ISS, and a proposal to NASA for the SMEX mission DUO (Dark Universe Observatory) that was based on a slight modification of the ROSITA telescope. The projected seven eROSITA cameras will each carry one frame store CCD detector (*see below*), which is a further step in technology derived from the pnCCDs of XMM-Newton. The number of shells in the mirror modules has been extended since the times of ABRIXAS by adding 27 shells on the outside, thereby increasing the collecting power with a total of 54 mirror shells by a factor of five at low energies. Ultimately, an angular on-axis resolution of the mirrors < 15 arcsec is necessary to meet the scientific requirements.

8.1.1 Scientific Goals of the eROSITA Mission

eROSITA will perform the first imaging all-sky survey in the medium energy X-ray range from 0.3 keV up to 12 keV with high sensitivity and an unprecedented spectral and angular resolution (*see Table 8.1*). Hence it will become possible to detect up to 100.000 galaxy clusters with a redshift from $z=0$ to 1.5. The sensitivity of this cluster survey in the 0.3 to 2 keV band will be about 4×10^{-14} erg/s/cm², which is an order of magnitude better than the ROSAT Survey, and it will be even deeper at the poles of the scan pattern. Multi-band optical surveys conducted preferably at the same time will provide the required photometric redshifts.

Because of their inherent properties, galaxy clusters are ideal to map out the large-scale structures in the Universe. They also provide information on cosmological parameters in different ways: The amplitude and shape of the cluster power spectrum and its variation with time as well as the cluster mass function in the local Universe depend sensitively on the density and distribution of Dark Matter and Dark Energy. Due to the acoustic oscillations at the time of matter recombination, the amplitude of primordial fluctuations in the matter power spectrum are still imprinted on the large scale distribution of clusters (Nichol, 2008). In addition, galaxy clusters can be used as cosmological standard candles to probe absolute distances, analogous to the use of supernovae type Ia (Allen et al., 2008). Progress in this field requires substantial, well-known samples of galaxy clusters, which eROSITA will provide in the future. They can be detected particularly in X-rays due to the radiation of the hot intracluster medium. A large sample size is necessary to determine the cluster mass function and power spectrum in such detail that it allows to follow the growth of structure with time.

The other main scientific goal is the systematical detection of all AGN and accreting Black Holes (including obscured ones) in the local Universe. Previous deep surveys in this range with Chandra and XMM-Newton and also with mid-infrared and sub-mm bolometers have shown that both, the cosmic star forming rate and the black hole feeding rate, are about two orders of magnitude lower today than they were in the early Universe (Brandt and Hasinger, 2005). This

decline of activity is not yet understood and many active black holes should be hidden in nearby galaxies, waiting to be detected by the survey.

Other science targets include the detection of ~ 600 Gamma-ray bursts (GRBs) over the four years of the all-sky survey. The scan geometry allows to observe every source in the sky every half year for ten seconds in each of ten consecutive orbits. With the planned sensitivity of eROSITA, GRB afterglows can be detected for up to two days after the burst. The exceptional event of the tidal disruption of a star that approaches a supermassive Black Hole also causes a bright flare in X-rays with a decay time of the order of years. The observation of large-scale diffuse emission profits from the high sensitivity and unlimited field of view of the survey but also from the excellent energy resolution of the frame store CCD. Due to the high read-out rates (20 frames/s), bright central sources in e.g. dust scattering halos that extend up to several degrees can be observed with less *pile-up*.

8.1.2 *The Spectrum-RG Observatory*

Spectrum-RG will be launched with a Soyuz-2 rocket from Baikonur, most likely into an ~ 580 km orbit with an inclination of around 29° (Pavlinky et al., 2006). But other orbits and even a placement in the second Lagrangian point (L2) are under discussion. A low earth equatorial orbit has been initially selected because of its low particle background. Since sources with low surface brightness and diffuse emission are studied (among others), it is important to keep the intrinsic background of the instruments as low as possible. Besides eROSITA, the satellite payload is currently composed of three other instruments (*Fig. 8.1*). Lobster, a wide field X-ray monitor, is developed by a UK-led consortium (Fraser et al., 2002). In the present design, it consists of six modules with a FOV of $22.5^\circ \times 162^\circ$, an angular resolution of $4'$ (FWHM), an energy range from 0.1 to 4.0 keV and an energy resolution of $\Delta E/E \sim 20\%$. ART, the Astronomical Roentgen Telescope supplied by IKI¹, had been proposed as an X-ray concentrator based on Kumakhov optics (Arefiev et al., 2006). However, the present design uses a system of multiple Wolter type-I mirror modules instead (O'Dell et al., 2008). For the Soft X-ray Calorimeter (SXC), which is developed by a collaboration between the USA, Japan and the Netherlands, a spare XRS detector from Suzaku with some modifications (larger area and improved resolution) is used. Significant improvement has been made since then in the optical blocking filters and the low energy response was strongly enhanced. Therefore, the SXC will collect 2-3 times more photons from diffuse sources than the Suzaku calorimeter (Mitsuda et al., 2008).

8.1.3 *The eROSITA Instrument*

The optical design of eROSITA consists of seven mirror modules, each containing 54 mirror shells with a diameter from 76 mm to 358 mm and a baffle in front of the mirrors. Their optical axes are co-aligned. Within the modules, both the mirrors and the baffle are adjusted and bonded to a spider wheel support structure. The mirror shells will be fabricated in the same process as those of XMM-Newton, by replication from super-polished mandrels with gold and electro-

¹IKI - Russian Space Research Institute

formed nickel. The advantages of having multiple modules instead of one large mirror are the smaller size of the mirror shells, which are therefore easier to produce and handle, a shorter focal length and reduced pile-up in the respective cameras for bright sources. A drawback of this concept is the higher background resulting from a larger detector area. The instrument will have a focal length of 1.6 m, a total length of 2.6 m (including baffles and cameras) and a diameter of 1.3 m. The effective area of eROSITA at 1.5 keV will be around 2500 cm² and is on average about twice that of XMM-Newton below 2 keV. Above this energy, however, it drops rapidly as a consequence of the small f-ratio (focal length vs aperture). Compared to ROSAT, the eROSITA sensitivity during the four year all-sky survey will be approximately 30 times better (Predehl et al., 2006). An overview of the instrument parameters of eROSITA is given in Table 8.1.

The CCDs that are used in the eROSITA cameras are improved versions of the pn-CCDs of XMM-Newton, which still provide excellent results after eight and a half years of operation. The CCDs now feature a fully depleted silicon bulk of 450 μm thickness, so the quantum efficiency is extended to even higher energies. By modification of the wafer processing the low energy response and resolution was also improved (Meidinger et al., 2006b). The pixel size was reduced to 75 μm to fit the resolution of the mirror modules. The most noticeable change, however, is the extension of the CCDs by a so-called *frame store* area, which allows a fast transfer of the generated charges from the exposed imaging area to the (shielded) storage area. From this area, the charges are read out at the usual, slower speed. This procedure drastically reduces the number of *out-of-time events*, i.e. unwanted photons which are recorded during the charge transfer and are therefore misplaced in the images along the shift direction.

Table 8.1: Overview of the eROSITA instrument parameters.

Parameter	Value
Energy range	0.2 keV - 12 keV
Energy resolution	< 130 eV @ Mn-K α
FOV (single telescope)	41.3'' \times 41.3''
FOV (total)	0.467 deg ²
Angular resolution	< 15'' on-axis
Number of mirror modules	7
Number of nested shells	54
Mirror coating	Au (> 50 nm)
Collecting area	2471 cm ² (7 modules @ 1.5 keV)
Exposure time per FOV	1342 s (in 4 years)

8.1.4 The Frame Store pnCCD-Camera

The frame store pnCCDs are developed by the MPI Semiconductor Laboratory (HLL) and profit from the institute's rich experience of the pnCCD development for XMM-Newton. They are im-

plemented on a $450\ \mu\text{m}$ thick monolithic wafer, which is fully depleted on operation. The name pnCCD refers to the fact that the three transfer registers of the pixels, the photon entrance window and the on-chip electronics are made of PN-diodes. The CCD chip designed for eROSITA is divided into 384×384 pixels. The pixel size of $75\ \mu\text{m} \times 75\ \mu\text{m}$ is matched to the angular resolution of the telescopes, which results in an image area of $28.8\ \text{mm} \times 28.8\ \text{mm}$. At the moment only 256×256 pixel prototypes are operated and considered in this simulation (see Fig. 8.2). After the exposure time, the image is transferred to the frame store area within $100\ \mu\text{s}$. This area contains the same number of pixels as the image area in order to store the complete image. However, the length of the pixels is shorter ($51\ \mu\text{m}$) to reduce the chip length. After the transfer, the image is read out in $5\ \text{ms}$ via two DUO CAMEX chips with 128 channels each, while the next image is integrated. With the foreseen additional integration time of $45\ \text{ms}$, which is also needed for the on-board event preprocessing, a time resolution of $50\ \text{ms}$, corresponding to a frame rate of $20\ \text{Hz}$, is achieved.

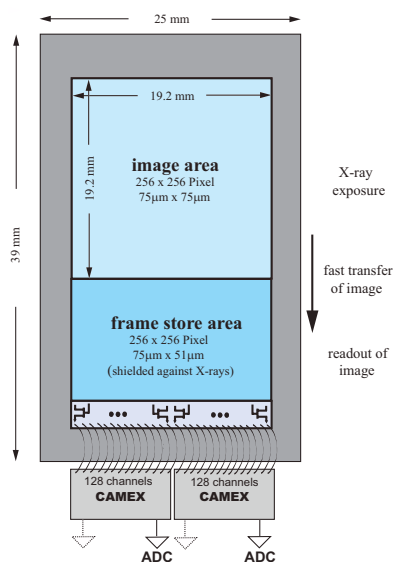


Figure 8.2: Geometry of the eROSITA prototype detector (N. Meidinger, MPE/HLL). The frame store pnCCD consists of an image area, the frame store area and the readout electronics. The device is glued to a multilayer aluminum oxide PCB with a cut-out for the photon entrance window on the back side.

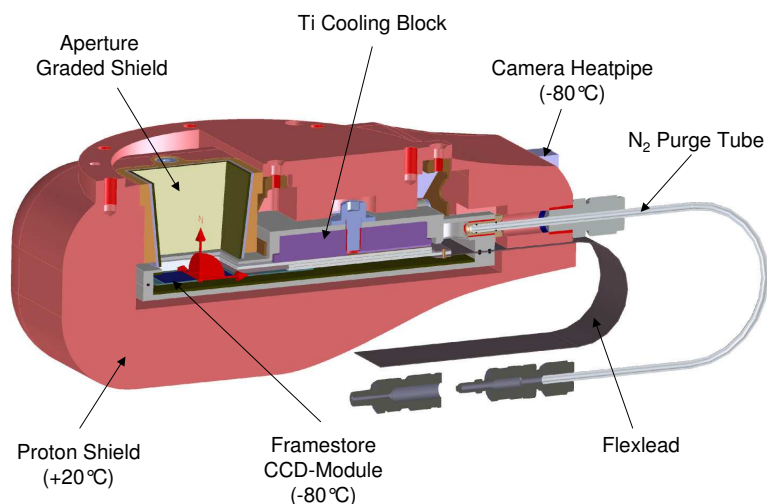


Figure 8.3: Cut-away drawing of one of the eROSITA camera heads (L. Tiedemann, MPE). A $30\ \text{mm}$ thick copper shield protects the CCD from high-energy protons. Only the image area is exposed to photons entering the camera through the aperture on top, the frame store area is shielded against X-rays.

In the spacecraft, the camera will be operated at a temperature of -80°C to reduce noise. Numerous performance tests were conducted at HLL for a 256×256 pixel prototype detector under eROSITA relevant conditions, i.e. frame store mode, cycle time of $50\ \text{ms}$, but at a temperature of only -60°C (Meidinger et al., 2006a). The energy resolution was analyzed for single events as well as for all event patterns. A shorter integration time or a lower operating temper-

ature lead to a slightly better energy resolution because of dark current minimization. Under these conditions, the energy resolution achievable in single event spectra has already reached the theoretical limit given by the Fano noise (125 eV at Mn-K α).

The design of the camera casing, which contains the CCD, is shown in Figure 8.3. A thick copper layer surrounds the interior and protects the CCD from damage caused by protons. On the inside of the proton shield is a graded Z-shield to stop the fluorescence photons from copper. Its composition is projected with a thickness of 1 mm aluminum and 0.5 mm boron carbide. The CCD is cooled via a titanium block which is in turn connected to variable conductance heatpipes (VCHPs). The heatpipes from each camera are redundantly coupled to a ring-shaped cooling system containing latent cold storage volumes and two large radiators. The complete telescope can be flushed on ground with nitrogen which is inserted at the back of the camera to keep the interior and mirrors free from dust and moisture.

8.2 *Details and Results of the Simulations*

This section describes the performed simulations for the eROSITA mission. Results on the camera background, which is due to interaction of trapped and cosmic-ray protons with the camera and spacecraft materials, are presented and discussed. Based on these results, a recommendation for the choice of orbit is given, with respect to a minimized camera background.

8.2.1 *Goals of the Simulations*

As described in the previous chapters, simulations that are performed with our simulation environment allow to estimate the level and spectral shape of the background inside an X-ray detector. For this purpose, the environment is supplemented with a geometric mass model of the detector and the camera. Furthermore, the radiation and particle environment present in the orbit of the satellite serve as an input for each simulation run. These particles interact with the materials of the mass model and create secondaries that sometimes register on the detector and create unwanted background events in addition to the 'scientific' events from sources. The background of such a camera therefore strongly depends on the environment in the orbit. The goal of these simulations for eROSITA is therefore to estimate the background level that is to be expected in the orbits/locations which are still considered possible for the Spectrum-RG satellite. These results can contribute to the final decision process.

8.2.2 *Simulation Geometry*

For the simulation of the expected eROSITA background, a rather simple approximation of the camera geometry is used by now. Figure 8.5 shows a cut-out of the design, where the CCD on the ceramics board is visible. In the simulation, the CCD is represented by a $30 \times 20 \times 0.45$ mm³ silicon slab. The ceramics PCB below is 20 mm wider on every side, 1 mm thick and has a cut-out of 20×20 mm below the CCD. The geometry of the proton- and graded-shield design is represented by concentric spheres, which completely surround the detector. A more detailed geometric model, close to the design in Fig. 8.3, is currently being implemented by the author.

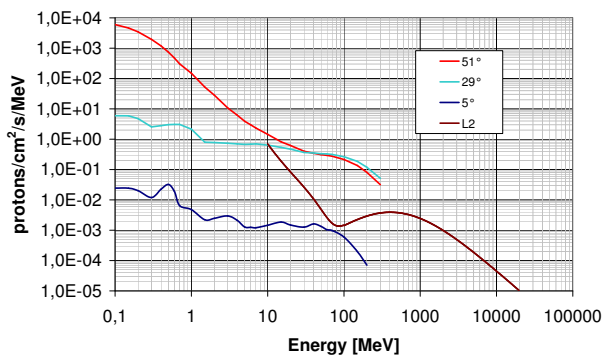


Figure 8.4: Proton spectra and fluxes used to simulate the eROSITA background for different orbit inclinations and the L2 position. The spectra are averaged over many of the respective orbits. They have been calculated with models of the OMERE software for the time of launch.

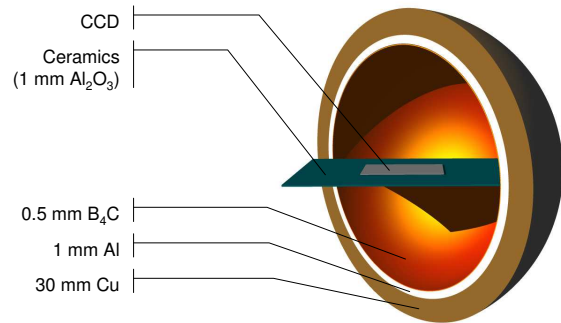


Figure 8.5: Cut-out of the simulation geometry for the eROSITA cameras. The 30 mm copper proton shield is covered on the inside by a graded shield made of 1 mm Al and 0.5 mm B₄C to stop fluorescence photons.

8.2.3 Incoming Particle Spectra and Fluxes

For the results presented here, only protons have been used as incoming particles. As has been shown in Chapter 3 for the case of XMM-Newton, they are responsible for most of the internal camera background. Figure 8.4 shows the calculated trapped proton flux at different energies for three circular orbits (altitude: 580 km) with different inclinations. Additionally, the cosmic proton flux for a hypothetical position of the satellite in the second Lagrangian point (L2) at a distance of 1,500,000 km to the earth is plotted. The calculations have been performed with the AP-8 (trapped protons) and CREME86 (cosmic-ray protons) models implemented in the OMERE 3.2 software for a launch date at the end of 2010. Besides the distance and the inclination, unfortunately no other properties of the L2 point are taken into account by these models.

While in the L2 only cosmic-ray protons are present, the near earth orbit environment is dominated by the particles trapped in the radiation belts. The cosmic-ray proton flux from the models in these orbits is below 10^{-5} protons/cm²/s/MeV in the energy range of interest and thus negligible. All data used and presented here are averaged over many orbits and thus include passages through the South Atlantic Anomaly (SAA). Only the orbit with an inclination of 5° avoids this region, which is the cause of the low average proton flux and consequently of the low detector background. The SAA is the region where the Earth's inner van Allen radiation belt is closest to the planet's surface (see Fig. 8.6 and 8.7). Thus, for any given near earth orbit altitude, the intensity of radiation is always greater within this region than elsewhere. Because of the tilt and offset of the Earth's magnetic axis to the rotational axis, the inner belt is closest to the Earth's surface over the south Atlantic, and furthest over the north Pacific.

The contribution to the background caused by interactions of trapped electrons (modelled with AE-8) with the camera has also been studied for the three mentioned orbit inclinations. It

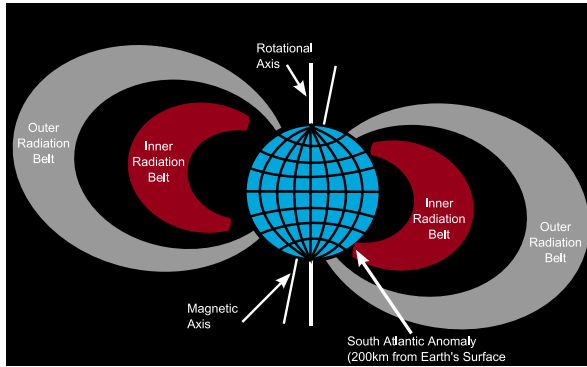


Figure 8.6: Schematic drawing of the Van Allen radiation belts indicating the location of the South Atlantic Anomaly.

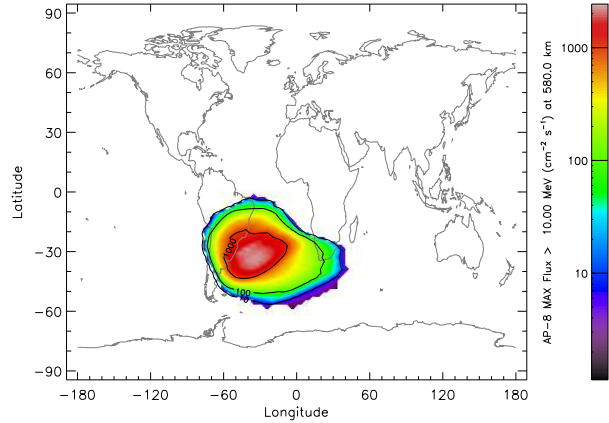


Figure 8.7: World map of the integral trapped proton flux above 10 MeV. The map has been calculated with SPENVIS² for mid 2010 and an altitude of 580 km. The strong influence of the South Atlantic Anomaly on the spacecraft environment is apparent.

was found to be below 20% of the proton induced background, so primary electrons were not included in further simulations.

As in the simulations for Simbol-X, the incoming particles are generated with equal distribution on the surface of a large sphere with a radius of 20 m. They are all emitted into a cone-shaped solid angle, encompassing the outermost sphere of the geometry. This way, an isotropic flux onto the camera is simulated and the simulation run-time can be obtained from the number of generated particles by using Equation 5.3.

8.2.4 Simulation Results

During all interactions that deposit energy in the detector, their time, location and deposited energy were registered at the time of the simulation run and were afterwards stored in a FITS-file. In the following analysis of the simulation output, spectra were composed for the different orbit inclinations. A range of interest between 0.3 keV and 20 keV and a binsize of 10 eV was selected. The results are shown in Figure 8.8.

While the orbits with an inclination of 29° and 51° show a background level of a few times 10^{-3} cts/cm²/s/keV over the whole energy range of eROSITA (0.2 keV to 12 keV), the background of the 5° orbit is two orders of magnitude lower. This outcome is obviously a direct consequence of the difference that already existed in the input proton fluxes (Fig. 8.4) for these orbits. The 5° orbit is not an option that is available for the eRosita mission. It was, however, selected for these background studies due to the fact that in this orbit a spacecraft is exposed almost to the same average proton flux as in an orbit with higher inclination outside the passages through the SAA. The fact that the 29° orbit has a higher flux than the 51° orbit, although the

integral proton flux is lower, can be understood by analyzing the properties of the proton shield (Fig. 8.9).

For this purpose, mono-energetic protons were fired again from all directions at the camera. While the event output of the detector was monitored, the proton energy was increased slowly. Above a certain energy, the detector began to register valid photon events from photons that were created in different processes upon interactions of the protons with the camera casing. The plot shows the probability of such a valid detector event as a function of the energy of the incoming proton. It becomes evident that protons with an energy below 235 MeV might in fact penetrate the proton shield, but only with an energy above that threshold they are able to produce valid detector events. From this it can be inferred that in this case only the high-energy parts of the input spectra are relevant for the generation of background events. Interestingly, the proton spectra in the two above-mentioned orbits change their intensity at about 40 MeV in such a way that the 51° orbit has the lower flux at higher energies. This is most probably due to the shorter passes of the satellite through the center of the SAA.

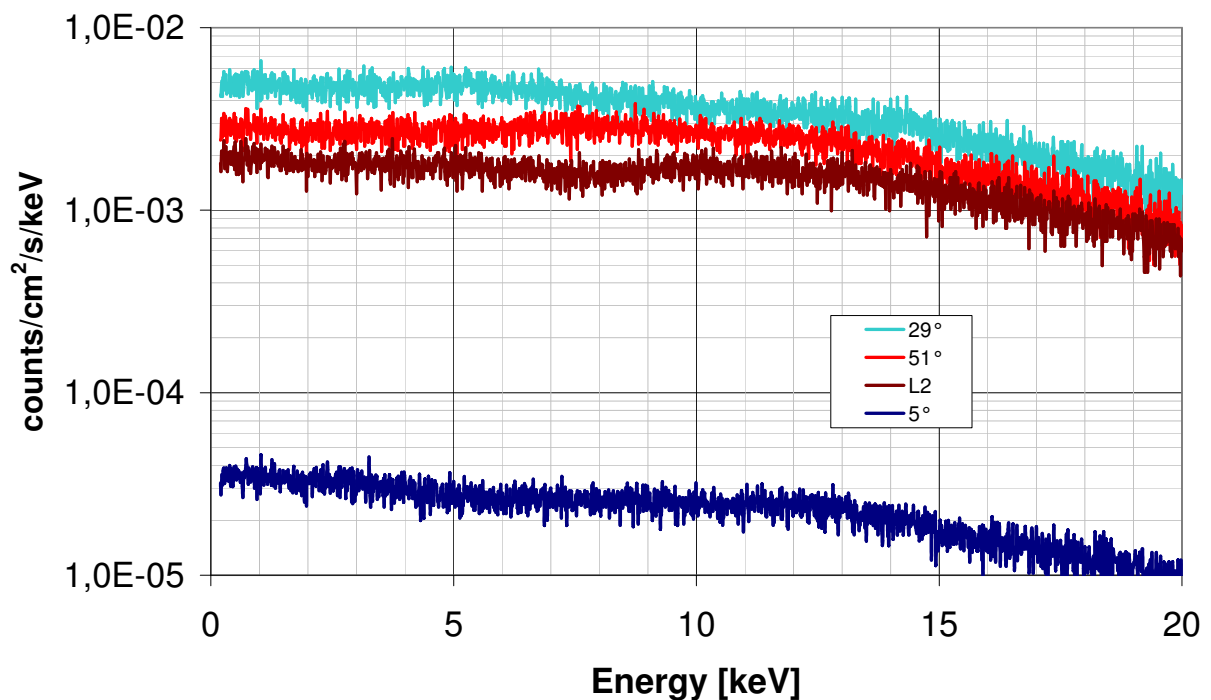


Figure 8.8: Simulated background spectra in the different orbits/locations. The 5° orbit shows by far the lowest background level as it does not include passages through the South Atlantic Anomaly.

The detector background that results of a position in the L2 point, which is only due to cosmic-ray protons, is slightly lower than that of the other two orbits. It is also important to note that it is constant over time in contrast to the fluctuating background level in a near earth orbit. No fluorescence lines can be detected in the spectra, at least with 5×10^7 simulated protons. The photons prompted in the copper are stopped within the graded shield, which leaves

only fluorescence photons from boron and carbon. These, however, have an energy below the detection threshold selected for the simulations.

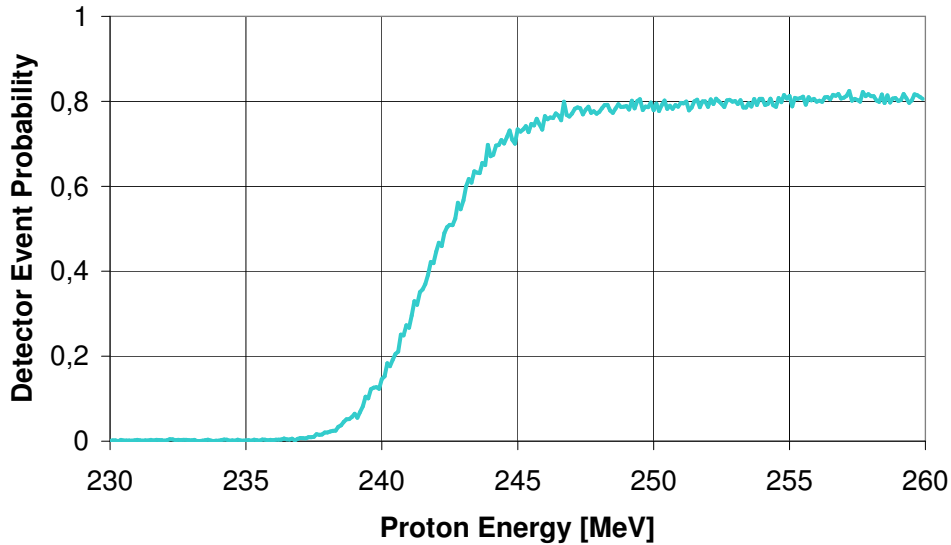


Figure 8.9: Probability of an eROSITA detector event as a function of incoming proton energy. Mono-energetic protons were shot at the simulation geometry. When the energy of the protons is increased, they start to penetrate the shielding and from a certain threshold value upwards, they also cause valid detector events via secondaries.

8.3 Discussion of the Results

As the 5° orbit completely avoids the SAA, the higher average flux and the resulting higher background in the other orbits are mainly attributed to the transitions through the radiation belts. Spectra for a few single partial orbits with high inclination that avoid the SAA completely, due to their selected phase, confirm, that the remaining flux outside of the SAA is comparable to that of a low inclined orbit. Therefore, a very low detector background can be achieved, when an orbit with higher inclination is selected and observations are only made outside the radiation belts.

Although the simulations for eROSITA are only a very recent project and no detailed model has yet been created, a first estimation of the general shape of the background spectrum was possible. In the end, however, the outcome of these simulations depends directly on the input spectra from the models for the orbit environment. At least for near earth orbits outside of the radiation belts, the modelling possibilities available at the moment appear a bit unsatisfactory. Still it is clear, that the simulation results favor a 51° orbit over the 29° orbit. Also any inclination $< \sim 20^\circ$ that would completely avoid the SAA is recommendable with respect to the background. A position in the L2 point would also result in a low, temporally constant background, which is highly desirable. However, the cosmic-ray protons flux at this position is much more extended to higher energies than that of the trapped particles in near earth orbits

(see Fig. 8.4) and thus the rate of high-energy proton interaction with the CCD in spite of the proton shield increases strongly. A trade-off between protection of the CCD and background generation should therefore be the ultimate goal of the camera design and orbit selection.

For the near future, it is foreseen to implement a detailed version of the actual camera geometry. This will allow also to investigate details of the detector background like the production of fluorescence lines from materials close to the CCD. Predictions of a wider variety of models for the proton background will also be analyzed.

Summary and Conclusions

In the course of this work it was demonstrated that Monte-Carlo simulations of the physics processes and interactions taking place in a space-based X-ray detector as a result of its orbital environment are capable of explaining the measured detector background of existing missions. They are, therefore, an excellent tool in predicting the background of future observatories. Details about the GEANT4 Monte-Carlo simulation toolkit, which lies at the core of the simulations, have been introduced and the quality and potential of the simulation environment created for this thesis has been proven. The environment was then used to predict the background of the future X-ray instruments Simbol-X and eROSITA.

9.1 Summary

Below is a short overview of the main results of this work:

- **XMM-Newton**

The simulation results for the internal camera background of the pn-camera served as an important criterion to judge the quality of the simulation environment. The quantum efficiency of the pn-CCDs could be reproduced nicely. The same applies to the overall spectral shape and level of the camera background. Although the intensities of the fluorescence lines in the spectrum deviate slightly from the measured ones (due to missing details in the mass model and/or inaccuracies of the toolkit), the images of the background events around these lines reproduce the origin of the registered events exactly. This is the first time that the pn-camera background has been reproduced to this extent with simulations. The measured spectra shown in Fig. 3.8 also represent the largest background compilation from 'Closed' observations up to now.

- **Simbol-X**

The simulations for Simbol-X were performed in parallel to the design and development of the actual detector. They were a valuable source of input for the engineers as it was possible to evaluate suggestions and changes in the geometry with respect to the background. Therefore, the results of the simulations had a major impact on today's design. The outcome of different studies regarding the shielding, the background and the deadtime of the detectors were described in this work. For the latest configuration, the composition, level and shape of the remaining detector background were presented. Based on these results, the sensitivity of the instrument and, ultimately, its scientific performance were estimated.

An experiment to measure the contribution of fluorescence backlight from the HED to the overall LED background was simulated and carried out. It was shown that this effect is negligible. Furthermore, an on-board event-preprocessor to further reduce the background and the telemetry rate of Simbol-X was developed and tested in collaboration with the electronics lab at IAAT.

- **eROSITA**

A simple approximation of the eROSITA camera was modelled for GEANT4 simulations. Interactions of high-energy (> 10 MeV) protons with the camera materials, mainly the proton shield, were simulated. The effects of their interactions on the camera background were evaluated for different orbit parameters and environments. On this basis, a recommendation for the best (available) orbit with respect to the background level is given.

Summarizing the experiences with the simulation toolkit, it can be said that the quality of the results from these simulations depends strongly on the accuracy of the geometric model of the instrument as well as on a realistic representation of the input particle environment.

9.2 Outlook

The current simulation environment developed within this work applies to all kinds of X- and γ -ray detectors. It allows a range of applications even beyond space-based instruments. Besides the detector background, also scientific observations can be simulated with it. This was indicated in Chapter 5 in the context of an observation of the Cosmic X-ray Background. Furthermore, arbitrary X-ray source populations can be placed within the field of view, producing counts that have to be registered and identified in the presence of the background interactions. This will presumably be the next step for the Simbol-X simulations. In this way, the model and the environment can be used even after launch to be first verified with observations and to aid in understanding the instrument behaviour.

The implementation of a more detailed camera model for eROSITA and the intensity of the fluorescence lines seen in the pn-camera background of XMM-Newton will both be subjects of in-depth studies in collaboration with the HLL in the near future. The geometric models of XMM and Simbol-X presented here are foreseen to be made available to the scientific community soon.

The HEXIS (High-Energy X-ray Imaging Spectrometer) balloon experiment led by the University of California, San Diego, and proposed to NASA this summer is currently simulated with an environment derived from the basics of the one presented in this work. Finally, simulations for the background of the INTEGRAL (INTERNATIONAL Gamma-Ray Astrophysics Laboratory) detectors with this environment will start soon in order to further prove and improve its capabilities.

Simulations of the internal background of space-based detectors like the ones presented here are becoming an important factor in the development of new instruments. They allow to avoid

otherwise unnoticed sources of background and to improve the detector geometry in order to achieve optimum science output. The number of publications on Monte-Carlo simulations in this context as well as the number of scientists in the GEANT4 space user community are increasing rapidly. These simulations are also helpful for already existing missions as they can definitely contribute to our understanding of their background composition.

APPENDIX A

Details of the Simulation Environment

During the work for this thesis, the author was part of the Science Payload Simulation Team (SPST). Its members independently performed simulation studies regarding various different topics and reported them periodically at the meetings of the background group. The geometry was shared and important results were also cross-checked between the members of the team. Table A.1 shows the current and former members of the group.

Table A.1: *The SPST background group is composed of experts in different background fields and in previous space experiments (e.g. XMM, Integral, BeppoSax).*

Name	Affiliation
Briel, Uli	MPE, Garching, Germany
Bulgarelli, Andrea	IASF, Bologna, Italy
Chipaux, Rémi	CEA/DSM/DAPNIA, Saclay, France
Foschini, Luigi	IASF, Bologna, Italy
Kendziorra, Eckhard	IAAT, Tübingen, Germany
Klose, Christian	TU Darmstadt, Germany
Kuster, Markus	TU Darmstadt, Germany
Laurent, Philippe	CEA/DSM/DAPNIA, Saclay, France
Tenzer, Christoph	IAAT, Tübingen, Germany

The simulation of physics processes by the GEANT4 kernel is included into the respective simulation environment by instantiating the different particles and assigning the appropriate processes to them. Table A.2 contains the complete list of all particles accounted for in the environment presented here.

Table A.2: *Complete list of implemented particles*

GEANT4 Class	Particles
Leptons	$e^-, e^+, \nu_e, \bar{\nu}_e, \mu^-, \mu^+, \nu_\mu, \bar{\nu}_\mu, \tau^-, \tau^+, \nu_\tau, \bar{\nu}_\tau$
Light Mesons	$\pi^+, \pi^-, \pi^0, K^+, K^-, K_s^0, K_L^0, \eta^0, \eta^{0'}$
Charm Mesons	$D^+, D^-, D^0, \bar{D}^0, D_s^+, D_s^-, J/\Psi$
Bottom Mesons	$B^+, B^-, B^0, \bar{B}^0, B_s^0, \bar{B}_s^0$
Nucleons	p, n, \bar{p}, \bar{n}
Strange Baryons	$\Lambda, \bar{\Lambda}, \Sigma^+, \Sigma^-, \Sigma^0, \bar{\Sigma}^+, \bar{\Sigma}^-, \bar{\Sigma}^0, \Xi^-, \Xi^0, \bar{\Xi}^-, \bar{\Xi}^0$
Charm Baryons	$\Lambda_c^+, \Omega_c^0, \Sigma_c^+, \Sigma_c^{++}, \Sigma_c^0, \Xi_c^+, \Xi_c^0, \Lambda_c^+, \Omega_c^0, \bar{\Sigma}_c^+, \bar{\Sigma}_c^{++}, \bar{\Sigma}_c^0, \bar{\Xi}_c^+, \bar{\Xi}_c^0$
Ions	Alpha, Deuteron, ^3He , Triton, other generic ions
Shortlived	Baryon Resonances, Meson Resonances, Quarks
Others	Gammas, optical Photons

The following table gives the electromagnetic interactions considered in the simulations presented in this work for each particle type.

Table A.3: *List of electromagnetic physics processes included in the simulation environment*

Electromagnetic and Low-Energy (LE) Electromagnetic Processes	
Particle	Process Name
Gamma	LE Compton Scattering, LE Photoelectric Effect, LE Gamma Conversion, LE Rayleigh Scattering
e^-	Multiple Scattering, LE Ionization, LE Bremsstrahlung
e^+	Multiple Scattering, Ionization, Bremsstrahlung, e^+ Annihilation
μ^-	Multiple Scattering, Ionization, Bremsstrahlung, Pair Production, μ^- Capture at Rest
μ^+	Multiple Scattering, Ionization, Bremsstrahlung, Pair Production
τ^+ , τ^-	Multiple Scattering, Ionization
generic ions	Multiple Scattering, LE Ionization
Shortlived	Multiple Scattering, LE Ionization

The description of hadronic interactions in GEANT4 is much more complex than that of electromagnetic interactions. In order to meet the multidisciplinary requirements on this topic, the hadronic framework in GEANT4 provides a large degree of functionality and flexibility. Sets of alternative physics models are available, so that the user can freely choose appropriate models according to the type of application. Each cross section table or physics model has its own energy range, so the user is able to combine different models (*see Fig. A.1 for an overview of models available at certain energy ranges*).

The modular structure of GEANT4 hadronic interactions is separated into five levels of implementation framework (*see Fig. A.2*). These have to be specified together with the models implementing them in order to assemble the hadronic physics for the simulation engine. However, there are default cross section sets provided for each type of hadronic process (At Rest, Elastic, Inelastic, Capture, Fission). Some contain only a few numbers to parametrize cross sections while others represent large databases (in data driven models).

The number of options that are available to assemble a hadronic physics list is therefore quite large and there are many particle species to be tracked that need complete and consistent physics. Therefore, the choice of model depends on the physics studied. The conclusion that should be drawn of this is that no single model covers all energies or all particles and much care is required when assembling the physics list. However, many pre-assembled hadronic physics lists are available for topics like low and high energy nucleon penetration shielding, low energy dosimetric applications, medical neutron applications, low background experiments (underground) and, of course, space applications.

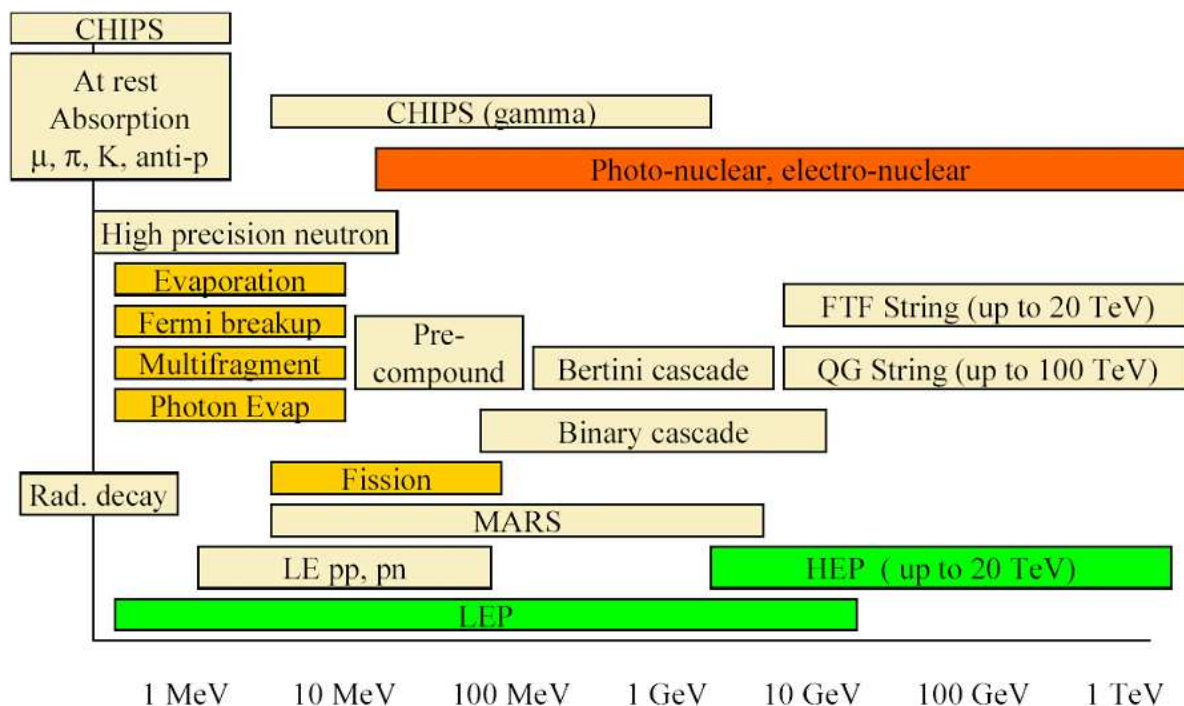


Figure A.1: Overview of the valid energy ranges for different hadronic model implementations in GEANT4 (Wright/Helkinnen, CERN).

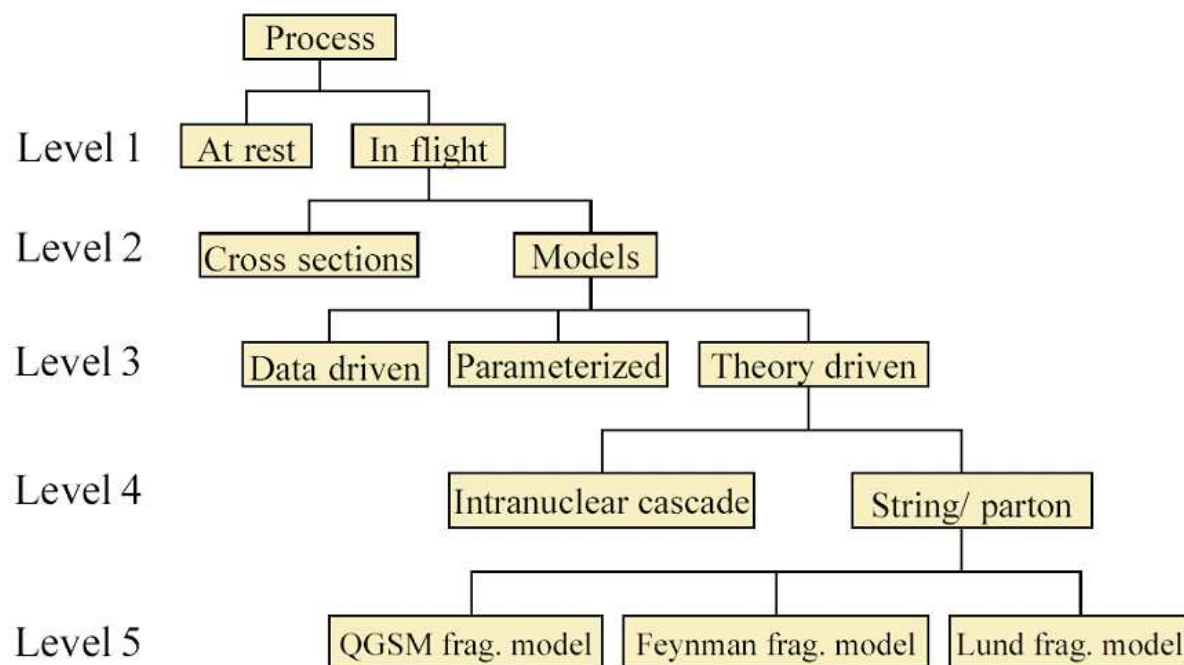


Figure A.2: Hierarchy of the different interaction levels in the hadronic model framework in GEANT4 (Wright/Helkinnen, CERN).

Bibliography

- Ables, J. G., Fourier transform photography: a new method for X-ray astronomy. *Proceedings of the Astronomical Society of Australia*, 1:172–+, December 1968.
- Agostinelli, S. et al., Geant4 - a simulation toolkit. *Nuclear Instruments and Methods in Physics Research A*, 506:250–303, July 2003.
- Allen, S. W., Rapetti, D. A., Schmidt, R. W., Ebeling, H., Morris, R. G., and Fabian, A. C., Improved constraints on dark energy from Chandra X-ray observations of the largest relaxed galaxy clusters. *MNRAS*, 383:879–896, January 2008.
- Allison, J. et al., Geant4 developments and applications. *IEEE Transactions on Nuclear Science*, 53: 270–278, 2006.
- Amako, K. et al., Geant4 and its validation. *Nucl. Phys. Proc. Suppl.*, 150:44–49, 2006.
- Apostolakis, J. et al., Geant4 low energy electromagnetic models for electrons and photons. *CERN-OPEN-99-034*, 1999.
- Arefiev, V., Pavlinsky, M., Revnivtsev, M., Churazov, E., Gilfanov, M., Kumakhov, M., Lapshov, I., Levin, V., Akimov, V., Semena, N., Tkachenko, A., Vikhlinin, A., and Sunyaev, R., Hard x-ray concentrator experiment for Spectrum-X-Gamma mission. In *Proceedings of the SPIE*, volume 6266, July 2006.
- Asai, M., Geant4 Applications in Space. In *Invited talk at 10th ICATPP Conference on Astroparticle, Particle, Space Physics, Detectors and Medical Physics Applications, Como, Italy, 8-12 Oct, 2007*.
- Aschenbach, B., X-ray telescopes. *Reports of Progress in Physics*, 48:579–629, May 1985.
- Bradt, H. V., Rothschild, R. E., and Swank, J. H., X-ray timing explorer mission. *A&AS*, 97:355–360, January 1993.
- Brandt, W. N. and Hasinger, G., Deep Extragalactic X-Ray Surveys. *ARA&A*, 43:827–859, September 2005.
- Briel, U. G. et al., Calibration and preliminary results on the performance of the XMM EPIC PN flight camera: imaging modes. In Siegmund, O. H. and Gummin, M. A., editors, *Proceedings of the SPIE, EUV, X-Ray, and Gamma-Ray*, volume 3445, pages 38–49, November 1998.
- Campana, S., Transient neutron star X-ray binaries with Simbol-X. In *Proc. of the workshop 'Simbol-X: The hard X-ray universe in focus', Bologna 14-16 May, 2007*.

- Chipaux, R., Briel, U., Bulgarelli, A., Foschini, L., Kendziorra, E., Klose, C., Kuster, M., Laurent, P., and Tenzer, C., Status of the Simbol-X detector background simulation activities. *Memorie della Societa Astronomica Italiana*, 79:234–+, 2008.
- Claret, A., Space environment of Simbol-X. CEA/Dapnia/SAP internal report, 2006.
- Comastri, A. et al., The Simbol-X view of the unresolved X-ray background. In *Proc. of the workshop 'Simbol-X: The hard X-ray universe in focus'*, Bologna 14-16 May, 2007.
- Cooperman, G., Nguyen, V. H., and Malioutov, I., Parallelization of geant4 using top-c and marshal-gen. In *NCA '06: Proceedings of the Fifth IEEE International Symposium on Network Computing and Applications*, pages 48–55, Washington, DC, USA, 2006. IEEE Computer Society. ISBN 0-7695-2640-3.
- Della Ceca, R. et al., Heavily obscured AGN with BeppoSAX, INTEGRAL, SWIFT, XMM and Chandra: prospects for Simbol-X. In *Proc. of the workshop 'Simbol-X: The hard X-ray universe in focus'*, Bologna 14-16 May, 2007.
- Dicke, R. H., Scatter-Hole Cameras for X-Rays and Gamma Rays. *ApJ*, 153:L101+, August 1968.
- Dirks, B.P.F. et al., The focal plane of the SIMBOL-X space mission. In *Proceedings of the SPIE*, volume 6276-45, 2006.
- Ferguson, C., General purpose Source Particle Module for Geant4/SPARSET: User Requirements Document. *UoS-GSPM-URD*, Issue 1.1, 2000.
- Ferrando, P., Simbol-X: a formation flying mission for hard X-ray astrophysics. *Science proposal submitted to CNES*, 2005.
- Ferrando, P. et al., SIMBOL-X: a formation flying mission for hard X-ray astrophysics. In *Proceedings of the SPIE*, pages 195–204, August 2005.
- Ferrando, P. et al., The SIMBOL-X mission. In *Proceedings of the SPIE*, June 2008.
- Ferrando, P. and Giommi, P., Simbol-X Scientific Performance. Internal Paper, 2007.
- Ferrando, P., Lortholary, M., Pigot, C., and Sauvageot, J. L., Cosmic ray identification and rejection in the EPIC-MOS cameras onboard XMM-Newton: results from flight data. In Truemper, J. E. and Tananbaum, H. D., editors, *Proceedings of the SPIE*, volume 4851, pages 270–276, March 2003.
- Fiore, F. et al., Science with Simbol-X. In *Proc. of the workshop 'Simbol-X: The hard X-ray universe in focus'*, Bologna 14-16 May, 2007.
- Fraser, G. W., *X-ray detectors in astronomy*. Cambridge and New York, Cambridge University Press, 1989, 312 p., 1989.
- Fraser, G. W. et al., LOBSTER-ISS: an imaging x-ray all-sky monitor for the International Space Station. In Flanagan, K. A. and Siegmund, O. H., editors, *Proceedings of the SPIE*, volume 4497, pages 115–126, January 2002.

- Freyberg, M. J., Briel, U. G., Dennerl, K., Haberl, F., Hartner, G. D., Pfeffermann, E., Kendziorra, E., Kirsch, M. G. F., and Lumb, D. H., EPIC pn-CCD detector aboard XMM-Newton: status of the background calibration. In *Proceedings of the SPIE, Volume 5165*, pp. 112-122, pages 112–122, February 2004.
- Friedman, H., Lichtman, S. W., and Byram, E. T., Photon Counter Measurements of Solar X-Rays and Extreme Ultraviolet Light. *Physical Review*, 83:1025–1030, September 1951.
- Friedrich, P., *The Universe in X-rays*. Springer-Verlag, J. Truemper + G. Hasinger (Editors), 2008.
- Geant4 Collaboration, Geant4 User's Guide for Application Developers. Version 8.2, 2006.
- Giacconi, R., The Einstein X-ray Observatory. *Scientific American*, 242:80–85, February 1980.
- Giacconi, R., Gorenstein, P., Murray, S. S., Schreier, E., Seward, F., Tananbaum, H., Tucker, W. H., and van Speybroeck, L., *The Einstein Observatory and future X-ray telescopes*, pages 195–278. Telescopes for the 1980s, Annual Reviews Monograph, 1981.
- Giacconi, R., Gursky, H., Paolini, F. R., and Rossi, B. B., Evidence for X-Rays From Sources Outside the Solar System. *Physical Review Letters*, 9:439–443, December 1962.
- Giacconi, R., Gursky, H., and van Speybroeck, L. P., Observational Techniques in X-Ray Astronomy. *ARA&A*, 6:373–+, 1968.
- Giacconi, R., Gursky, H., and Waters, J. R., Two Sources of Cosmic X-rays in Scorpius and Sagittarius. *Nature*, 204:981–982, December 1964.
- Gilli, R., Comastri, A., and Hasinger, G., The synthesis of the cosmic X-ray background in the Chandra and XMM-Newton era. *A&A*, 463:79–96, February 2007.
- Gruber, D. E., Matteson, J. L., Peterson, L. E., and Jung, G. V., The Spectrum of Diffuse Cosmic Hard X-Rays Measured with HEAO 1. *The Astrophysical Journal*, 520:124–129, July 1999.
- Guatelli, S. and Mantero, A. and Mascialino, B. and Nieminen, P. and Pia, M. G., Geant4 Atomic Relaxation. *IEEE Transactions on Nuclear Science*, 54:585–593, June 2007.
- Harris, D. E., Forman, W., Gioia, I. M., Hale, J. A., Harnden, F. R., Jr., Jones, C., Karakashian, T., Maccacaro, T., McSweeney, J. D., and Primini, F. A., editors. *The Einstein Observatory catalog of IPC X ray sources.*, volume 1, April 1993.
- Hartmann, R. et al., Quantum efficiency of the XMM pn-CCD camera. In *Proceedings of the SPIE*, volume 3765, pages 703–713, October 1999.
- Heller, J., *Catch-22*. Simon and Schuster, 1961.
- Jagoda, N., Austin, G., Mickiewicz, S., and Goddard, R., The UHURU X-Ray Instrument. *IEEE Transactions on Nuclear Science*, 19:579–+, February 1972.
- James, F., A Review of Pseudorandom Number Generators. *Comp. Phys. Comm.* 60, pages 329–344, 1990.
- Jansen, F. et al., XMM-Newton observatory. I. The spacecraft and operations. *A&A*, 365:L1–L6, January 2001.

- Kelley, R. L., The Astro-E2 Mission. In *Bulletin of the American Astronomical Society*, volume 36 of *Bulletin of the American Astronomical Society*, pages 925–+, August 2004.
- Klose, C., Simulationen zum Detektorhintergrund des Röntgensatelliten SIMBOL-X. Diploma Thesis, University of Darmstadt, 2007.
- Kok, M. V., Kaya, E., and Akin, S., Monte Carlo Simulation of Oil Fields. *Energy Sources, Part B: Economics, Planning and Policy*, 1:207–211, July 2006.
- Kortright, J. B., *X-ray Data Booklet*, pages 53–54. Lawrence. Berkeley Labs, Berkeley, 2001.
- Krause, M. O., Atomic radiative and radiationless yields for K and L shells. *Journal of Physical and Chemical Reference Data*, Volume 8 Issue 2:307–327, April 1997.
- Kunieda, H., Mitsuda, K., and Takahashi, T., New Japanese X-ray Mission: NeXT. In *Bulletin of the American Astronomical Society*, 2006.
- Laurent, P., Lechner, P., Authier, M., Briel, U., Cara, C., Colonges, S., Ferrando, P., Fontignie, J., Kendziorra, E., Limousin, O., Martignac, J., Meuris, A., Ravera, L., and Rio., Y., The Simbol-X focal plane. *Memorie della Societa Astronomica Italiana*, 79:32–+, 2008.
- Lechner, P. et al., The low energy detector of Simbol-X. In *Proceedings of the SPIE*, June 2008.
- Lehmann, I., Hasinger, G., Schmidt, M., Giacconi, R., Trümper, J., Zamorani, G., Gunn, J. E., Pozzetti, L., Schneider, D. P., Stanke, T., Szokoly, G., Thompson, D., and Wilson, G., The ROSAT Deep Survey. VI. X-ray sources and Optical identifications of the Ultra Deep Survey. *A&A*, 371: 833–857, June 2001.
- Malaguti, G. et al., Active and passive shielding design optimization and technical solutions for deep sensitivity hard x-ray focusing telescopes. In Citterio, O. and O’Dell, S. L., editors, *Proceedings of the SPIE*, volume 5900, pages 159–171, August 2005.
- Meidinger, N., Andritschke, R., Hälker, O., Hartmann, R., Hartner, G., Hasinger, G., Herrmann, S., Holl, P., Hyde, E., Kimmel, N., Pfeffermann, E., Predehl, P., Soltau, H., and Strüder, L., Systematic testing and results of x-ray CCDs developed for eROSITA and other applications. In *Proceedings of the SPIE*, volume 6276, July 2006a.
- Meidinger, N., Andritschke, R., Hälker, O., Hartmann, R., Herrmann, S., Holl, P., Lutz, G., Kimmel, N., Schaller, G., Schnecke, M., Schopper, F., Soltau, H., and Strüder, L., Next generation of pnCCDs for X-ray spectroscopy and imaging. *Nuclear Instruments and Methods in Physics Research A*, 568:141–148, November 2006b.
- Mertz, L., a Dilute Image Transform with Application to AN X-Ray Star Camera. In Fox, J., editor, *Modern Optics*, pages 787–+, 1967.
- Metropolis, N., Monte-Carlo: In the Beginning and Some Great Expectations. In Alcouffe, R., Dautray, R., Forster, A., Ledonois, G., and Mercier, B., editors, *Monte-Carlo Methods and Applications in Neutronics, Photonics, and Statistical Physics*, volume 240 of *Lecture Notes in Physics*, Berlin Springer Verlag, pages 62–+, 1985.
- Metropolis, N., The Beginning of the Monte Carlo Method. *Los Alamos Science Special Issue*, 15: 125–130, January 1987.

- Meuris, A., Limousin, O., Lugiez, F., Gevin, O., Pinsard, F., Le Mer, I., Delagnes, E., Vassal, M. C., Soufflet, F., and Bocage, R., Caliste 64, an Innovative CdTe Hard X-Ray Micro-Camera. *IEEE Transactions on Nuclear Science*, 55:778–784, April 2008.
- Mitsuda, K., Kelley, R., McCammon, D., den Herder, J.-W., and Ohashi, T., Microcalorimeter Instruments for the Spectrum-R(X)G and NeXT Missions. *Journal of Low Temperature Physics*, 151: 703–708, May 2008.
- Mitsuda, K., Kunieda, H., Inoue, H., and Kelley, R., Astro-E2 mission. In Hasinger, G. and Turner, M. J. L., editors, *Proceedings of the SPIE*, volume 5488 of *Presented at the Society of Photo-Optical Instrumentation Engineers (SPIE) Conference*, pages 177–186, October 2004.
- Nartallo, R., Daly, E., Evans, H., Nieminen, P., Lei, F., and Truscott, P., Low-angle scattering of protons on the XMM-Newton optics and effects on the on-board CCD detectors. *IEEE Transactions on Nuclear Science*, 48:1815–1821, December 2001.
- Nichol, R. C., Cosmology with galaxy correlations. *General Relativity and Gravitation*, 40:249–267, February 2008.
- O’Dell, S. L. et al., ART: Surveying the Local Universe at 2–11 keV. In *AAS/High Energy Astrophysics Division*, volume 10 of *AAS/High Energy Astrophysics Division*, pages 36++, March 2008.
- Ogallagher, J. J. and Maslyar, G. A., III, A dynamic model for the time evolution of the modulated cosmic ray spectrum. *Journal of Geophysical Research*, 81:1319–1326, March 1976.
- Pareschi, G., Basso, S., Citterio, O., Ghigo, M., Mazzoleni, F., Spiga, D., Burkert, W., Freyberg, M., Hartner, G. D., Conti, G., Mattaini, E., Grisoni, G., Valsecchi, G., Negri, B., Parodi, G., Marzorati, A., and dell’Acqua, P., Development of grazing-incidence multilayer mirrors by direct Ni electroforming replication: a status report. In Citterio, O. and O’Dell, S. L., editors, *Proceedings of the SPIE*, volume 5900, pages 47–58, August 2005.
- Pareschi, G., Cotroneo, V., Spiga, D., Vernani, D., Barbera, M., Artale, M. A., Collura, A., Varisco, S., Grisoni, G., Valsecchi, G., and Negri, B., Astronomical soft x-ray mirrors reflectivity enhancement by multilayer coatings with carbon overcoating. In Hasinger, G. and Turner, M. J. L., editors, *Proceedings of the SPIE*, volume 5488, pages 481–491, October 2004.
- Pavlinisky, M., Hasinger, G., Parmar, A., Fraser, G., Churazov, E., Gilfanov, M., Sunyaev, R., Vikhlinin, A., Predehl, P., Piro, L., Arefiev, V., Tkachenko, A., Pinchuk, V., and Gorobets, D., Spectrum-RG/eROSITA/Lobster astrophysical mission. In *Proceedings of the SPIE*, volume 6266, July 2006.
- Perkins, S.T., Cullen, D.E., Chen, M.H., Hubbell, J.H., Rathkopf, J., and Scofield, J., Tables and Graphs of Atomic Subshell and Relaxation Data Derived from the LLNL Evaluated Atomic Data Library (EADL), Z=1-100. 30, 1991.
- Pfeffermann, E. et al., PN-CCD camera for XMM and ABRIXAS: design of the camera system. In Siegmund, O. H. and Flanagan, K. A., editors, *Proceedings of the SPIE, EUV, X-Ray, and Gamma-Ray Instrumentation for Astronomy*, volume 3765, pages 184–191, October 1999.
- Pfeffermann, E. et al., Shielding of cosmic-ray-induced background in CCD detectors for X-ray astronomy. In Holland, A. D., editor, *Proceedings of the SPIE*, volume 5501, pages 304–311, September 2004a.

- Pfeffermann, E., Meidinger, N., Strüder, L., Bräuninger, H., and Hartner, G., Lessons learned from the EPIC pn-CCD camera for future missions. *Memorie della Societa Astronomica Italiana*, 75: 555–+, 2004b.
- Predehl, P. et al., eROSITA. In *Proceedings of the SPIE*, volume 6266, July 2006.
- Ritz, S. M., Michelson, P. F., Meegan, C., Grindlay, J., and GLAST Mission Team, The Gamma-ray Large Area Space Telescope (GLAST) Mission. In *American Astronomical Society Meeting Abstracts*, 2007.
- Santin, G. et al., New Geant4 based simulation tools for space radiation shielding and effects analysis. *Nuclear Physics B Proceedings Supplements*, 125:69–74, September 2003.
- Schanz, T., Tenzer, C., Kendziorra, E., and Santangelo, A., A fast event preprocessor for the SIMBOL-X low-energy detector. In *Proceedings of the SPIE*, June 2008.
- Skinner, G. K., Coding (and Decoding) Coded Mask Telescopes. *Experimental Astronomy*, 6:1–7, December 1995.
- Strüder, L. et al., The European Photon Imaging Camera on XMM-Newton: The pn-CCD camera. *A&A*, 365:L18–L26, January 2001.
- Strüder, L., Meidinger, N., Pfeffermann, E., et al., X-ray pn-CCDs on the XMM Newton Observatory. In Truemper, J. E. and Aschenbach, B., editors, *Proceedings of the SPIE*, volume 4012, pages 342–352, July 2000.
- Taylor, B. G., Andresen, R. D., Peacock, A., and Zobl, R., The EXOSAT mission. *Space Science Reviews*, 30:479–494, March 1981.
- Tenzer, C., Kendziorra, E., Santangelo, A., Kuster, M., Ferrando, P., Laurent, P., Claret, A., and Chipaux, R., Monte Carlo simulations of stacked x-ray detectors as designed for SIMBOL-X. In *Proceedings of the SPIE, Volume 6266, pp. 62662O (2006)*, July 2006.
- Treis, J. et al., Noise and spectroscopic performance of DEPMOSFET matrix devices of XEUS. In *Proceedings of the SPIE*, volume 5898, pages 256–266, 2005.
- Treis, J. et al., Study of noise and spectroscopic performance of DEPMOSFET matrix prototypes for XEUS. volume 568, pages 191–200, November 2006.
- Truemper, J., The ROSAT mission. *Advances in Space Research*, 2:241–249, 1982.
- Turner, M. J. L. et al., The European Photon Imaging Camera on XMM-Newton: The MOS cameras. *A&A*, 365:L27–L35, January 2001.
- Voges, W., Aschenbach, B., Boller, T., Braeuninger, H., Briel, U., Burkert, W., Dennerl, K., Enghauser, J., Gruber, R., Haberl, F., Hartner, G., Hasinger, G., Kuerster, M., Pfeffermann, E., Pietsch, W., Predehl, P., Rosso, C., Schmitt, J. H. M. M., Truemper, J., and Zimmermann, H. U., ROSAT All-Sky Bright Source Catalogue (1RXS) (Voges+ 1999). *VizieR Online Data Catalog*, 9010:0–+, November 1999.

- Voges, W., Aschenbach, B., Boller, T., Brauning, H., Briel, U., Burkert, W., Dennerl, K., Enghauser, J., Gruber, R., Haberl, F., Hartner, G., Hasinger, G., Pfeffermann, E., Pietsch, W., Predehl, P., Schmitt, J., Trumper, J., and Zimmermann, U., ROSAT All-Sky Survey Faint Source Catalog (Voges+ 2000). *VizieR Online Data Catalog*, 9029:0–+, May 2000.
- Weisskopf, M. C., Brinkman, B., Canizares, C., Garmire, G., Murray, S., and Van Speybroeck, L. P., An Overview of the Performance and Scientific Results from the Chandra X-Ray Observatory. *PASP*, 114:1–24, January 2002.
- Winkler, C., Courvoisier, T. J.-L., Di Cocco, G., Gehrels, N., Giménez, A., Grebenev, S., Hermsen, W., Mas-Hesse, J. M., Lebrun, F., Lund, N., Palumbo, G. G. C., Paul, J., Roques, J.-P., Schnopper, H., Schönfelder, V., Sunyaev, R., Teegarden, B., Ubertini, P., Vedrenne, G., and Dean, A. J., The INTEGRAL mission. *A&A*, 411:L1–L6, November 2003.
- Wolter, H., Spiegelsysteme streifenden Einfalls als abbildende Optiken für Röntgenstrahlen. *Annalen der Physik*, 445:94–114, 1952.
- Worsley, M. A., Fabian, A. C., Alexander, D. M., Bauer, F. E., Brandt, W. N., Hasinger, G., and Lehmer, B. D., Resolving the X-ray Background. In Bulik, T., Rudak, B., and Madejski, G., editors, *Astrophysical Sources of High Energy Particles and Radiation*, volume 801 of *American Institute of Physics Conference Series*, pages 51–56, November 2005.
- Zhang, C., Lechner, P., Lutz, G., Porro, M., Richter, R., Treis, J., Strüder, L., and Nan Zhang, S., Development of DEPFET Macropixel detectors. *Nuclear Instruments and Methods in Physics Research A*, 568:207–216, November 2006.

List of Figures

1.1	Attenuation of Electromagnetic Radiation in the Earth's Atmosphere, after Giacconi et al. (1968)	2
1.2	Imaging Techniques: Honeycomb Collimator, Rotation Modulation Collimator, Coded Mask	4
1.3	Imaging Techniques: Wolter Type-I Telescope	6
1.4	Detection Techniques: pn-CCD and Crossed-Strip Detector (T. Schanz)	7
1.5	Sensitivity of Current and Historic X- and Gamma-ray Observatories	9
2.1	The Fermiac - a Monte-Carlo Simulation Device (Metropolis, 1985)	16
2.2	Structural Scheme of an Exemplary Simulation with GEANT4	21
2.3	Class Diagram of the Low Energy Electromagnetic Processes	23
3.1	The XMM-Newton satellite (ESA/Dornier)	27
3.2	The Focal Planes of XMM-Newton's MOS- and pn-Camera (Leicester University/MPE)	29
3.3	The EPIC pn-Camera Head - Geometric Model	30
3.4	Layout of the CCDs in the Focal Plane of the pn-Camera	31
3.5	Geometrical Model of the pn-Camera's Focal Plane Printed Circuit Board	32
3.6	Time-Coverage of EPIC-pn FF and eFF Observations With 'Closed' Filter	33
3.7	Measured EPIC-pn Background Spectrum in FF and eFF Operation Modes	33
3.8	Measured EPIC-pn Background During Different Times of the Solar Cycle	34
3.9	Solar Flux Progression During the Current Solar Cycle (NOAA/SWPC, Boulder, Colorado)	36
3.10	Cosmic-Ray Proton Spectra Used in the XMM-Newton Simulations	36
3.11	Simulated vs. Measured Quantum Efficiency of the pn-Camera	38
3.12	Comparison Between Simulated and Measured EPIC-pn Background Spectra	39
3.13	Comparison Between Simulated and Measured Fluorescence Images	41
4.1	The Simbol-X Mission (CNES/Oliver Sattler, 2006)	43
4.2	The Simbol-X Orbit	44
4.3	The Composition of the Cosmic X-ray Background (Gilli et al., 2007)	46
4.4	Effective Area of the Simbol-X Mirror Module (G. Pareschi, INAF)	48
4.5	Model of a DEPFET Pixel (MPI Semiconductor Laboratory)	49
4.6	The Simbol-X Low Energy Detector (MPI Semiconductor Lab)	50
4.7	The Simbol-X High Energy Detector (CEA/DAPNIA)	51
5.1	Simplified Illustration of the Geometry of the Two Simbol-X Spacecraft	55
5.2	Evolution of the Simbol-X Geometric Model Used in the Simulations	57
5.3	Current Model of the Simbol-X Focal Plane Used in the Simulations	58
5.4	Photon Spectrum of the Cosmic X-ray Background as Given by Gruber et al. (1999) and Cosmic Ray Proton Spectrum as Given in Claret (2006)	61
5.5	Cut Length vs. Computation Time in Simulations	64
5.6	Quantum Efficiency of the Simbol-X Low Energy Detector	65

5.7	Quantum Efficiency of the Simbol-X High Energy Detector	65
5.8	Composition of the Simbol-X Detector Background (Geometry Version 3)	66
5.9	Simbol-X Simulated Background Spectrum	67
5.10	Efficiency of the Simbol-X Graded Shield	68
5.11	Effects of Thickness Variation of the Tantalum Component in the Graded Shield	69
5.12	Calculated Deadtime of the Low Energy Detector	70
5.13	Calculated Signal/Noise Ratio in the LED for a Weak Source	70
5.14	Proton Induced Secondary Particle Spectrum at the Location of the Lateral AC Slabs	71
5.15	AC Effectivity and Count rates as a Function of AC Trigger Threshold	72
5.16	Updated Drawings of the Simbol-X Focal Plane (CEA, Saclay)	73
5.17	Snapshot From an Ongoing Simulation with CXB Photons	74
5.18	Calculated Deadtime of the Low Energy Detector (Geometry Version 4)	74
5.19	Simulated Spectra of an Observation of the Cosmic X-ray Background	75
5.20	Simbol-X: Minimum Detectable Flux	76
5.21	Estimation of the Simbol-X Sensitivity	77
5.22	Comparison of the Current Simbol-X Background Composition to that of Previous Geometry Versions	78
6.1	Lab Setup for the Measurement of the CdTe Fluorescence Lines (M. Martin)	80
6.2	The Aluminum Slider Carrying the CdTe Crystals (M. Martin)	81
6.3	Central Area of the DEPFET Matrix (M. Martin) and Functional Block Diagram of the Lab System Setup	82
6.4	Fluorescence yields for K and L shells for $5 \leq Z \leq 110$ (Krause, M. O., 1997)	84
6.5	Simulation Model of the X-ray Fluorescence Experimental Setup	84
6.6	Simulated Spectra for the Fluorescence Experiment	86
6.7	Pattern Flux of Fluorescence Measurements No. 3, 7 and 8	88
6.8	Comparison Between Simulated and Measured Fluorescence Spectra	89
7.1	Functional Block Diagram of the Simbol-X Low Energy Detector Assembly (E. Kendziorra)	92
7.2	Block Diagram of the Simbol-X EPP (T. Schanz)	95
7.3	Valid Pixel Patterns Recognized by the Simbol-X EPP	97
7.4	Block Diagram of the Simbol-X EPP Testbench (T. Schanz)	99
7.5	Lab Setup of the Simbol-X EPP Testbench	99
7.6	Screenshot of the EPP Testbench Output	100
8.1	The eROSITA Instrument on Board of the Spectrum-RG Mission (Author/MPE)	103
8.2	Schematic Drawing of the eROSITA Detector (N. Meidinger, MPE/HLL)	107
8.3	Cut-away Drawing of an eROSITA Camera Head (L. Tiedemann, MPE)	107
8.4	Proton Spectra Used in the eROSITA Simulations	109
8.5	Simulation Geometry for the eROSITA Cameras	109
8.6	The Van Allen Radiation Belts and the South Atlantic Anomaly	110
8.7	World Map of the Trapped Proton Flux Above 10 MeV	110
8.8	Simulated eROSITA Background Spectra for Different Orbits	111
8.9	Probability of an eROSITA Detector Event as a Function of Proton Energy	112
A.1	Overview of the GEANT4 Hadronic Model Energy Ranges (Wright/Helkinnen, CERN)	121
A.2	Models at Different Levels in the GEANT4 Hadronic Framework (Wright/Helkinnen, CERN)	121

List of Tables

1.1	Overview of Instrument Parameters of Historic and Modern X-ray Observatories .	11
4.1	Simbol-X Top-Level Scientific Requirements	47
4.2	Properties of the Simbol-X Mirror Module	48
4.3	Parameters of the Simbol-X Low Energy Detector	50
4.4	Parameters of the Simbol-X High Energy Detector	51
5.1	Overview of Currently Implemented Simulation Software Versions	63
5.2	Composition of the Simbol-X Detector Background (Geometry Version 3)	66
6.1	Energies of Selected X-ray Emission Lines (Bearden, 1967)	82
6.2	Overview of the X-ray Fluorescence Simulations	85
6.3	Overview of the X-ray Fluorescence Measurements	86
8.1	Overview of the eROSITA Instrument Parameters	106
A.1	Current and Former Members of the SPST Background Group	119
A.2	Complete List of Implemented Particles	119
A.3	List of Electromagnetic Physics Processes Included in the Simulation Environment	120

Acknowledgements

I would like to thank all my friends at the institute who supported my work and enjoyed inventing or playing innumerable board-, card-, soccer- and other games with me during these last years. Furthermore, I want to thank those colleagues who participated with me in yet other activities like climbing, running, skiing, sailing and making music.

Several people have played an important role for this thesis and deserve mentioning:

- **Prof. Dr. Andrea Santangelo**
for friendly advising and supervising during the writing of this thesis
- **Dr. Eckhard Kendziorra**
for the excellent mentoring as well as many helpful ideas and suggestions. Particularly, for his continuous support throughout so far my whole academic life. A person who has always been a source of motivation.
- **The members of the simulation group**
who contributed a lot to the quality and extent of the simulation environment
- **Thomas Schanz**
for all the discussions, generous help and our joint projects
- **My parents and my girlfriend**
for their continuous support of my studies.
- **Further Acknowledgements:**
This work was partly supported by the Bundesministerium für Wirtschaft und Technologie through Deutsches Zentrum für Luft- und Raumfahrt e.V. (DLR) grants FKZ 50QR0601 and FKZ 50OG0601.

The author wishes to thank the institute 'for the friendly lease of a fully automatic calculating machine without which the realization of this work would not have been possible'.

Lebenslauf

10.09.1978: geboren in Tübingen
1985-1989: Grundschule Ofterdingen
1989-1998: Quenstedt-Gymnasium, Mössingen
1998: Abitur
07.1998-04.1999: Wehrdienst, II. Korps, Ulm
10.1999-12.2004: Eberhard-Karls-Universität Tübingen, Studium der Physik
10.2000-02.2001: wissenschaftliche Hilfskraft, Wilhelm-Schickard-Institut für Informatik, Universität Tübingen
10.2000-12.2004: wissenschaftliche Hilfskraft, Institut für Astronomie und Astrophysik, Universität Tübingen (IAAT)
11.2003-11.2004: Diplomarbeit unter Anleitung von Herrn Prof. Dr. R. Staubert: 'Entwicklung einer Sternkamera und Entwurf einer digitalen Steuerelektronik für ballongetragene Röntgenexperimente'
12.2004: Diplom
01.2005-07.2008 : wissenschaftlicher Angestellter, IAAT
01.2005-07.2008 : Anfertigung der Dissertation mit dem Titel 'Monte-Carlo Background Studies for Space-Based Detectors in X-ray Astronomy' an der Universität Tübingen, IAAT, Abt. Astronomie, unter Anleitung von Herrn Prof. Dr. A. Santangelo

Meine wichtigsten akademischen Lehrer waren die folgenden Professoren und Dozenten:

Astronomie und Astrophysik: E. Kendziorra, W. Kley, H. Ruder, A. Santangelo, R. Staubert, K. Werner, J. Wilms

Experimentalphysik: H. Clement, P. Grabmayr, G. Wagner, C. Zimmermann

Informatik: H. Klaeren, M. Sperber

Mathematik: H. Fischer, H. Kaul, M. Wolff

Medizinische Physik: F. Nüsslin

Theoretische Physik: M. Liu, H. Mütter, N. Schopohl